FIELD MEASUREMENTS OF BULK FLOW AND TRANSPORT THROUGH A SMALL COASTAL EMBAYMENT HAVING VARIABLE DISTRIBUTIONS OF AQUATIC VEGETATION

A Thesis

Presented to the Faculty of the Graduate School

of Cornell University

in Partial Fulfillment of the Requirements for the Degree of

Master of Science

by

Alexandra King

August 2006

ABSTRACT

This thesis is largely the documentation of two passive tracer release studies performed in Sterling Pond (SP), a small embayment on the southern coast of Lake Ontario (LO). SP has a large watershed and is strongly connected to LO by a long and narrow channel. The experiments were designed to decipher the effects of aquatic vegetation (macrophytes) on flow and transport through SP and through shallow embayments dominated by macrophytes in general. Towards this objective, the studies captured the residence time distribution (RTD) of water entering SP from its watershed under two different spatial distributions of macrophytes, and they were conducted in synchrony with extensive surveys of macrophyte density, height, and species composition. Variables relevant to the dynamics of SP were continuously monitored at its boundaries, including meteorological conditions, water surface elevation, flow, and temperature (temperature was continuously monitored within SP as well); bathymetric data was collected once. The first study took place when watershed flow was high and macrophytes were sparse – mean residence time was measured to be $0.6 days$. The second took place under moderate barotropic forcing from LO when watershed flow was low and macrophytes were dense and uniform across SP – mean residence time was measured to be $20 days$. As the studies were conducted under fairly extreme environmental conditions, the measured RTD's roughly capture the range of residence time scales of water entering SP from its watershed. The tracer experiments, macrophyte surveys, and auxiliary data comprise a benchmark data set that may be used for development and validation of numerical models of flow through flexible vegetation.

BIOGRAPHICAL SKETCH

Allie King has trouble explaining where she comes from, having been born in Seattle, WA, and having lived in Princeton, NJ from ages 3-9, and in Boca Raton, FL from ages 9-18. Perhaps she's from Delray Beach, FL, where she attended Atlantic Community High School with a bunch of other nerds in the International Baccalaureate program there. It was in Chris Perry's high school physics class that Allie (and countless other students) first fell in love with physics[1]. She entered Rice University in 1998, and dabbled in physics, art, biology, and electrical engineering for her first two years there. She eventually joined the civil engineering department with thoughts of architecture graduate school, but perhaps inspired by a series of epic floods and water balloon fights (both common to the Rice campus), she ended up concentrating in hydrology. Allie graduated in 2002 with a B.S. in Civil Engineering from Rice. During the summer of 2001, she worked at Cornell as an intern for Dr. Cowen just as the NSF Lake Ontario Biocomplexity Project was getting off the ground. That summer, she was introduced to environmental fluid mechanics and to Ithaca, NY, both of which she enjoyed a great deal; Allie is now in Ithaca studying environmental fluid mechanics.

[1]Incidentally, in college, Allie would also fall in love with a physicist, with whom she is still in love.

To water.

ACKNOWLEDGEMENTS

Credit for this research is shared by a large number of individuals and organizations, to whom the author is sincerely grateful. Thanks to everyone involved, and in particular thanks to the following:

Funding: The National Science Foundation for funding this research through the Biocomplexity in the Environment Program (grant numbers OCE-0083625 and CTS-0093794) and for funding the author's studies at Cornell through the Graduate Research Fellowship Program.

Research Site: Fair Haven Beach State Park and the State of New York for allowing us to conduct research in Sterling Pond; the community of Fair Haven for making the field site a pleasant place to work.

Advisors: Todd Cowen, for his guidance and enthusiasm; Francisco Rueda, whose enthusiasm is rivaled only by Dr. Cowen's, for planning field experiments and for sharing his numerical expertise; Bob Johnson for coordinating his research with ours and for going out of his way to support our efforts.

In the Defrees Lab: Kristi Kull and Aaron Blake for launching the Defrees Lab field program and for making the 2002 field experiments happen; P.J. Rusello for becoming the local ADCP expert, for conversations about data analysis, for lifting $150lb$ weights over the side of the Zodiac, for pulling them back in again, and for doing half of the 2003 field experiment; Lee Virtue, Monroe Weber-Shirk, and Cameron Willkens for support in the shop and in the lab; Evan Variano for being

a reliable third set of hands in the field.

On the Biocomplexity Project: Kristi Arend and Becky Doyle for company during Hurricane Isabel and for spearheading collaboration between our groups; Sonia Castanedo, Virginia Pasour, and Nami Tanaka, for help with field work and for shared experience with Si3D; the project staff including Gail Steinhart, Andrea Parmenter, Tom Bell, and Marci Meixler for their amazing support of the project.

In the field: A special thanks to deep cycle marine batteries. Last, but certainly not least, thanks to the Fly By Night Cookie Company of Fair Haven, NY for supplying most of the calories that fueled the above participants as they conducted the following research.

TABLE OF CONTENTS

LIST OF TABLES

LIST OF FIGURES

Chapter 1

Introduction

In this thesis, we primarily document two passive tracer release studies in which we directly measured the residence time distribution of water entering a small embayment (Sterling Pond) from its watershed. Sterling Pond (SP) empties a large watershed into Lake Ontario through a long and narrow manmade channel. From late spring through early fall, SP is populated by diverse species of aquatic macrophytes[1]. The passive tracer studies were designed to accomplish two goals:

1. to directly measure the residence time of water entering SP from its watershed as part of an effort to characterize residence times in coastal embayments for the Lake Ontario Biocomplexity Project, and

2. to decipher the effects of macrophytes on flow and transport through SP and through shallow embayments dominated by macrophytes in general.

To meet both of these goals, we sought to conduct the experiments under different types of hydrodynamic forcing and different macrophyte distributions, both of which we characterized in detail as follows: We conducted the tracer studies in synchrony with extensive surveys of macrophyte density, height, and species composition; meteorological conditions were continuously monitored in the proximity of SP during the tracer studies, as were temperature and water surface elevation on the boundaries of SP and in the pond itself. Bathymetric data was collected in SP, the stream feeding SP, and in Lake Ontario. The tracer experiments, macrophyte surveys, and auxiliary data comprise a benchmark data set that may be used in the

[1]Macrophytes are plants that can be seen without a microscope.

future for development and validation of numerical models of flow through flexible vegetation.

1.1 Lake Ontario Biocomplexity Project

The seminal objective of the work described herein was to characterize residence time scales of Sterling Pond for the Lake Ontario Biocomplexity Project[2], a five year project involving nine principal investigators with expertise in water chemistry, fish, plankton, aquatic macrophytes, forest and wetland ecology, ecosystem modeling, watershed modeling, land use, and hydrodynamics. The broad project goal was to understand how physics, chemistry, biology, and human society interact to shape ecosystems of freshwater embayments, and the central hypothesis was that

> "the average time water takes to move through an aquatic system is a key variable defining the extent that ecosystems are self-organized or dominated by outside influences."

Eight embayments along the southern and eastern coasts of Lake Ontario were chosen as study sites because they encompass a variety of morphological characteristics, including embayment volume, watershed size, degree of connectedness to Lake Ontario, and presence of aquatic vegetation, having transit time scales that are thought to range from a few hours to many years. The sites are pictured in Figure 1.1.

[2]Biocomplexity: Physical, Biological, and Human Interactions Shaping the Ecosystems of Freshwater Bays and Lagoons, NSF award number OCE-0083625, 2001-2005.

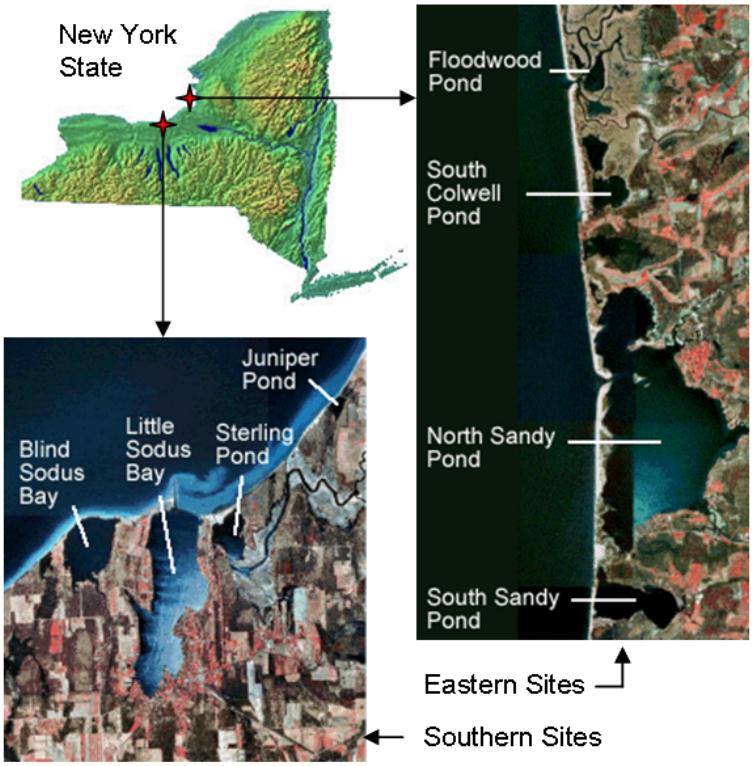

Figure 1.1: Field sites for the Lake Ontario Biocomplexity Project. Photo credit: International Joint Comission.

Our group plays a central role in testing the main hypothesis — characterizing the transport time scales of the eight embayments. The present work grew out of this responsibility, and was facilitated and inspired by collaborations within the project. We have collaborated extensively with Robert Johnson, director of the Cornell Ponds facility, who thoroughly characterized macrophyte populations in Sterling Pond throughout the tenure of the project in pursuit of his own research interests and specifically sampled during our passive tracer release studies to support our efforts.

We have also collaborated extensively with Kristin Arend and Rebecca Doyle to understand the effects of episodic upwelling events in Lake Ontario on the ecosystems of the southern Biocomplexity sites. During the summer and fall of 2003 and 2004, Doyle and Arend led intensive sampling of chemistry, plankton, and fish in Little Sodus Bay, Sterling Pond, Blind Sodus Bay, and neighboring sites in Lake Ontario before, during, and after upwelling events[3]. The embayments were sampled less extensively during a 2002 upwelling event. In 2003, the event occurred during one of the dye studies described in this thesis.

1.2 Transport Time Scales

Aquatic systems may be characterized by a variety of transport time scales, and it is always important to specify exactly which time scale is being discussed and consider carefully what that time scale represents. Monsen et. al. (2002) identify three time scales that describe the bulk transport through a system. *Residence time* is the amount of time a water parcel beginning within (or on the boundary

[3]Coastal upwelling of Lake Ontario was anticipated using the 1-D model of Csanady (1977) and real-time wind data from a NOAA buoy in the center of Lake Ontario.

of) a system takes to exit that system. *Age* is the amount of time a water parcel at a given point and time has spent in the system. *Flushing time* is the amount of time required for a specific fraction (often 0.99 or e^{-1}) of the water in a system at a given time to leave. These time scales are useful as bulk descriptors of different processes. For example, the flushing time of a polluted estuary indicates how long it will take the estuary to clean itself. The residence time of water entering a lake from the surrounding watershed represents the amount of time nutrients from the watershed will be available to the lake ecosystem in an average sense. The age of water at the bottom of a lake during the stratified season may indicate the availability of oxygen for organisms in the hypolimnion. For the purposes of testing the main hypothesis of the Biocomplexity Project, we have focused on residence time, although all of these time scales are relevant to the embayment ecosystems.

Not only does residence time vary with starting location and time, $(\vec{x_0}, t_0)$, but even for a single water parcel beginning at a given $(\vec{x_0}, t_0)$, there is not a single residence time, but a *residence time distribution* (RTD) for the individual molecules within that parcel. In this thesis we will denote the residence time distribution by $r(\vec{x_0}, t_0, t)$, or simply by $r(t)$ when the starting location and time are clear. The first and second moments of the RTD, given in Eqs. 1.1 and 1.2, are the mean and variance of the residence time, and they roughly measure advection and dispersion through the system, respectively.

$$\mu_{RT} = \int_{t_0}^{\infty} t\ r(t)dt \tag{1.1}$$

$$\sigma^2_{RT} = \int_{t_0}^{\infty} (t - \mu_{RT})^2 r(t)dt \tag{1.2}$$

Residence time is the easiest of the three bulk time scales we have discussed to

measure in the field. If a passive tracer of mass m_0 is released instantaneously at time t_0 and locally at $\vec{x_0}$, and the total tracer mass $m(t)$ remaining in the system at time t can be measured continuously, then the residence time distribution $r(t)$ may be computed directly from Eq. 1.3. Eq. 1.3 shows that the RTD is proportional to the rate of mass loss from the system; we derive this equation by observing that the infinitesimal fraction of mass leaving the system at time t, $d(m(t)/m_o)dt$, is equal to the fraction of tracer having residence time t, which is $r(t)dt$.

If the tracer is conservative, then the rate of tracer mass lost from the system is equal to the total tracer mass flux out of the system. Thus, we may directly measure the RTD if we can continuously measure the tracer flux out of all the system exits. If the tracer is well mixed at an exit, i.e. if the tracer concentration $C(t)$ is uniform over the exit plane, then the mass flux of the tracer out of that exit is equal to $\rho_T C(t)Q(t)$ where ρ_T is the tracer mass density and $Q(t)$ is the flow rate of water through the exit. Noting that the initial tracer mass $m_0 = \rho_T V_0$ where V_0 is the initial tracer volume, we derive Eq. 1.4 for directly measuring the RTD in a system having one exit over which the tracer is assumed to be well mixed.

$$r(t) = -\frac{d}{dt}\left(\frac{m}{m_0}\right) = -\frac{1}{m_0}\frac{dm}{dt} \tag{1.3}$$

$$r(t) = \frac{Q(t)C(t)}{V_0} \tag{1.4}$$

If the total mass in the system drops monotonically, then $r(t)$ as defined by Eqs. 1.3 and 1.4 is the probability density function for the residence time (i.e. the RTD). However, if mass re-enters the system through the exit point, for example because of oscillatory flow, then these equations yield negative values and $r(t)$ does not technically represent the RTD. Nevertheless, as discussed in Hilton, et. al.

(1998), the mean of $r(t)$ is the same as the mean residence time even if mass re-enters the system, and we will loosely refer to $r(t)$ as the residence time distribution throughout this thesis.

The probability distribution function, $r(t)$ has a corresponding cumulative distribution function $R(t)$ defined by Eq. 1.5. We refer to $R(t)$ as the cumulative residence time distribution (CRTD), even if it is only loosely a cumulative distribution function (i.e. even if it does not increase monotonically). The CRTD has an interesting physical interpretation: we see in Eq. 1.6 that the cumulative distribution function is equal to the fraction of tracer that has left the system at time t. This is the case even if tracer re-enters the system.

$$R(t) = \int_0^t r(t')dt' \tag{1.5}$$

$$R(t) = \int_0^t -\frac{d}{dt'}\left(\frac{m(t')}{m_0}\right)dt' = 1 - \frac{m(t)}{m_0} \tag{1.6}$$

In summary, to measure the residence time distribution, $r(\vec{x_0}, t_0, t)$, for a tracer released instantaneously at time t_0 and locally at location $\vec{x_0}$ in a system having one exit across which the tracer is fairly well-mixed, we release volume V_0 of the tracer as instantaneously as possible at time t_0 and locally at location $\vec{x_0}$, and then we continuously monitor the water flow rate, $Q(t)$ through the exit and the tracer concentration, $C(t)$, at the exit. Then Eq. 1.4 gives us the RTD, and we may compute the mean residence time using Eq. 1.1 and the CRTD using Eq. 1.5. If $r(t)$ is positive for all t, then $r(t)$ is a true probability distribution of the residence time and we may compute higher order statistics such as the variance given in Eq. 1.2.

While it is much easier to measure residence time directly in large scale field

experiments than either flushing time or age, passive tracer release studies are nonetheless expensive and invasive. It is difficult if not practically impossible to perform multiple tracer releases at the same time in different locations or even at different times that are not sufficiently spaced apart. Modeling can fill in where field studies leave off. As discussed by Monsen et. al. (2002), Hilton, et. al. (1998), Levenspiel (1999), and (indirectly) Chapra (1997), there are a variety of simple models for residence time. If a system is well-mixed, a continuously stirred tank reactor (CSTR) model is appropriate; if the system is dominated by periodic tides, then a tidal prism model is appropriate; if the system is sufficiently one-dimensional, then a simple advection-diffusion model will predict the residence time curve. However, for systems that are not well mixed, dominated by periodic tides, or one dimensional, more complex models are necessary. This was the case for Little Sodus Bay, discussed in the following section, and it is the case for Sterling Pond. We note that residence time distributions measured in the field, being bulk measures of system transport, are excellent checks for the validity of complex models (Hilton, et. al. 1998).

1.3 Previous Work in Little Sodus Bay

Little Sodus Bay (LSB) is one of the four Biocomplexity Project sites on the southeast coast of Lake Ontario (see Figure 1.1). It is a few hundred meters to the west of Sterling Pond, the focus of this thesis. LSB is $3km^2$ in surface area and $6 - 11m$ deep. The watershed covers $9km^2$, excluding the bay, and supplies negligible inflow to LSB. LSB is connected to Lake Ontario (LO) by a shallow ($2 - 3m$ deep), narrow ($75m$ wide), and long ($550m$ long) channel.

To understand the processes that drive flow and transport in LSB and to char-

acterize LSB residence times, our research group carried out a joint program of field studies and numerical modeling. In 2001, Biocomplexity project staff mapped the bathymetry of LSB. In 2002, 2003, and 2004, our group collected wind records and other meteorological data near LSB, measured temperature profiles and water surface elevation continuously in LO near the western Biocomplexity sites, and continuously monitored temperature profiles in LSB itself. We also conducted several experiments in the channel to measure friction-induced mixing. The field data was used to identify the physical processes that dominate transport in LSB, and to develop and verify an existing 3D hydrodynamic model, Si3D, for use in LSB. Si3D was then run using our field data and historical data as boundary conditions to fully characterize the residence times of LSB.

Cowen and Rueda (2004) and Rueda and Cowen (2005a) found that exchange in the LSB channel is the result of a balance where spatial thermal variations (baroclinic forcing), oscillations in the water level (barotropic forcing), friction mixing, wind, and unsteadiness in the forcing are all important. Rueda and Cowen (2005b) showed that baroclinic processes are the dominant transport mechanism in embayments like LSB. The largest density gradients across the channel are caused by episodic upwelling events in LO during the stratified season, when exchange rates increase by at least an order of magnitude. The mean residence time scales undergo dramatic variations in time and space and in general are comparable to the time scales of the system's variability itself, such as those associated with seasonal changes in stratification, allowing complex patterns of intermittent exchange events to determine residence time scales. The temporal variations of mean residence times occur at inter-annual, seasonal, and down to synoptic time scales, and are closely related to the occurrence and frequency of upwelling events in LO.

Chapter 2

Methods

2.1 Study Site

Sterling Pond (SP) is a small and shallow embayment located on the southeast coast of Lake Ontario (LO) in Fair Haven Beach State Park. SP drains a relatively large watershed through Sterling Creek (SC) into Lake Ontario (LO) through a long and narrow maintained channel.

The pond basin is $400m$ wide and $600m$ long in the direction of net through flow, having a surface area of $0.38km^2$. Most of the pond is $1.5m$ deep, but the northeast lobe of the pond reaches a depth of $3m$, and at the mouth of SC, the depth reaches $6m$ (Figure 2.1). The pond basin has a mud bottom, and the bathymetry did not change appreciably over the three year study period.

SP is essentially a natural retention basin for a $200km^2$ watershed (Figure 2.2). The watershed is drained through a network of streams that converge on SC $3km$ before it empties into SP. For one kilometer upstream of SP, SC is approximately $4m$ deep and $40m$ wide. Watershed land cover is primarily forest (44%) and agricultural land (41%)[1], but an ecologically important wetland area borders the last $3km$ of SC and the south side of the SP basin (Figure 2.3).

A $17m$ wide, $2.5m$ deep, $140m$ long channel connects SP to LO. We will refer to this as *the channel*. The channel is lined by concrete and corrugated steel piling, but the bottom is covered with sand from LO. During much of a typical year, flow through the channel changes direction quasi-periodically due to seiching of

[1]Land cover analysis was done by Andrea Parmenter for the Biocomplexity Project.

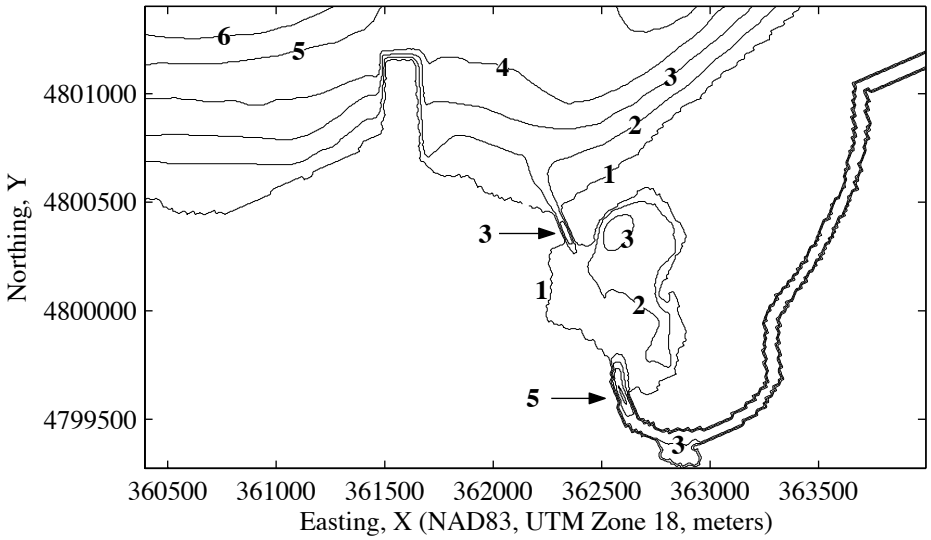

Figure 2.1: Bathymetry of Sterling Pond. Contour labels indicate meters below typical lake level (75m above IGLD85).

Figure 2.2: Sterling Pond and its watershed. The pond is located in the upper left corner, and the watershed is outlined. Map is from the United States Geological Survey.

Figure 2.3: Topographic map of Sterling Pond, showing Sterling Creek and its surrounding wetlands. The pond is filled in dark blue, and wetlands are indicated by dotted blue and white area. Map is from the United States Geological Survey.

LO. In an average sense, flow through the channel is from SP to LO, but only after periods of substantial rainfall, when watershed flow is high, is this true for a sustained period of time. Coastal upwelling of LO has been observed to result in bi-directional flow through the channel in which cold water from the LO hypolimnion flows into SP along the bottom and warmer SP water flows out into LO on the top.

From late spring through early fall, SP is home to diverse populations of aquatic macrophytes which experience one or more dense blooms. The species composition, density, and spatial distribution of the macrophyte canopy varies dramatically throughout the growing season and from year to year.

SP is just $100m$ east of Little Sodus Bay (LSB), the Biocomplexity site studied by Rueda and Cowen. The systems are similar in that they are both connected to LO by a maintained channel, but SP is a smaller embayment with a much larger watershed, and LO is too deep to sustain a significant macrophyte population. From our findings in LSB, we expect the hydrodynamics and resulting water residence times of SP to be determined in large part by barotropic and baroclinic forcing

from LO, but we also expect watershed flows and the macrophyte canopy to play significant roles. Thus, SP is a more complicated system than LSB, and it is an excellent laboratory for studying flow and transport through variable distributions of aquatic vegetation under different forcing conditions.

2.2 Overview of Field Experiments

Toward the goal of characterizing the residence time scales in SP, we conducted two passive tracer release studies in which we directly measured the residence time distribution of a water parcel entering SP from the surrounding watershed at the mouth of SC. During the tracer studies, macrophyte distributions were characterized in detail throughout the pond. Residence time is a good bulk measure of flow and transport, but to understand more fully the physical processes in SP and in particular to decipher the effects of the macrophytes, we measured or otherwise obtained several other relevant variables including meteorological data, water surface elevations, temperature profiles, and bathymetry in SP, LO, and SC. Throughout this thesis, we will refer to the two tracer studies as the 2002 and 2003 dye experiments, corresponding to the experiments conducted from May 15 – 16, 2002 and from September 18 – October 6, 2003, respectively. Locations of the field equipment are mapped for each of these tracer studies in Figures 2.4 and 2.5, and GPS coordinates are given in Tables 2.1 and 2.2.

2.2.1 Passive Tracer Release Studies

In two passive tracer release studies ("dye studies"), we measured the residence time distribution, $r(t)$, of water entering SP from the surrounding watershed by carrying out the following three-part procedure:

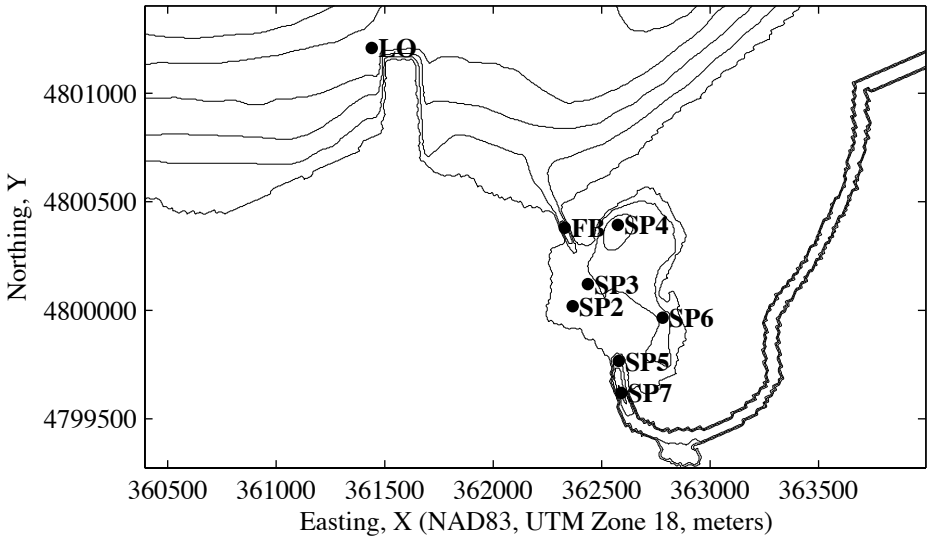

Figure 2.4: Equipment locations for the 2002 tracer study. GPS coordinates are given in Table 2.1

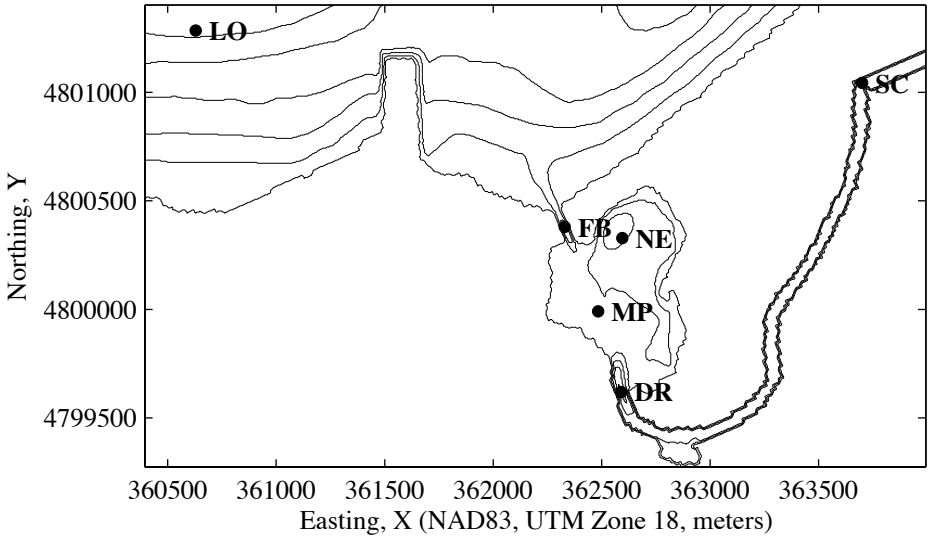

Figure 2.5: Equipment locations for the 2003 tracer study. GPS coordinates are given in Table 2.2

Table 2.1: GPS coordinates of field equipment deployed during the 2002 dye study. Coordinates are referenced to NAD83 and UTM Zone 18 (meters).

Site	Northing	Easting
LO	4801209	0361440
FB	4800380	0362330
SP2	4800020	0362365
SP3	4800120	0362436
SP4	4800394	0362573
SP5	4799766	0362578
SP6	4799966	0362780
SP7	4799620	0362590

Table 2.2: GPS coordinates of field equipment deployed during the 2003 dye study. Coordinates are referenced to NAD83 and UTM Zone 18 (meters).

Site	Northing	Easting
LO	4801285	0360629
FB	4800380	0362330
NE	4800328	0362595
MP	4799990	0362484
DR	4799620	0362590
SC	4801043	0363700

1. Release volume V_0 of a passive tracer instantaneously at a point where SC empties into SP (site SP7 in 2002 and site DR in 2003).

2. Continuously monitor outflow, $Q(t)$, from SP into LO in the center of the channel connecting SP to LO (site FB in 2002 and 2003).

3. Continuously monitor concentration, $C(t)$, of the tracer at the outflow monitoring site.

As discussed in Section 1.2, a residence time distribution is specific to a particular release site and time, so we considered carefully the time and place at which to release the tracer. We sought to conduct the dye studies under different conditions of hydrodynamic forcing in order to have some small measure of how residence time varies throughout the year. We chose the point where SC meets SP as the tracer release site because in an average sense, flow through SP is from the watershed to LO, so the most important residence time is arguably that of water entering SP from its surrounding watershed. Because the cross-section where SC meets SP is relatively narrow ($40m$ wide) and the watershed empties into SP primarily through SC, the single point tracer release is representative of nutrients and pollutants entering SP from the entire watershed provided that flow is in fact from the watershed to LO. In reality, during the 2003 tracer study, dye was observed to wash up to $500m$ upstream from the release site into SC. Thus, because we monitored the dye flux out of SP at the channel only, we technically measured the distribution of residence times in a system that includes part of SC as well as the SP basin, and our dye release site was not on the boundary of this system. Nevertheless, our residence time distributions are in an approximate sense representative of distributions for nutrients and contaminants entering SP from the watershed. The

residence time distribution of water entering SP from LO is also interesting and ecologically important, but it is considerably more difficult to measure, primarily because LO is so big that a particular point release is not representative of inflow from LO in general. In the future, we hope to numerically model tracer releases in LO and thus estimate residence times without the practical impossibility of such a large-scale tracer release in the field.

2.2.2 Macrophyte Surveys

The Biocomplexity research group let by Principal Investigator Robert Johnson conducted extensive macrophyte surveys in SP characterizing species composition, dry weight, abundance, and height from the bottom in $100m \times 100m$ quadrates throughout the pond basin. Surveys were conducted throughout the growing season, beginning in late spring and continuing through the fall between 2002 and 2004. In particular, we are interested in the surveys conducted on May 23, 2002 and on September 25, 2003. The May 23, 2002 survey was conducted seven days after the 2002 dye release, and the September 25, 2003 survey was conducted in the middle of the 2003 dye study.

2.2.3 Supporting Data

In order to characterize the physical conditions determining flow and transport in SP, and to provide boundary conditions and initial conditions for the purposes of future 3D modeling, we collected continuous records of meteorological, temperature, and water surface elevation both during the three dye studies and during large parts of the summer and fall of 2002, 2003, and 2004. We additionally collected bathymetric data in SP and SC and purchased bathymetric data from near-shore

LO. Only data collected during the two dye studies is presented in this thesis, but all of the data is available by request from the author.

2.3 Physical Conditions During the Dye Studies

A brief summary of the background physical conditions during each of the passive tracer studies is given in Table 2.3. The field data from which we summarize these conditions is presented in Chapter 4.

Table 2.3: Environmental conditions during each of the dye experiments.

	Lake Ontario
2002	Negligible effect – favorable water surface gradient for draining SP.
2003	Very strong barotropic forcing due to high winds during and after hurricane Isabel; short upwelling event observed September 22 – 24.
	Sterling Creek
2002	High flow ($15 m^3/s$ average)
2003	Low flow ($0.3 m^3/s$ average)
	Macrophytes
2002	Sparse vegetation concentrated in the northeast lobe of SP; did not reach the water surface.
2003	Extremely dense vegetation reaching the water surface; density was fairly uniform across the pond.

2.4 Passive Tracer Releases

Our passive tracer of choice was rhodamine WT (RWT), a red fluorescent dye. We positioned a line source diffuser in $5m$ of water at the dye release site (SP7 in Figure 2.4 and DR in Figure 2.5). Dye was pumped from a $20L$ Nalgene cannister on the west shore of SP through $1/2in$ diameter polyethylene tubing into the line source diffuser which was itself a strip of $1/2in$ polyethylene tubing having circular perforations every inch and a plug at the bottom. The diffuser was held in a vertical orientation with a buoy at the top and a weight at the bottom. In the 2002 experiment, we released $1gal$ of 20% RWT solution that had been further diluted in $20L$ of water. In the 2003 study, we released $2gal$ of 20% RWT that had not been diluted further[2]. After emptying the Nalgene cannister of dye, we ran another cannister of clean water through the tubing and the diffuser to wash out any remaining dye. The start time, end time, and end-of-rinse time for each study are given in Table 2.4. The final column of the table indicates the time which we take to be the "time of release" for the purpose of computing residence time distributions – note that this time is given in decimal days, for which day zero is midnight of January 1. The time axes of most plots in this thesis also refer to decimal days.

[2]It is best to dilute RWT in order to better match the density of water – the 20% solution has a specific gravity of 1.15, so in the 2003 experiment the negative buoyancy of the dye was significant. Failing to dilute the solution was an error on the part of the investigators.

Table 2.4: Dye release times. Note that all times here and throughout this thesis are referenced to Eastern Daylight Time (EDT), and the "time of release" is given in decimal days.

Date	Start	End	End of Rinse	"Time of Release"
May 15, 2002	1:02 PM	1:16 PM	1:19 PM	134.54896
September 18, 2003	6:31 PM	6:36 PM	6:55 PM	260.77986

Figure 2.6: Footbridge over the channel that connects Sterling Pond (to the left) to Lake Ontario (to the right).

2.5 Outflow Measurements

During each of the dye experiments, outflow from SP to LO was measured in the center of the channel connecting SP to LO. Conveniently, there is a footbridge crossing the channel exactly half-way between SP and LO. This footbridge, pictured in Figure 2.6, was used to stage our outflow (and dye concentration) measurements. A view of the channel and SP from the footbridge is pictured in Figure 2.7.

Underneath the footbridge, the channel is $17m$ wide and $2-3m$ deep depending on the water level. It is impossible to directly measure outflow through such a big cross-section. Our approach was to continuously monitor the vertical profile

Figure 2.7: Photo of the SP channel taken from the footbridge, facing toward SP and away from LO.

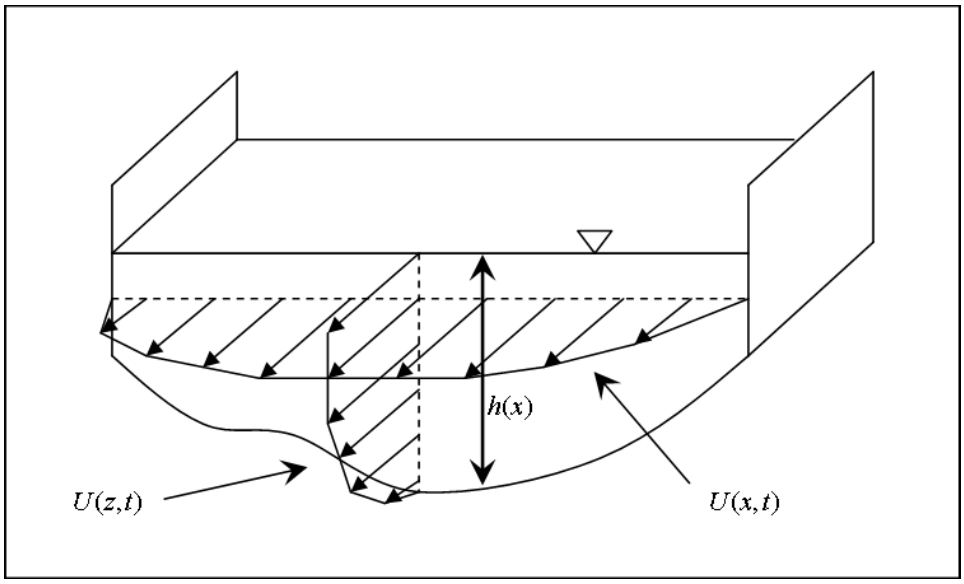

Figure 2.8: Schematic of the three measurements used in our estimation of outflow: Vertical velocity profile measured near the channel centerline, $U(z,t)$; horizontal velocity profile measured in the upper half of the channel, $U(x,t)$; and channel depth across the cross section, $h(x)$.

of velocity in the center of the channel using an RDI $1200kHz$ Workhorse Monitor acoustic Doppler current profiler (ADCP), characterize the horizontal velocity profile in the upper half of the channel in a one-time experiment using an RDI $600kHz$ Workhorse Monitor ADCP, and measure the bathymetry of the channel under the footbridge. From these three measurements, we estimate the total outflow through the cross-section. A schematic of the three measurements used in our estimation of outflow is shown in Figure 2.8.

2.5.1 Channel Bathymetry

A single bathymetric transect was taken in the channel cross-section underneath the footbridge on August 2, 2004. This was a year after our last tracer study, and shortly after the horizontal boundary layer measurement. The bathymetry of the channel is plotted in Figure 2.9. The width of the SP channel is $2D = 16.9m$ and

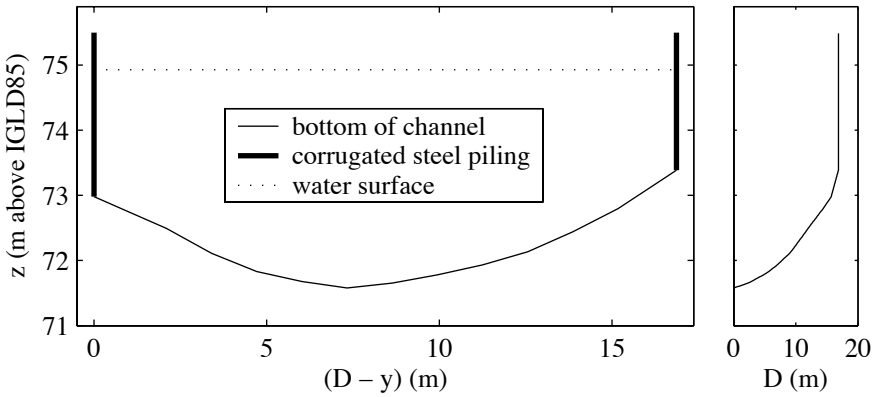

Figure 2.9: Bathymetry of the channel that connects SP to LO. Transect was taken on August 2, 2004.

the depth in the middle is about $2.5m$, depending on the water surface elevation.

2.5.2 Vertical Velocity Profiles

Throughout each of the dye studies, a vertical profile of the 3D velocity vector, $\vec{u}$, was measured in the center of the channel that connects SP to LO with an RDI Workhorse Monitor $1200kHz$ acoustic Doppler current profiler (ADCP). The ADCP was anchored to the center of a $1m$ by $1m$ square frame and lowered to the bottom of the channel from the footbridge. We will discuss the vertical velocity profile measurement for the 2003 experiment first because in 2003 the ADCP was operated in a high resolution pulse-coherent mode and the data from 2003 was used to improve the data from 2002.

2003

In 2003, the $1200kHz$ ADCP was configured in mode 11, a pulse-to-pulse coherent mode that was developed to make velocity measurements with very low noise or in very small bins. The ADCP was cabled to shore, powered by $12V$ deep cycle marine batteries, and data was recorded by a laptop computer. At the beginning

of the experiment, the ADCP was set up to record data in 75 bins of $5cm$ height, but because the data was noisy in this configuration, the ADCP was reconfigured to collect data in 255 bins of $1cm$ height for the rest of the experiment. We note that in the investigators' experience, larger bins result in noisier data for mode 11. Data was collected at a time interval of $5.56s$ with the ADCP pinging at the maximum possible rate. A correlation filter was applied during data collection, throwing out data with correlation under 40 (this is a tight filter, the default being 65, but did not result in much data loss). The ambiguity velocity, which is roughly the upper limit for velocity measurements, was set to $70cm/s$. Every ping was recorded, i.e. no ensemble averaging was performed during data collection. Using its internal compass, the ADCP continuously measured its own heading, pitch, and roll. Velocities were recorded in beam coordinates and transformed to earth coordinates (North-East-Up-Error) using WinADCP, a software package from RDI. All further analysis was performed using velocity in earth coordinates.

2002

For the 2002 experiment, the $1200kHz$ ADCP was configured in mode 1. Mode 1 is the default operating mode. It is robust in high velocities (over $1m/s$) and in high shear, but disadvantages are that that mode 1 requires large bins and suffers from high per-ping uncertainty compared to pulse-coherent modes. We collected $6s$ ensemble averages of 20 pings each in $25cm$ bins over a range of $4.5m$, beginning $0.75m$ above the transducer face. Note that we had bins far above the water surface, which is about $3m$ above the bed – this is because we were not sure how deep the water in the channel could get during periods of high runoff. For this experiment, we recorded velocities in earth coordinates, but we also recorded

the heading, pitch, and roll of the ADCP. We enabled bin mapping. The ADCP was powered by an internal battery pack and recorded to memory.

2.5.3 Horizontal Velocity Profiles

A single experiment was conducted on July 29, 2004 to characterize the horizontal velocity profile in the SP channel. The setup for this experiment is shown in Figure 2.10. A $600kHz$ RDI Workhorse Monitor ADCP was positioned a few meters to the south of the footbridge on the east wall of the SP channel with its transducers looking towards the west wall of the channel (in the positive y direction).

The walls of the channel are lined with corrugated steel piling, and the ADCP was bolted to two long two-by-fours that were placed flush with the crest of the piling on the east wall so their feet rested on the bottom of the channel. The top of the two-by-fours was clamped to the top of the piling. The ADCP was oriented so that beams 3 and 4 were in the horizontal plane with their bisector pointing straight across the channel. The center of the transducer face was $30cm$ in the cross-channel direction from the crest of the steel piling and $97cm$ below the water surface; the water surface elevation was $75.05m$ above IGLD85 when we measured this depth (according to NOAA CO-OPS[3]). Beams 1 and 2 were blocked with acoustic foam (left unblocked, these beams reflected off of the water surface and the bed, and the reflected signal was picked up by transducers 3 and 4). The ADCP was configured in mode 1 to sample at $3.125Hz$ with one ping per ensemble in 38 bins of $50cm$ width for $4.7hrs$.

[3]National Oceanic and Atmospheric Administration's Center for Operational Oceanographic Products and Services (http://tidesandcurrents.noaa.gov).

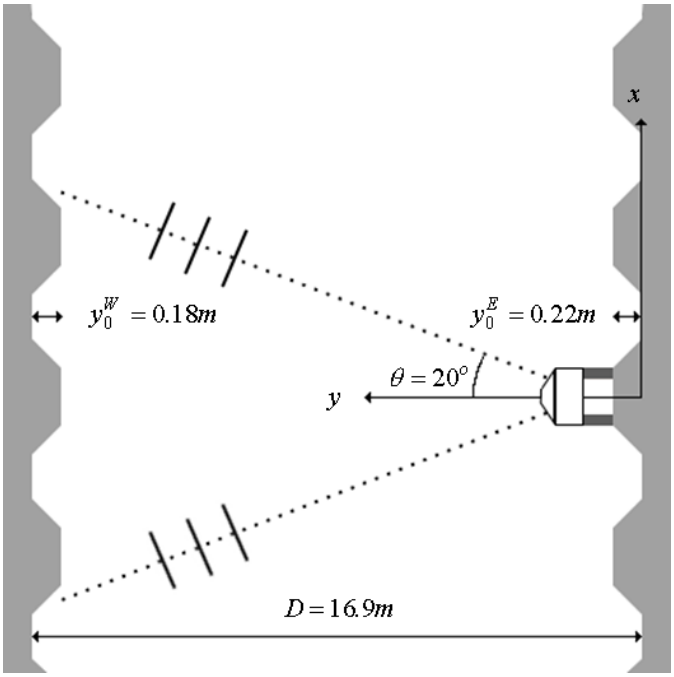

Figure 2.10: Setup of 2004 horizontal boundary layer experiment.

2.6 Concentration Measurements

For each of the field experiments, dye concentration was monitored continuously in the middle of the channel connecting SP to LO with a flow-through fluorometer. Monitoring of concentration began shortly before each dye release and continued until most of the dye had exited SP. This section covers details of the monitoring setup, fluorometer configuration, calibration, post-calibration, and data analysis resulting in our estimate of dye concentration at the exit boundary of SP for each experiment. As for outflow, our concentration measurement was best for the later dye experiment, and we will describe the best experiment first.

2.6.1 Equipment Setup

2003

A Turner Designs 10-AU flow-through fluorometer with temperature correction package was used to monitor Rhodamine WT (RWT) concentration at $1Hz$ throughout the 2002 and 2003 experiments. The 10-AU is an accurate and robust field fluorometer that reliably holds its calibration for months provided that the flow cell is kept clean. The setup of the monitoring system is shown in Figure 2.11. The goal was to measure the concentration of RWT and outflow at the same location, so the 10-AU was placed next to the footbridge under which the $1200kHz$ ADCP was deployed. The intake of a garden hose was positioned near the middle of the channel at mid-depth. The garden hose was connected to a submersible centrifugal pump that drew water into the 10-AU flow cell through $3/8in$ ID polyethylene tubing. Water was discharged from the flow cell through the same type of tubing. All of the polyethylene tubing was covered with duct tape to shade the flow cell from

sunlight, as specified in the 10-AU manual. A plastic, cylindrical ($10cm$ diameter, $15cm$ length) intake filter was screwed onto the intake of the garden hose to filter out plant matter and prevent clogging of the pump. With this setup, the flow rate was measured to be $107mL/s$, and the travel time between the intake filter and the 10-AU flow cell was estimated to be $21s$. The 10-AU was connected via serial cable to a laptop that recorded data every second. The 10-AU, submersible pump, and laptop were provided with AC power by two DC/AC inverters running on $12V$, $95Amp-hr$, deep cycle marine batteries. Six batteries were wired in parallel and swapped with six freshly recharged batteries on a 12 hour cycle to keep the experiment running for 17 days. The $1200kHz$ ADCP was powered directly from the same batteries, and its accompanying laptop was set up next to the 10-AU laptop. The computers and batteries were stored in waterproof plastic tubs and the whole setup was covered with a waterproof tarp. The tub containing the computers was chained shut, and the 10-AU was chained to the footbridge to prevent robbery.

2002

For the 2002 experiment, we used the 10-AU as well. The setup was similar to the 2003 setup. The one significant difference was that during the 2002 experiment, we did *not* cover the 10-AU intake and discharge tubing with opaque material to shield the flow cell from changing light conditions. In Section 2.6.5, we discuss the repercussions of this oversight.

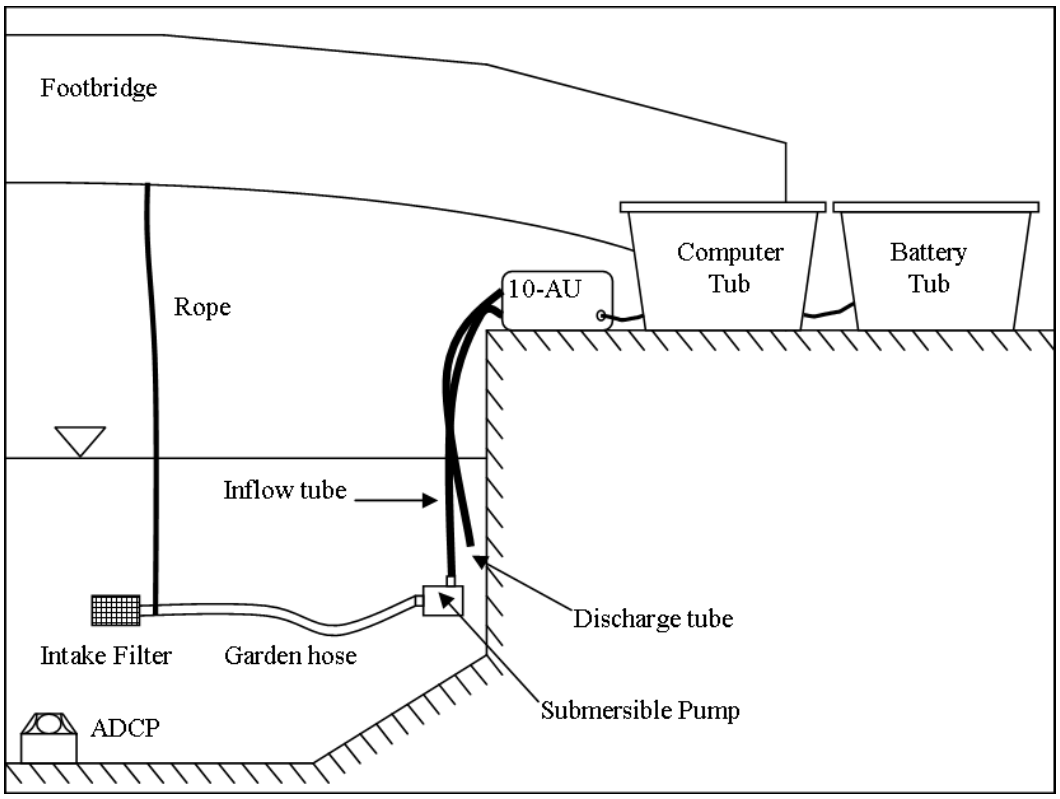

Figure 2.11: Setup for measuring concentration of RWT in 2003.

2.6.2 Calibration

2003

A few hours before the dye release, the 10-AU was calibrated against a blank and a standard in a $5gal$ glass fish tank following the procedure in the 10-AU manual. For the calibration, the garden hose and intake filter were removed from the pump, and the pump was placed in the fish tank as was the end of the discharge tube. A known volume of water from the SP channel was used as the blank, and a solution of RWT (made from the source) was added to the blank to make a standard solution of $20.0ppb$. Note that the pump, tubing, and 10-AU flow cell were dry at the beginning of the calibration so the volume of water involved in the calibration was not altered when the pump was primed.

2002

The 10-AU calibration procedure for the 2002 experiment was similar to that of the 2003 experiment. Suspiciously, however, the 10-AU reading for the first $2.5hrs$ after the dye release was approximately $-0.8ppb$. This strongly suggests that some RWT contaminated the fish tank or the 10-AU tubing during the blank.

2.6.3 Post-Calibration

2003

On October 6, at the end of the 2003 dye experiment, we performed the following set of post-calibration measurements. Before moving the 10-AU setup, we decided to test whether the garden hose and intake filter, which were quite dirty by the end of the experiment, had altered the concentration readings at all. We measured

the concentration in situ, just as we had during the entire dye experiment, and simultaneously collected a water sample from near the intake filter. We put this water sample into the fish tank, disconnected the hose and intake filter from the 10-AU piping, placed the pump and the end of the discharge tube in the fish tank, and measured concentration again. In situ, the 10-AU reported a concentration of $0.895 \pm 0.001 ppb$, and in the fish tank, the 10-AU reported a concentration of $0.875 \pm 0.001 ppb$. Note that for the above and following post-calibration concentration measurements, 95% confidence intervals are reported for bootstrap computations of mean concentration – see Efron and Tibshirani (1993) – and (with the possible exception of the in-situ measurement) they represent uncertainty due to instrument sensitivity.

We obtained a post-calibration blank from Lake Ontario by dipping a $10 gal$ jug into the water off the northern tip of the channel piling of Little Sodus Bay. Without moving the 10-AU setup from the footbridge, we disconnected the garden hose and the intake filter, ran the pump dry for a few seconds to empty the tubing and flow cell of water, and then put the pump and tubing into the fish tank with the LO blank. The concentration measured by the 10-AU for the LO blank was $0.459 \pm 0.003 ppb$, significantly above the $0 ppb$ we were hoping for.

Next, we added a post-calibration solution of RWT (mixed from Bright Dyes FWT Red 25 liquid dye) in three stages to the LO blank to make concentrations of $3.0 ppb$, $6.0 ppb$, and $9.0 ppb$. The 10-AU reported concentrations of $3.156 \pm 0.003 ppb$, $5.839 \pm 0.004 ppb$, and $8.411 \pm 0.005 ppb$, respectively.

Finally, we took the 10-AU back to the Defrees Hydraulics Laboratory at Cornell and observed the 10-AU reading for distilled water in the fish tank. Whereas normally, during the fish tank measurements, the 10-AU concentration reading will

spike as the pump primes and level out after about $30s$ to $1min$, in this case the concentration began at $0.50ppb$ and after $15min$ finally leveled out at $0.44ppb$. By the time the concentration had leveled out, the water in the fish tank was visibly dirty. We drained the 10-AU of water, opened its casing, and observed that the inside of the glass flow cell was also visibly dirty. We closed the casing, ran a new batch of distilled water through the 10-AU, and this time the concentration reading started at $0.37ppb$ and leveled out at $0.34ppb$ after $15min$. We replaced the dirty water with fresh distilled water once more, and this time the 10-AU gave a stable reading of $0.31ppb$ for $5min$. It appeared that the distilled water had cleaned the flow cell to some extent but had reached an impasse. Finally, we added some bleach to the distilled water and ran the pump continuously. After an hour, the concentration reading stabilized at zero.

2002

For the 2002 experiment, we did not do any post-calibration of the 10-AU. Because the 10-AU holds its calibration accurately for months and because this experiment was too short for grime to have accumulated inside the tubing and flow cell to bias the 10-AU, we need not worry about calibration drift during this experiment. However, it would have been helpful to perform a post-calibration measurement in distilled water to confirm that the negative readings were the result of a contaminated blank at calibration.

2.6.4 Background Fluorescence

It is good practice to monitor a dye release site for background fluorescence prior to a dye study – for discussion, see Smart and Karunaratne (2002). We did not

perform background flourescence measurements prior to any of our experiments, but we did collect water samples from the SP channel at weekly intervals during the summer of 2004, beginning around 9 months after the 2003 dye study. These grab samples were analyzed in an SLM 8000c cuvette-based spectrofluorimeter, calibrated with a 3.0ppb solution of RWT, at the Cornell Microscopy, Imaging, and Fluorimetry Facility (160a Biotech). No fluorescence was detected in the RWT band from any of the samples.

2.6.5 Sunlight Bias

We conducted a day-long experiment to investigate the impact of changing light conditions on 10-AU readings when the tubing is uncovered. We picked a day with similar weather to that of the May 15, 2002 dye release: May 24, 2006, a sunny day with very few clouds. The 10-AU was set up on the roof of Hollister Hall in Ithaca, NY with uncovered polyethylene tubing facing to the east (same orientation as for the 2002 dye experiment). The instrument was calibrated with a distilled water blank and a 5ppb standard RWT solution at 9:30AM. The 5ppb solution was mixed by eye (from the author's memory of what 5ppb looks like in a 14gal fish tank) because the source RWT was thought to have decayed significantly. The 10-AU was run in alternate blank and 5ppb solutions throughout the day until sunset. The 5ppb solutions were mixed with the same volumes of RWT source solution and fish tank water as the original calibration standard. We observed a maximum 0.16ppb bias in the blank reading with changing light conditions (the concentration reading dropped with lower light); multiplicative bias in the standard solution was not observed within the uncertainty of the solution concentration.

2.7 Macrophyte Surveys

Roughly twice a month during the growing seasons of 2002, 2003, and 2004, and within one week of each dye study, Johnson's research group conducted surveys of macrophyte species composition, dry weight, and height on a sampling grid of $100m \times 100m$ quadrates (plotted in Figure 2.12). Macrophytes were hand-harvested by diving and cutting the stems at the substrate-water interface. Samples were taken from a $0.25m \times 0.25m$ square frame randomly tossed in each quadrate. Stem lengths were measured in the field. Species were separated in the lab and dried for 48 hours at 105^oC to determine dry biomass on a per-species basis.

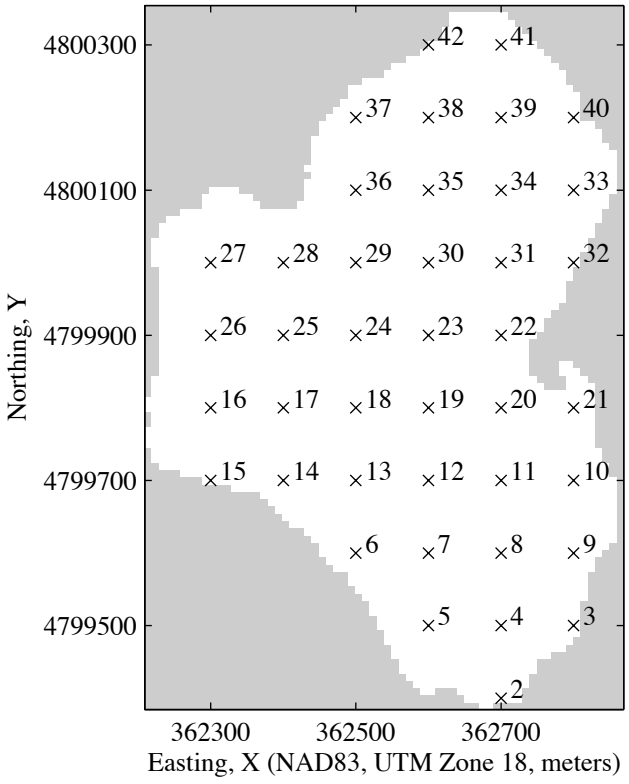

Figure 2.12: Macrophyte sampling quadrates – the center of each $100m \times 100m$ quadrate is labeled.

2.8 Supporting Data

2.8.1 Bathymetry Measurements

There were four sources of bathymetry data for Sterling Pond, Sterling Creek, and the adjacent part of Lake Ontario:

1. Canoe transects in the pond basin
2. ADCP transects in the channel and stream
3. Shoreline data
4. LO bathymetry data

The first two sets of bathymetry data were collected by Biocomplexity project staff and interns during the summer and fall of 2001. All of the horizontal coordinates for this data were collected using hand-held GPS with $10m$ accuracy or better. Depths were measured from the water surface and later referenced to the International Great Lakes Datum (IGLD85) by subtracting from the mean LO water level recorded by NOAA CO-OPS in Oswego Harbor on the date of collection.

The basin of the pond, the channel that connects SP to LO, and the 3 km of SC just upstream of SP were mapped from a canoe with a $15ft$ extendible depth gage on a roughly $15m \times 15m$ grid. The biggest source of error was probably the ambiguity of the bed location due to the mud bottom, and a rough estimate of the 95% confidence interval is, based on the author's memory of judging where the bottom was by poking it with a depth gage, $+/-25cm$. Fluctuations in lake level are also significant, but never exceeded $9cm$ on the days the data was collected, and were typically less than $4cm$.

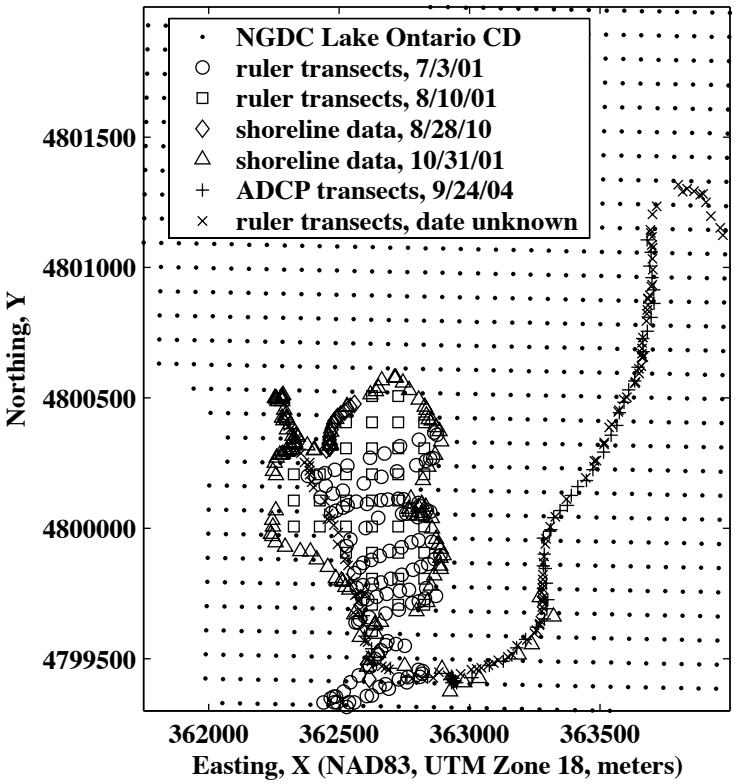

Figure 2.13: Horizontal coordinates of bathymetric data used to create the bathymetric map of SP.

The location of the shoreline of the pond basin was mapped by continuously recording coordinates with a hand-held GPS while walking around the pond on foot. Data from the pond basin and the shoreline was interpolated using GIS data by Biocomplexity staff, and provided to the author on a $5m \times 5m$ grid. In the summer of 2003, the $1.5km$ of SC just upstream of SP were mapped with a $600kHz$ RDI ADCP from the side of a boat that made zigzag transects. The location of the shoreline was noted as a percentage of the channel width traversed by the boat. Lake Ontario near-shore bathymetry data was obtained from the NGDC[4] on CD. This data is on a $75m \times 75m$ horizontal grid.

Horizontal locations of all raw bathymetry data are plotted in Figure 2.13. The reference ellipsoid is NAD83, and coordinates are given in units of meters in UTM Zone 18. Data was converted to these coordinates using Corpscon, a free software package from the U.S. Army Corps of Engineers.

2.8.2 Meteorological Measurements

Shortwave radiation, air temperature, relative humidity, barometric pressure, wind speed, and wind direction were all measured at a weather station mounted on a concrete dock in an unsheltered area over LSB (Figures 2.14 and 2.15). Between the weather station and SP are about $150m$ of land, including a small hill (about $10m$ high), a few trees, and a one-story building.

Sensors were wired to a Campbell Scientific CR10X data recorder with 128K memory and powered by a $10W$ MSX10 solar panel with a PS12LA power supply. The power supply included a charging regulator and a $7Amp-hr$ $12V$ battery.

[4]The National Oceanic and Atmospheric Administration's National Geophysical Data Center.

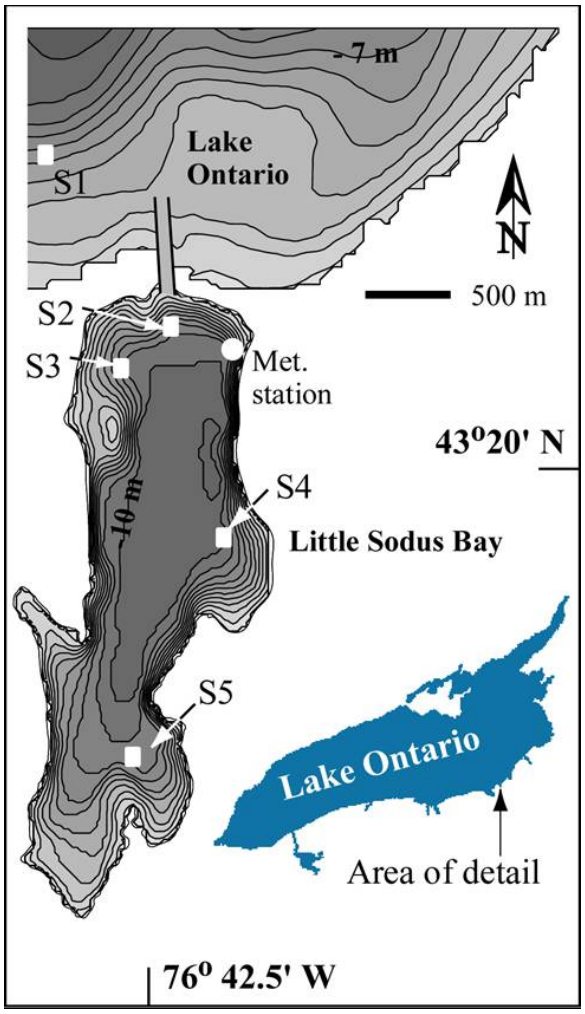

Figure 2.14: Map of Little Sodus Bay, including location of the weather station. Used with permission of Francisco Rueda.

Figure 2.15: Weather station next to LSB.

Data was averaged and recorded every $15min$.

Total radiation (direct solar plus sky radiation) was measured with a LI-COR LI-200SZ pyranometer. This sensor detects light in the $400 - 1100nm$ waveband, and manufacturer specifications indicate that it has a maximum absolute error of $\pm 5\%$, a typical absolute error of $\pm 3\%$, and a drift of $< \pm 2\%$ per year on a full scale of $0 - 3000W/m^2$.

Air temperature and relative humidity were measured with a Vaisala HMP45AC temperature and relative humidity probe. Manufacturer specifications indicate that the temperature is accurate to $\pm 0.3^oC$ in the $0 - 40^oC$ range and the relative humidity is accurate to $\pm 3\%$ in the $0 - 100\%$ range with a drift of $< 1\%$ per year.

Barometric pressure was measured with a CS105 barometer using Vaisala's Barocap^{TM} silicon capacitive pressure sensor. Campbell Scientific reports an accuracy of $\pm 2mb$, repeatability of $\pm 0.05mb$, and long term stability of $\pm 0.1mb$ per year. Note that $0.05mb$ corresponds to about $0.5mm$ of water, so relative pressures are highly accurate for the purpose of computing water surface elevations (see Section 2.8.4). However, the data logger was mistakenly programmed so that pressure

sensitivity is $1mb$, which corresponds to about $1cm$ of water. Since atmospheric pressure changes of about $20mb$ tend to take place fairly smoothly over several days, linear interpolation of the pressure record improves accuracy.

Horizontal wind speed and direction were measured with an R.M. Young 05103-5 wind monitor mounted on a schedule 40 pipe so that wind direction was recorded in degrees clockwise from magnetic west, using the convention that wind direction indicates the direction from which the wind originates. During the period of study, the declination of the earth's magnetic field at SP was 12.4^o west of true north[5], so 282.4^o was added to the measured wind direction in order to reference wind direction to true north (i.e. wind directions are reported in degrees clockwise from true north).

2.8.3 Temperature Measurements

During each of the dye studies, temperature profiles were measured using underwater temperature recorders (thermistors). In SP and SC, the thermistors were deployed as sketched in Figure 2.16. During the short 2002 experiment, the LO thermistors were deployed using this same setup, but between the 2002 and 2003 experiments, the entire LO deployment apparatus was dragged by surface waves for several kilometers during a period of high winds, so we designed a system to allow for slack between the surface buoy and the weight at the bottom. This improved setup, sketched in Figure 2.17, was used in the 2003 LO thermistor deployment.

At each measurement site (see Figures 2.4 and 2.5), thermistors were deployed at multiple depths. These thermistor depths, along with the total depth at each

[5]From the NGDC online magnetic declination calculator (http://www.ngdc.noaa.gov/seg/geomag/jsp/Declination.jsp).

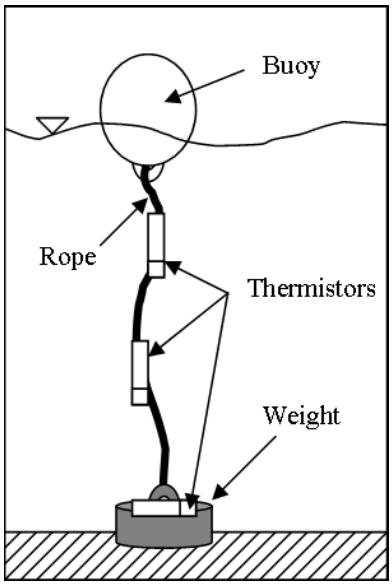

Figure 2.16: Deployment setup for thermistors and pressure recorders in SP and SC.

Table 2.5: Water depth and thermistor depths at each temperature profile site for the 2002 dye experiment. Depths were estimated from the water surface at the time of deployment.

Site	Water Depth	Instrument Depths
LO	$6.0m$	$1.5m$, $2.5m$, $3.5m$, $5.0m$, $5.5m$
SP2	$1.2m$	$0.5m$, $1.0m$
SP3	$1.2m$	$0.5m$, $1.1m$
SP4	$3.0m$	$0.5m$, $1.5m$, $2.5m$, $2.9m$
SP5	$2.7m$	$0.5m$, $1.5m$, $2.5m$
SP6	$1.2m$	$0.4m$, $1.0m$
SP7	$3.7m$	$0.5m$, $1.4m$, $2.1m$

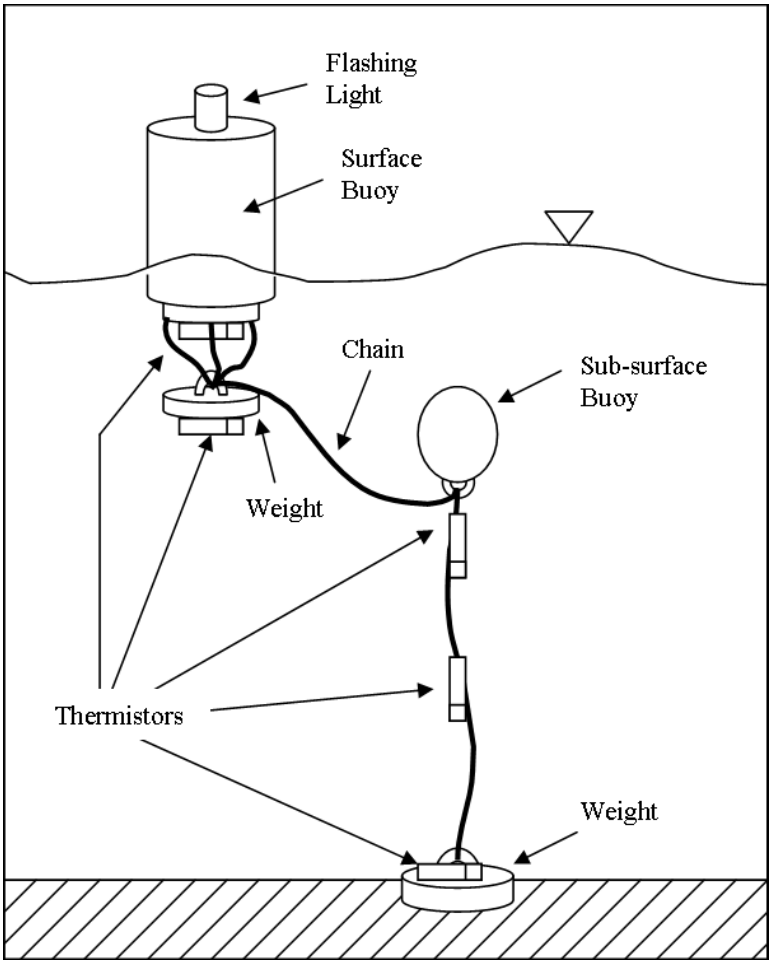

Figure 2.17: Deployment setup for thermistors in LO.

Table 2.6: Water depth and thermistor depths at each temperature profile site for the 2003 dye experiment. Depths were estimated from the water surface at the time of deployment.

Site	Water Depth	Instrument Depths
LO	$6.0m$	$0.5m$, $2.0m$, $4.0m$, $6.0m$
FB	$1.5m$	$0.2m$, $0.9m$, $1.4m$
NE	$2.5m$	$1.0m$, $2.5m$
MP	$0.8m$	$0.2m$, $0.8m$
DR	$3.0m$	$1.0m$, $2.4m$, $3.0m$
SC	$4.0m$	$0.5m$, $2.0m$, $3.9m$

site, are given in Tables 2.5 and 2.6 for the 2002 and 2003 deployments, respectively. Depths are estimated from the water surface.

All temperatures were recorded at a frequency of $1min^{-1}$. All but one temperature time-series were measured with Sea Bird Electronics SBE39 temperature recorders. These instruments have an initial accuracy of 0.002^oC and a typical drift of less than 0.002^oC per year. They have a watch-crystal internal clock that drifts less than 15 seconds per month, and the clock is set shortly before deployment. An In-Situ miniTROLL pressure/temperature recorder was used to measure temperature at the SC $3.9m$ site during the 2003 deployment. The miniTROLL thermistor has a manufacturer reported accuracy of $\pm 0.25^oC$.

2.8.4 Water Surface Elevation Measurements

Water surface elevations were measured using a combination of underwater pressure sensors and a barometer. The underwater sensors measured absolute pressure, and barometric pressure was subtracted to find gage pressure. The underwater pressure sensors also recorded temperature, and depths were computed from absolute underwater pressure, barometric pressure, and water column temperature as explained in Section 3.2.

The barometer was a component of the weather station (see Figure 2.14) and is discussed in Section 2.8.2. It is assumed that atmospheric pressure was uniform across the field site.

Some of the temperature recorders discussed in Section 2.8.3 included a pressure measurement package. These temperature/pressure recorders were fastened to weights at the bottom of thermistor strings (see Figure 2.16) so that the elevation of the instruments would not change appreciably. During the 2002 experiment,

pressure was recorded underwater at site SP5 at a depth of $2.5m$ with an SBE39 temperature/pressure recorder. An SBE39 temperature/pressure recorder was also deployed at a $6m$ depth in LO during the 2002 experiment, but this instrument became detached from the deployment apparatus and traveled several kilometers, so the data is useless – pressure sensors proved extremely difficult to deploy in LO because of high frequency surface waves and we settled for pressures measured inside SP. During the 2003 experiment, pressure was recorded $3.0m$ below the surface at site DR with an SBE39 temperature/pressure recorder and $3.9m$ below the surface at site SC with the In Situ miniTROLL (see Figures 2.4 and 2.5).

The SBE39 pressure sensors used in these experiments have a range of $0 - 303kPa$, an initial accuracy of $\pm 0.3kPa$, and a standard drift of $\pm 0.012kPa$ per month. Note that $0.012kPa$ corresponds to about $1mm$ of water, so these instruments are highly accurate. The miniTROLL pressure sensor has a range of $0 - 207kPa$ and an accuracy of $\pm 0.21kPa$, corresponding to about $\pm 2cm$ of water, so this instrument is less accurate than the SBE39's but still able to resolve the $10cm$ water surface elevation changes that occur over the course of a typical day in the LO environment.

Because we did not accurately measure the absolute vertical elevation of our pressure sensors, we do not know absolute water surface elevations, but at any given location where we measured pressure, we do know how water surface elevation changes in time. This is true inasmuch as the pressure sensors did not change elevation during the deployments. In order to roughly estimate absolute water surface elevations, we turn to NOAA CO-OPS. This program maintains continuous $6min$ water surface elevation records from a buoy in Oswego Harbor (OH), $30mi$ east of SP, and the records are publicly available. We compare this data to our

measured water surface elevations to estimate absolute water surface elevations and thus water depth in SP – note that bathymetric data is referenced to lake levels measured at OH. We also use filtered OH water surface elevations to fill in some missing data (see section 3.2).

2.9 Notation for Uncertainty Analysis

A large portion of this thesis is devoted to uncertainty analysis. Because our goal is to integrate measured variables in time to arrive at residence time statistics, it is very important for us to consider how errors are correlated in time[6]. Because we have a large number of variables, we use a concise notation to distinguish uncertainty intervals due to bias errors, precision errors, and errors that are correlated over a finite but nonzero time scale.

First let us discuss our notation for errors and uncertainty intervals. For an arbitrary quantity ξ, let us define the *error*, $\Delta\xi$, to be the difference between the measured or calculated value ξ and its true value. Let us then define $\delta\xi$ to be the 95% uncertainty interval for ξ. That is, we expect $\Delta\xi$ to fall within $\pm\delta\xi$ with 95% confidence. Note that the expected value of $\Delta\xi$ is always zero if we as experimentalists have made our best estimate of the true value of ξ.

Now let us discuss the various ways in which errors may be correlated in time t. The autocorrelation function, $\rho_{\Delta\xi}(\tau)$, for error $\Delta\xi$ is defined in Eq. 2.1 where $E\{\ \}$ is the expected value operator and σ_ξ is the standard deviation of the error $\Delta\xi$.

$$\rho_{\Delta\xi}(\tau) \equiv \frac{E\left\{\Delta\xi(t)\Delta\xi(t+\tau)\right\}}{\sigma_\xi^2} \tag{2.1}$$

[6]Propagation of errors through time integration is discussed in Appendix A.

Following standard terminology – e.g. Kline and McClintock (1953) – a *bias error* is an error for which $\rho_{\Delta\xi}(\tau) = 1$ for all values of τ. On the other extreme, a *precision error* is an error for which $\rho_{\Delta\xi}(\tau) = 1$ for $\tau = 0$, but $\rho_{\Delta\xi}(\tau) = 0$ for all other values of τ. In the majority of scientific experiments, all errors may be classified as either bias or precision errors, but because our measurements are taken in a turbulent fluid, there are a wide range of time scales involved, and we may encounter errors that are somewhere in between bias and precision errors. These errors are correlated over some finite but nonzero time window. To distinguish uncertainty intervals due to bias errors, precision errors, and errors that are correlated over a various finite but nonzero time windows, let us denote these uncertainties using the notation given in Table 2.7. We define τ_Q to be the autocorrelation time scale of outflow and τ_C to be a time scale associated with concentration measurements – both time scales are discussed later on in this thesis.

Table 2.7: Notation for uncertainty stemming from different types of error.

Symbol	Error Source
$\bar{\delta}\xi$	Bias error (correlated indefinitely in time)
$\tilde{\delta}\xi$	Precision error (uncorrelated in time)
$\breve{\delta}\xi$	Error correlated over time τ_Q
$\hat{\delta}\xi$	Error correlated over time τ_C

Chapter 3

Analysis

In this chapter, we discuss our analysis of raw field data by which we reach the results presented in Chapter 4. Significant data processing was required to arrive at estimates of water surface elevation, outflow, concentration, residence time distributions, cumulative residence time distributions, and mean residence times – each of these quantities receives attention here. Uncertainties in outflow, concentration, and residence time are considered in depth, and measures for reducing uncertainty in similar experiments are discussed. Temperatures and meteorological data were ready to use after downloading from the field equipment, so these quantities are not discussed in this chapter.

3.1 Bathymetry

The raw bathymetry data plotted in Figure 2.13 was processed with an eye towards future use in a 3D numerical model. The shoreline of Lake Ontario was mapped by lining up the grid in Figure 2.13 with the USGS topographic map shown in Figure 2.3. All of the bathymetric data was interpolated onto a $17.5m \times 17.5m$ grid using the linear interpolation algorithm in MATLAB 6.5. The stream depth was made uniform and equal to the mean stream depth, and all of the data was smoothed using a $52.5m \times 52.5m$ moving average filter. The resulting bathymetry is plotted in Figure 2.1.

3.2 Water Surface Elevation

Water surface elevations, η, in SP and SC were computed from barometric pressure, P_a, measured at the LSB weather station and underwater pressure, P, measured by pressure sensors as described in Section 2.8.4 using Eq. 3.1, where $g = 9.806 m/s^2$ is the acceleration of gravity, T is the temperature recorded by the pressure sensor, and $\rho(P_a, T)$ is computed from the 1981 UNESCO standard formula given in Gill (1982).

$$\eta = \frac{P - P_a}{g\rho(P_a, T)} \tag{3.1}$$

Note that η is the depth of water above a pressure sensor. Because we only very roughly know where the pressure sensors were located, vertically, we compare η to water surface elevations measured by NOAA in Oswego Harbor (OH), $30 mi$ east of SP, in order to estimate absolute water surface elevation, H. In Figures 3.1 and 3.2 we compare water surface elevations, η, calculated from measured data using Eq. 3.1 with water surface elevations, H, measured at OH during the 2002 and 2003 dye experiments, respectively.

Before going on with the analysis, let us observe the relationship between water surface elevations in LO, SP, and SC. In Figures 3.1 and 3.2, we see that SP is strongly coupled to LO – the water surface elevation in SP appears to be set primarily by the level in LO. During the 2003 experiment, this is not surprising, as stream flow from SC was low. During the 2002 experiment, water surface elevations in SP were measured during a period of high and relatively constant flow from SC – thus water levels in SP are probably higher than those in LO during this experiment, and if we had measured water surface elevations until

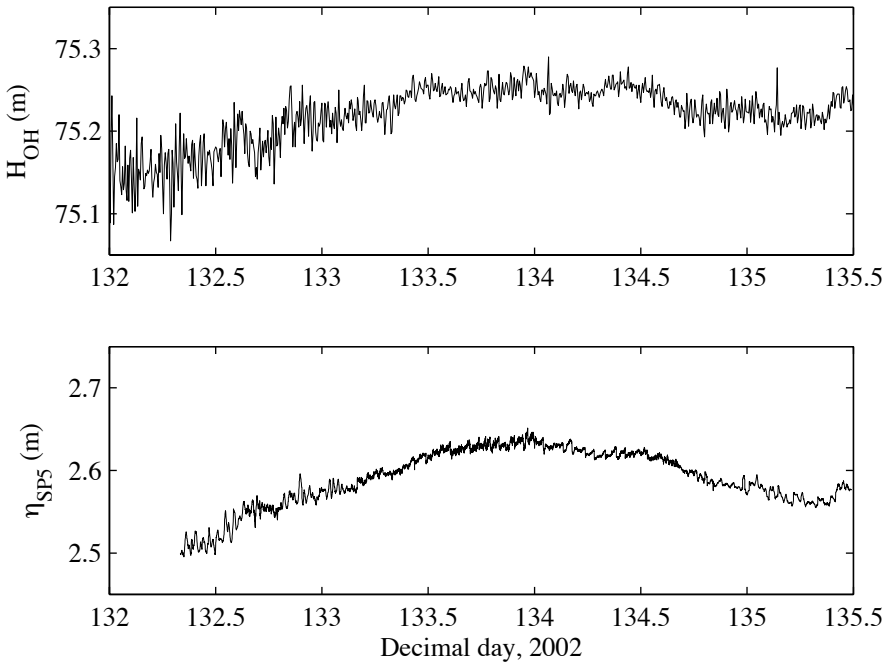

Figure 3.1: Water surface elevation in Oswego Harbor, H_{OH}, obtained from NOAA CO-OPS, and water surface elevation measured at site SP5, η_{SP5}, during the 2002 experiment. Note that H_{OH} is referenced to the IGLD85 datum whereas η_{SP5} is referenced to the unknown vertical elevation of the pressure sensor at SP5.

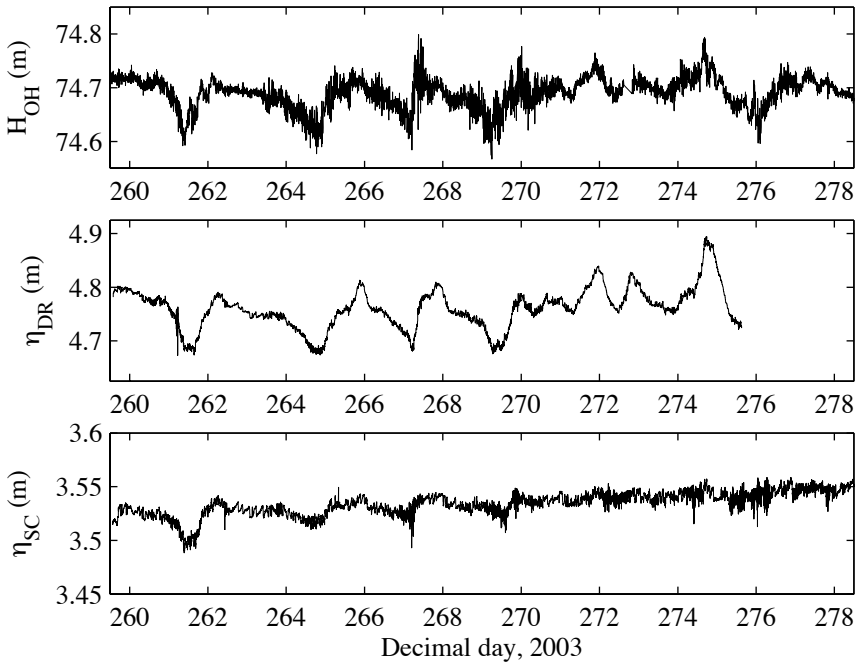

Figure 3.2: Water surface elevation in Oswego Harbor, H_{OH}, obtained from NOAA CO-OPS, water surface elevation measured at site DR, η_{DR}, and water surface elevation measured at site SC, η_{SC}, during the 2003 experiment. Note that H_{OH} is referenced to the IGLD85 datum whereas η_{DR} and η_{SC} are referenced to the unknown vertical elevations of the respective pressure sensors.

after SP had drained, we would probably have seen the level in SP drop where the LO elevations do not. We also observe that during the 2003 experiment, water levels in SC appear to be somewhat influenced by LO, but the amplitude of the response is damped considerably (note different ranges of the axes in Figure 3.2).

We also observe that high frequency oscillations are present in OH which are not present in SP, and furthermore, these oscillations are high in energy (note that OH is considerably larger than SP). We found that applying an $8th$ order $1.5hr$ low-pass Butterworth filter to the water surface elevation records from OH[1] removed these high frequency oscillations. We applied this filter to water surface elevations in SP and OH. We referenced the water surface elevations in SP to the IGLD85 datum by matching mean filtered water surface elevations in SP and OH over the time window during which SP data is available. Filtered water surface elevation records measured in SP and referenced to IGLD85 are compared to filtered records from OH for the 2002 and 2003 experiments in Figures 3.3 and 3.4. The SP records are taken from sites SP5 and DR for the 2002 and 2003 experiments, respectively. Note that for the 2002 experiment, we expect this method of matching mean water surface elevations in SP and LO to bias absolute water surface elevations by several centimeters during the period of high flow. Also note that we do not compare the record from the stream site, SC, measured in 2003.

Missing data was filled in by splicing together the SP and OH water surface elevation measurements. The water surface elevations presented in Chapter 4 are spliced, filtered, and referenced to IGLD85 as described above.

[1]The filter was applied twice – in the forward direction and then in the reverse direction.

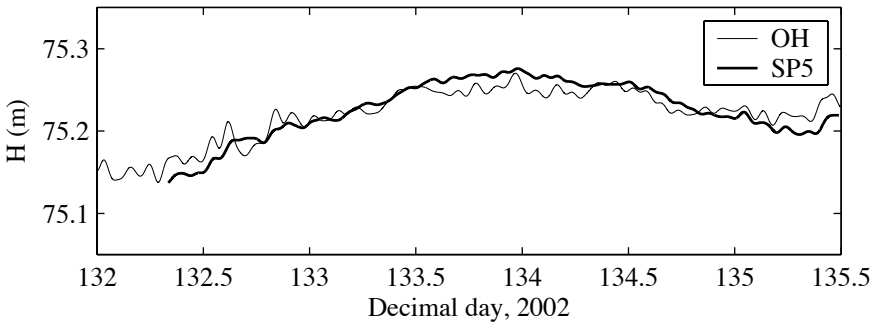

Figure 3.3: Comparison of filtered water surface elevation records from SP5 and OH during the 2002 experiment. Note that the SP5 record has been referenced to the IGLD85 datum by matching the means of the SP5 and OH records.

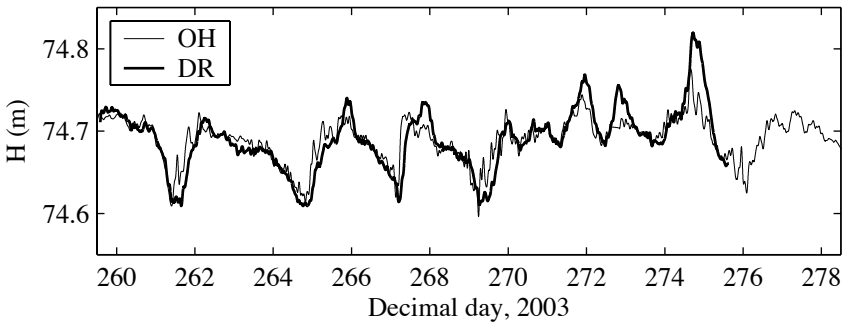

Figure 3.4: Comparison of filtered water surface elevation records from DR and OH during the 2003 experiment. Note that the DR record has been referenced to the IGLD85 datum by matching the means of the DR and OH records.

3.3 Vertical Velocity Profiles

Our goal in this section is to arrive at a vertical profile of the velocity component pointing from SP to LO on the channel centerline underneath the footbridge. We begin with the instantaneous raw velocity vector profile $\vec{u}(z,t)$ measured by the $1200kHz$ ADCP, and end with a profile of the ensemble-averaged long-stream velocity component $U(z,t)$.

3.3.1 Error Velocity Filter

In earth coordinate mode, the ADCP reports an error velocity, which is the difference between vertical velocities computed by two independent linear combinations of the four measured beam velocities. The error velocity is a good test of the horizontal homogeneity of the beam velocities, and because the beam velocities are more homogeneous over longer time scales, a tight filter on the error velocity was not imposed until after ensemble averaging. However, data with unusually large error velocity was throw out in the first stage of data processing. The histograms of error velocity were inspected and the error velocity cutoff at this first stage was chosen to make the histograms Gaussian and symmetrical.

2003

The 2003 error velocity histograms are plotted in Figure 3.5. On the first day of the dye experiment (decimal day 259 of 2003), the histogram was highly asymmetrical and, interestingly, periodic. For day 259, data with error velocities over $11.4cm/s$ in magnitude were thrown out. For the rest of the experiment, after we changed the ADCP configuration so that the data was less noisy (see Section 2.5.2), the histograms looked more Gaussian, except for some obvious outliers; the histogram

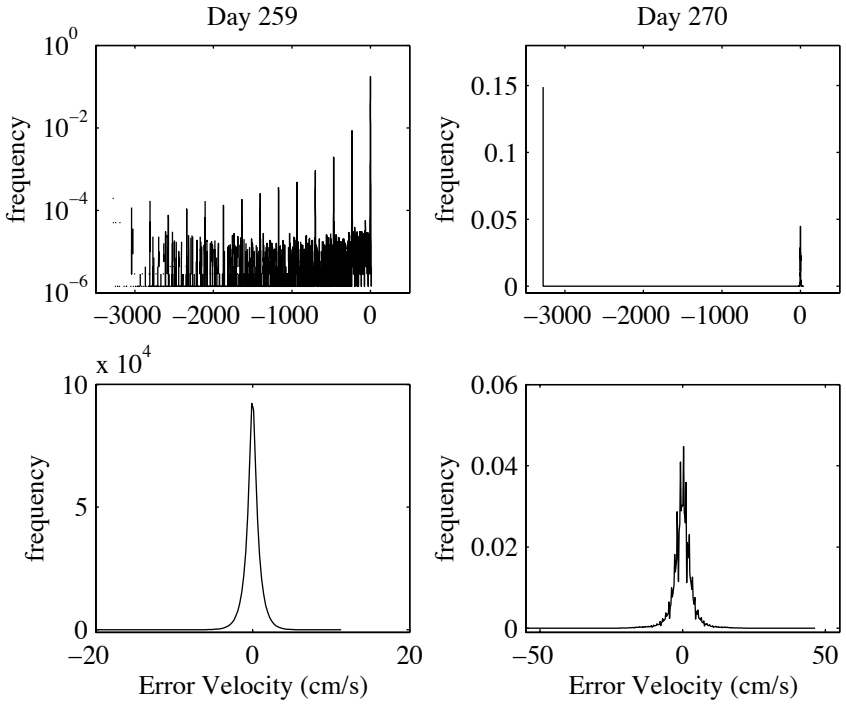

Figure 3.5: Representative error velocity histograms for the 2003 dye experiment. The day 259 histogram is plotted on the left, and the day 270 histogram, representative of all days other than 259, is plotted on the right. Below is a closeup of the portion of each histogram within the error velocity filter bounds.

for day 270 is representative, and the error velocity cutoff was set at $46.5cm/s$.

2002

The 2002 error velocity histogram is plotted in Figure 3.6. To make the histogram Gaussian and symmetrical, we threw out all data having error velocity magnitude greater than $36.3cm/s$.

3.3.2 Ensemble Averaging

The ideal ensemble length is much longer than the longest turbulent timescale and much shorter than the shortest barotropic mode. In order to chose an ensemble averaging period, we inspect the power spectra of velocity to identify the

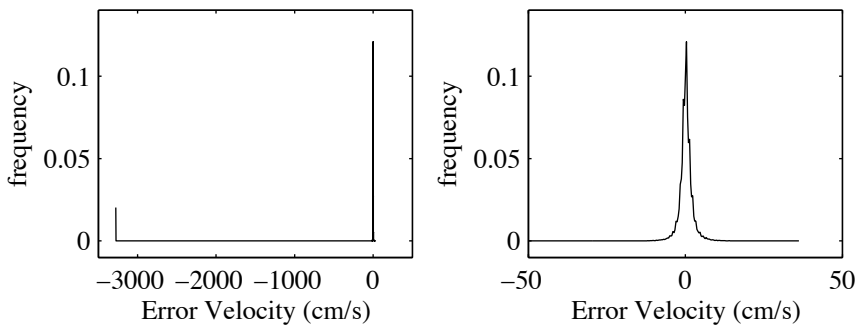

Figure 3.6: Error velocity histogram for the 2002 dye experiment. All data below the water surface is included. The plot on the right is simply a closer view of a portion of the histogram.

relevant time scales. Because we work with velocities in earth coordinates, the reader should exercise caution when interpreting power spectra that involve higher frequencies. As noted in Lu and Lueck (1999a,b), instantaneous measurements in earth coordinates cannot be interpreted as physical velocities because they are in fact linear combinations of two or more physical velocities measured along ADCP beams, and the beams are separated in space by a distance that increases with depth. Time averages of velocities in earth coordinates may be homogeneous in horizontal planes, but because of turbulence having scales smaller than the beam spacing, the instantaneous velocities themselves are certainly not homogeneous, so information in high frequency velocity fluctuations is lost in the linear transformation to beam coordinates. For an example of turbulence measurements with an ADCP and a discussion of issues involved in measuring turbulence with divergent acoustic beams, see Stacey et. al. (1999).

2003

The power spectral density of long-channel velocity, S_{uu}, for the 2003 experiment is plotted in Figure 3.7. Because we did not deal with velocities in beam coordinates,

we cannot trust the spectra in the higher frequencies. Nonetheless, the dominant barotropic modes of Lake Ontario and other unidentified modes are clearly represented by a large hump in S_{uu} for periods between $6min$ and $1.5hrs$. From Hamblin (1982), we expect to see the first four modes of barotropic oscillations in LO, having periods of $5.0hrs$, $3.2hrs$, $2.3hrs$, and $1.7hrs$. The first mode of the barotropic seiche in SP should be around $3min$. We do not know the source of the spike at $24min$, but hypothesize that this is some sort of resonance mode between SP and the nearby bays. This mode is readily observed by eye in the field – flow reversals occur visibly in the channel every 10 to 15 minutes. The beginning of the inertial subrange is visible, but the higher turbulent frequencies break down into noise because beam velocities are not correlated over these short time scales, and channel coordinate velocities are linear combinations of these uncorrelated physical velocities.

From dimensional analysis, we expect the turbulent time scale to be order $\kappa z/u_*$, where u_* is the friction velocity of the bottom boundary layer, computed later, z is the height above the bed, and $\kappa = 0.41$ is the Kármán constant. Friction velocities were assumed to be around 1/10 of the mid-depth velocity which oscillated during the 2003 experiment with amplitude between 4 and $40cm/s$. The maximum depth of the channel is $3m$. The time scale of the largest eddies thus varies with mid-depth velocity as shown in Figure 3.8, so we see that the longest time scale of the turbulence is around $8min$ when the mean velocity is $2.5cm/s$ (lower than typical amplitudes). For higher velocities, the turbulent time scale is shorter, but unfortunately it is still near the same order of magnitude as the upper bound on the ensemble-averaging period. The turbulent time scale drops below 10% of $8min$ for velocities over $10cm/s$. The standard practice is to look

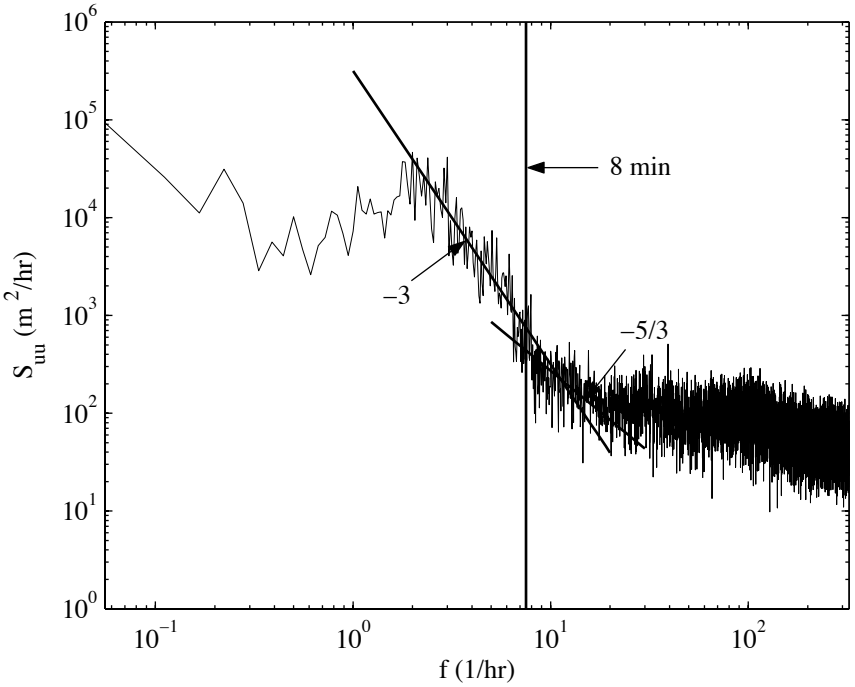

Figure 3.7: Power spectral density of instantaneously measured long-stream velocity from $1.5m$ above the bottom of the channel (mid-depth) during the 2003 dye experiment. Power spectral densities were computed for nine ensembles, each $18hrs$ in length, and averaged to obtain the result shown. The vertical line shows the $8min$ period corresponding to the $4min$ ensemble averages.

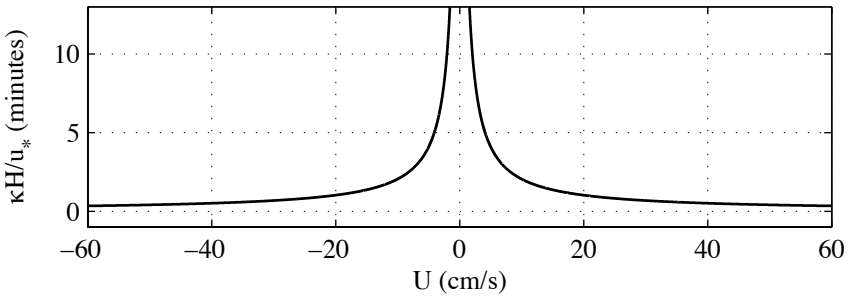

Figure 3.8: Time scale of the largest eddies in the channel, computed from a simple scaling argument for a range of velocities found in the channel at mid-depth. The friction velocity is taken to be 1/10 of the mid-depth velocity.

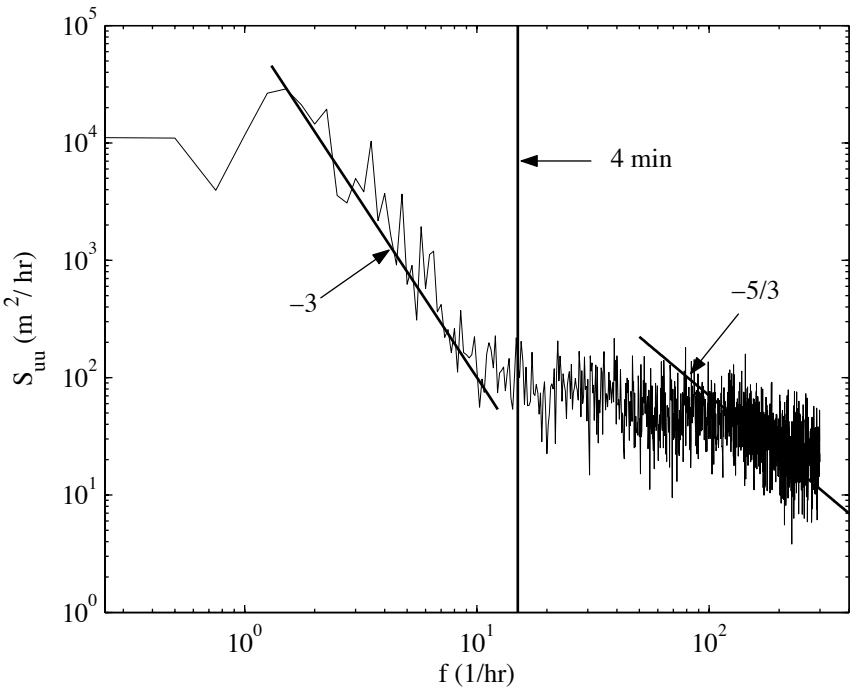

Figure 3.9: Power spectral density of instantaneously measured long-stream velocity from the free stream during the 2002 dye experiment. Power spectral densities were computed for three ensembles, each $4hrs$ in length, and averaged to obtain the result shown. The vertical line shows the $4min$ period corresponding to the $2min$ ensemble averages.

for a spectral gap between the turbulence and the large scale modes (Lohrman, et. al. 1990) and chose the ensemble averaging period at the longer end of that gap. Our spectral gap is very small, if it exists at all, but at a time scale of $8min$ the 3D turbulence appears to meet the lower mode oscillations, so we chose a $4min$ ensemble length and note that we may expect modest errors in our time-averaged quantities due to smoothing over of weak barotropic modes (for example the SP seiche) and due to turbulence.

Ensemble averaging was carried out over $4min$ intervals and $5cm$ vertical bins using a bootstrap sampling technique. Each time-space ensemble window was randomly sampled with replacement 1000 times, and for each set of samples, the mean was computed. The expected value and 95% confidence interval of the mean was taken from the resulting distribution – this technique is known as bootstrapping (Efron and Tibshirani 1993). Note that missing data was simply left out of the ensemble average, but the percentage of data that was missing was noted, and ensembles for which more than 90% of the data was missing were thrown out. All components of velocity, including the error velocity, were ensemble averaged. The error velocity magnitude was greatly reduced by ensemble averaging, confirming the hypothesis that over long time scales, the mean velocity field is homogeneous in horizontal planes. It is interesting to note that uncertainty in the mean velocity measured by the bootstrap technique often exceeds the error velocity measured by the ADCP (see Figure 3.13). This relatively high uncertainty in the mean is probably due the fact that the $4min$ averaging window is not comfortably inside a spectral gap between barotropic modes and turbulence.

2002

The power spectral densities of long-channel, cross-channel, and vertical velocities for the 2002 experiment are plotted in Figure 3.9. Velocities in the channel during this experiment were very high, having magnitudes between 30 and 75cm/s. Referring to Figure 3.8, we see that we expect the turbulence time scales to be much shorter in this case. The power spectral density function seems to support this – we actually do see a spectral gap, centered around a 2min period. We tried using a 1min ensemble average corresponding to this 2min period but found that a 2min ensemble average produces velocity profiles that are less noisy without adding significant error. Thus, we ensemble averaged our data over 2min windows. We carried out the ensemble average in the same manner as for 2003, using a bootstrap to estimate error due to the quasi-steady assumption.

3.3.3 Finding the Free Surface

2003

To reference the bin elevations to the bed, 30cm was added to account for the ADCP and its frame. To find the location of the free surface, the water surface elevation record (Section 3.2) was compared by eye to ADCP backscatter intensity as shown in Figure 3.10. The peak backscatter intensity occurs at the free surface, so by matching these plots by eye and manually testing different bed elevations to line up the plots, the bottom elevation was determined to be 71.74m above the IGLD85 datum. This bottom elevation was subtracted from water surface elevation, giving a time series of water depth above the bed. Data above the free surface was thrown out.

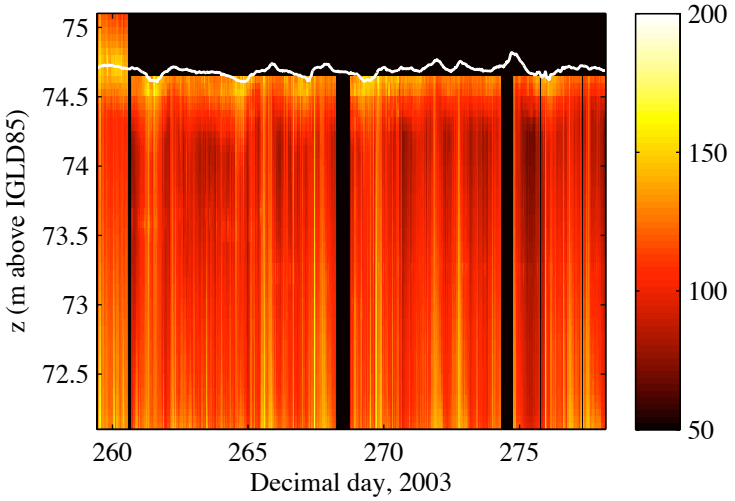

Figure 3.10: The elevation of the bed underneath the ADCP was found by matching ADCP backscatter intensity to the water surface elevation record (white line) as shown here. The elevation of the ADCP bins have been adjusted so that water surface elevation matches peak backscatter intensity, and the magnitude of the required adjustment gives the elevation of the bed below the ADCP.

2002

For the 2002 experiment, we used the same method as for 2003, comparing backscatter intensity to water surface elevation. The bed elevation below the ADCP was found to be $72.42m$ above the IGLD85 datum. A plot of the match between water surface elevation and backscatter intensity is shown in Figure 3.11.

3.3.4 Transforming from Earth to Channel Coordinates

We use the mean direction of the velocity in the channel to determine the channel direction underneath the footbridge.

2003

The angle of the channel was computed using the ensemble averaged 2003 velocities in the middle 1/6 of the channel ($1.25m$ to $1.75m$ above the bed). The record

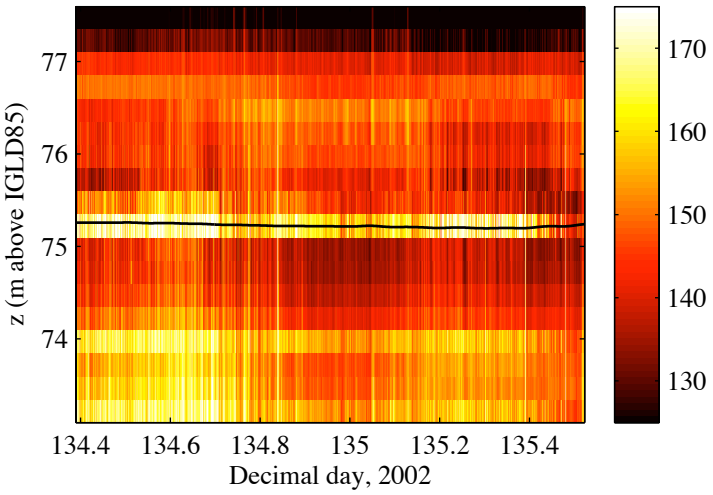

Figure 3.11: Matching of ADCP backscatter intensity and water surface elevation (black line) to find the bed elevation for the 2002 dye experiment.

was filtered to select data for which the error velocity was less than $0.3cm/s$ in magnitude and the northward velocity was greater than $6cm/s$ in magnitude. The idea was to judge the angle using data for which the flow was strong and horizontally homogeneous (error velocity less than 5% of mean velocity). The direction of these velocity vectors (^{o} north of east and ^{o} vertical from the horizontal plane) was then computed, and the mean angles were taken to describe the direction of the channel. Different angles were computed for velocities from SP to LO and for velocities from LO to SP.

The range of angles found at the selected velocities and the mean angles taken to represent the direction of the channel are plotted in Figure 3.12. We note that the angles measured by this method compare well to angles measured from USGS maps and aerial photos of SP.

After ensemble averaging, velocities were converted from earth coordinates, which we denote by U_{north}, U_{east}, U_{up}, and U_{error}, to channel coordinates (long-stream, cross-stream, bed-normal, and error velocity), which we denote by U, V,

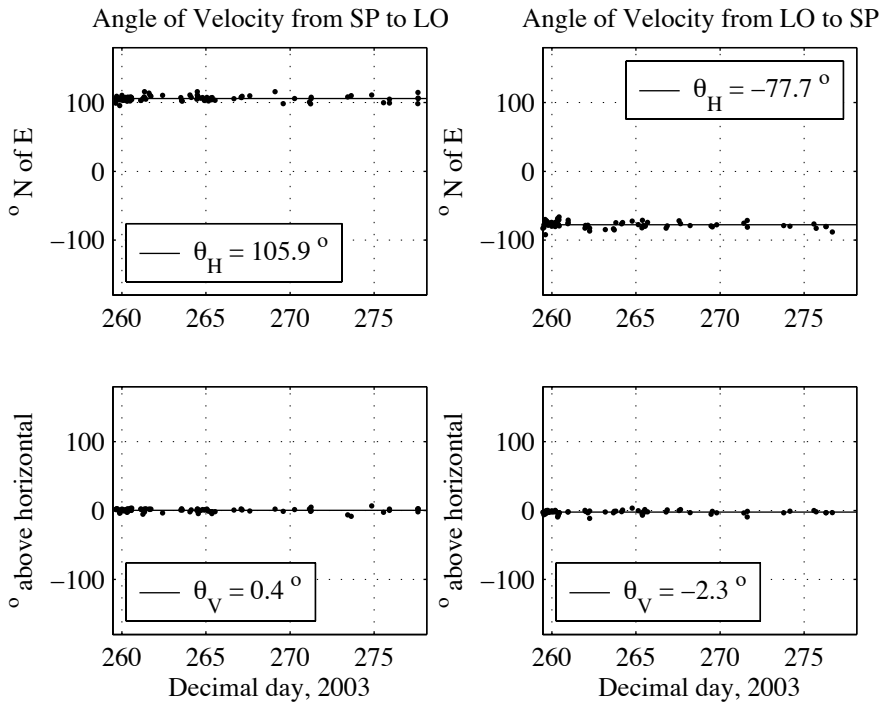

Figure 3.12: Angle of velocity vector in the channel during 2003 experiment. Angles were computed from velocities for which the error velocity magnitude is less than $0.3cm/s$ and the northward velocity magnitude is greater than $6cm/s$. The horizontal lines and the legends show the angles that are taken to represent the direction of the channel and used to transform velocity to channel coordinates.

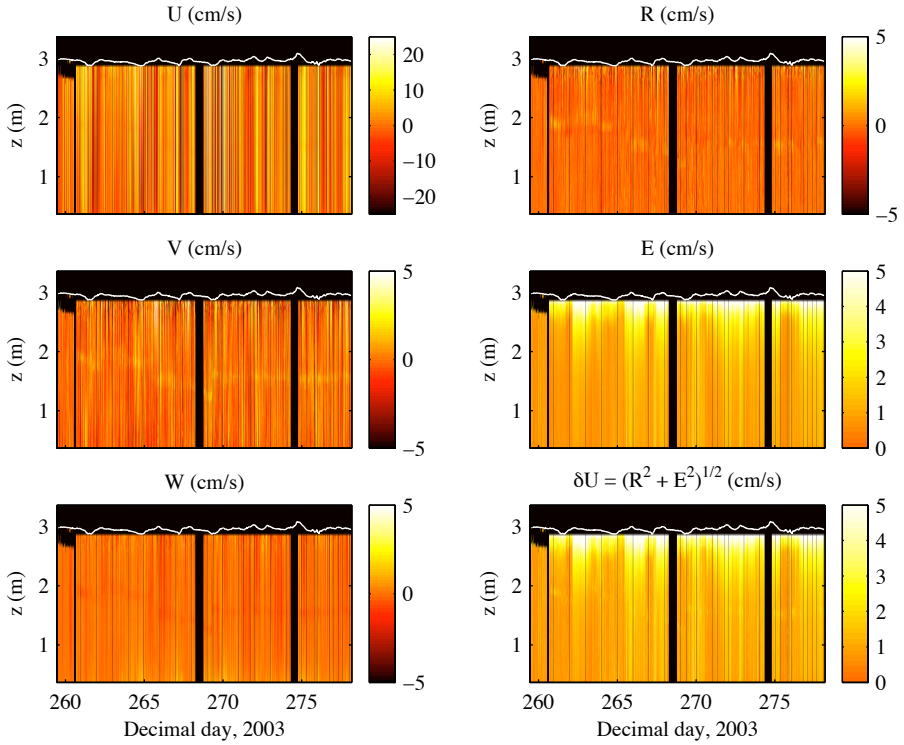

Figure 3.13: All 2003 velocity data below the free surface after the ensemble average, coordinate transformation, and error filtering. Long-stream, cross-stream, and vertical velocities are plotted on the left. Error velocity, ensemble average bootstrap error, and the estimated total 95% uncertainty are plotted on the right.

W, and R, by Eq. 3.2. The velocities are plotted in channel coordinates in Figure 3.13.

$$\begin{aligned} U &= (U_{north}\sin\theta_H + U_{east}\cos\theta_H)\cos\theta_V + U_{up}\sin\theta_V \\ V &= U_{north}\cos\theta_H - U_{east}\sin\theta_H \\ W &= -(U_{north}\sin\theta_H + U_{east}\cos\theta_H)\sin\theta_V + U_{up}\cos\theta_V \\ R &= U_{error} \end{aligned} \tag{3.2}$$

2002

For the 2002 experiment, we repeated the procedure described for 2003, taking velocity data between $1.3m$ and $1.6m$ above the bed. Since flow was almost always from SP to LO, we did not consider the case of flow from LO to SP. The velocity vector angles are shown in Figure 3.14, and we see that they are practically identical to those found in 2003. The 2002 velocities were converted to channel coordinates using Eq. 3.2, and the velocities are plotted in channel coordinates in Figure 3.15.

3.3.5 Velocity Uncertainty

2003

The velocity uncertainty estimates were converted to channel coordinates by the same formulas used to convert velocities (Eq. 3.2). The root sum square of the error velocity, R, and the 95% uncertainty in the ensemble average long-stream velocity, E, was taken as an estimate of the total 95% uncertainty in the long-stream velocity measurements, $\delta U = \sqrt{R^2 + E^2}$. Ensembles with $\delta U > 5cm/s$ were thrown away, as were ensembles for which more than 10% of the original

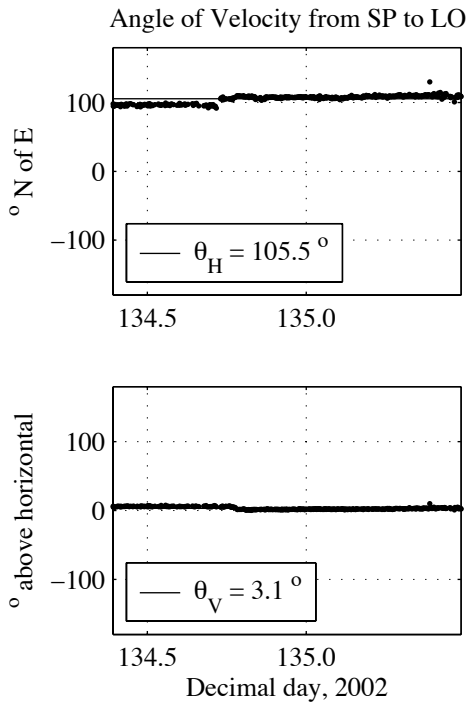

Figure 3.14: Angle of velocity vector in the channel during 2002 experiment. Angles were computed from velocities for which the error velocity magnitude is less than $0.3cm/s$ and the northward velocity magnitude is greater than $6cm/s$. The horizontal lines and the legends show the angles that are taken to represent the direction of the channel and used to transform velocity to channel coordinates.

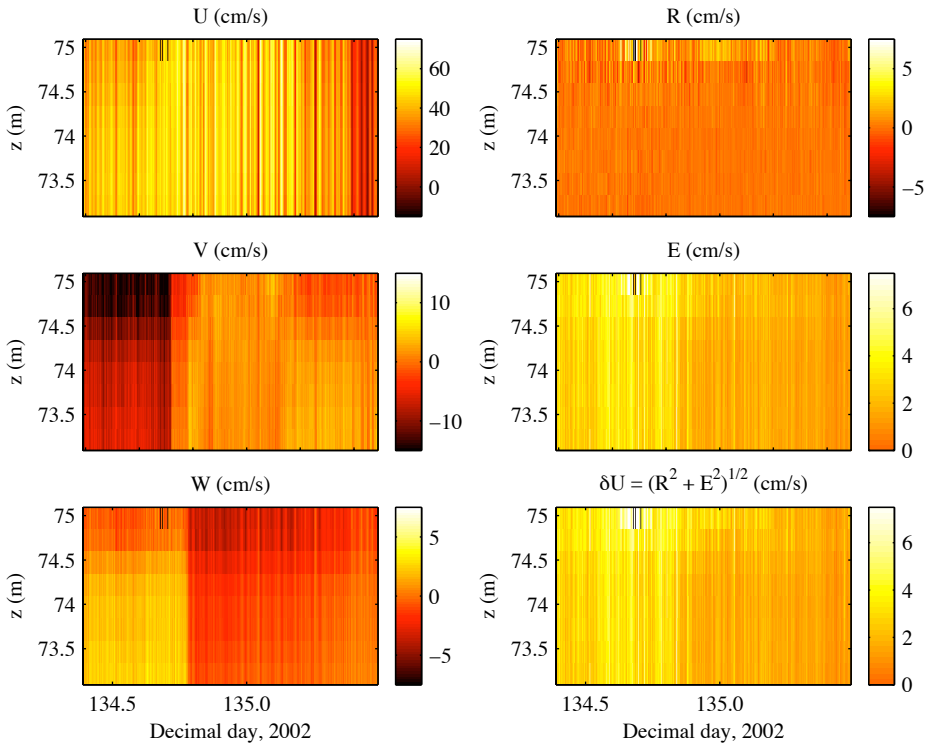

Figure 3.15: Components of the 2002 velocities in channel coordinates are plotted on the left. The error velocity, ensemble averaging uncertainty, and total uncertainty are plotted on the right.

data is missing. In the future, we will have to propagate uncertainty through time integration, so we should take a moment to consider how δU is correlated in time. Because ensemble averaging error is really error in the assumption of quasi-steady flow, we expect it to be correlated over a time scale close to the autocorrelation timescale of outflow, τ_Q, and thus we denote $\delta U = \breve{\delta} U$ (see Section 2.9). The sources of long-stream velocity uncertainty and the total uncertainty are plotted in Figure 3.13 along with the velocity components.

2002

In 2002, as in 2003, we have uncertainty due to error velocities and ensemble averaging error that is correlated over the autocorrelation time scale of the outflow, $\breve{\delta} U = \sqrt{R^2 + E^2}$. For this experiment, we reject ensembles for which more than 50% of the original data is missing or for which $\breve{\delta} U > 3 cm/s$. The various contributions to the uncertainty are plotted in Figure 3.15 along with the velocity components and the magnitude of the velocity vector. The total uncertainty is not that bad – 90% of the uncertainty is less than 10% of the long-channel velocity.

3.3.6 Characterizing the Bottom Boundary Layer

The 2003 vertical velocity profile data set is far better in resolution than the 2002 data set. In particular, in the 2003 data set, the first bin is centered only $37cm$ above the bed, whereas during the 2002 experiment it was $80cm$ above the bed. Because the first bin is near the bed, we are able to extrapolate the 2003 data set even closer to the bed using a good fit to the accelerating boundary layer profile (Section 3.3.7). We do not have enough points to do this for the 2002 data set. Thus, we use the extrapolated 2003 data to develop a method for extrapolating

the 2002 data to the bed.

We will see in Section 3.3.7 that we are unable to find a good predictive relationship between free stream velocities, accelerations, and the accelerating bottom boundary layer. However, we may make rough predictions if we assume a log law (Eq. 3.3), assume that the friction velocity, u_*, is directly proportional to the free stream velocity, $U(z_1)$, at a particular height, z_1, and fit all of the 2003 data to find the coefficient of proportionality and the roughness height, z_0. Assuming that friction velocity is proportional to free stream velocity at a particular elevation is common practice, and because friction velocity represents the shear stress at the bed, this relationship is often expressed in terms of the drag coefficient, C_d. Specifically, we assume the relationship given by Eq. 3.4. Plugging 3.4 into 3.3, and requiring continuity of velocity at z_1, we obtain Eq. 3.5.

$$U(z) = \frac{u_*}{\kappa} \ln\left(\frac{z}{z_0}\right) \tag{3.3}$$

$$u_* = C_d^{1/2} U(z_1) \tag{3.4}$$

$$U(z) = C_d^{1/2} \frac{U(z_1)}{\kappa} \ln\left(\frac{z}{z_1}\right) + U(z_1) \tag{3.5}$$

$$\breve{\delta} U(z) = \frac{U(z_1)}{\kappa} \ln\left(\frac{z}{z_1}\right) \breve{\delta} C_d^{1/2} \tag{3.6}$$

In 2002, the lowest bin was $0.80m$ above the bed, so we fit the extrapolated 2003 data to Eq. 3.5 for $z_1 = 0.80m$. We perform the fit by rearranging Eq. 3.5 to compute $C_d^{1/2}$ for each data point in the boundary layer, taking the median value to be the best fit. Then, we compute the error, $\Delta C_d^{1/2}$, directly for each point, and

find the 95% confidence interval, $\delta C_d^{1/2}(z)$, as a function of bin elevation. $\delta C_d^{1/2}(z)$ is nearly linear, so we fit a line to it, and we will use the fitted line to estimate uncertainty due to extrapolating the boundary layer later on – the extrapolation uncertainty in $U(z)$ stemming from uncertainty $\delta C_d^{1/2}(z)$ is given in Eq. 3.6. We find that $C_d^{1/2}$ and $\delta C_d^{1/2}(z)$ vary with the magnitude of the free stream velocity but become invariant for free stream velocity magnitudes over $10cm/s$. Thus, we filter the 2003 boundary layer data, selecting time steps at which free stream velocity magnitude exceeds $15cm/s$ (782 time steps), and use only this data to compute $C_d^{1/2}$ and $\delta C_d^{1/2}(z)$. Because deviation from the log law is probably due to acceleration and deceleration of the flow, we assume that $\delta C_d^{1/2}(z)$ is correlated over the time scale of the flow itself, and thus we denote $\delta C_d^{1/2}(z) = \breve{\delta} C_d^{1/2}(z)$.

The results of fitting Eq. 3.5 to this filtered 2003 boundary layer data for $z_1 = 0.80m$ are $C_d^{1/2} = 0.14$ and $\breve{\delta} C_d^{1/2}(z) = (0.22m^{-1})z + 0.024$. In Figure 3.16, we plot the directly computed 95% uncertainty $\breve{\delta} C_d^{1/2}(z)$ along with the linear fit. An example of a boundary layer extrapolated using Eq. 3.5 is plotted in Figure 3.17.

3.3.7 Vertical Extrapolation

2003

The ADCP velocity profile covered most of the vertical extent of the channel in 2003, but because the ADCP rested on the bottom of the channel and has a finite blanking distance between the transducers and the first bin, velocity data was not measured very near to the bed. Because of acoustic reflections from the surface, measurements very near to the surface are noisy and in error. Also, because of unanticipated water levels and a desire to have small bins, we mistakenly did not

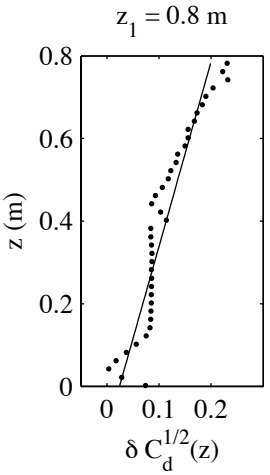

Figure 3.16: $\breve{\delta}C_d^{1/2}(z)$ computed directly from extrapolated 2003 velocity data and linear fit.

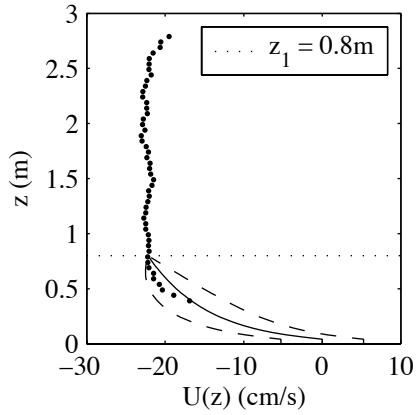

Figure 3.17: Log law extrapolation of the boundary layer profile for a sample 2003 profile using free stream velocity at $z_1 = 0.80m$. Measured 2003 data is represented by dots, the extrapolated profile is a solid line, and the 95% confidence interval is bounded by dashed lines.

configure the ADCP bins to always reach the free surface. For these reasons, the velocity profile had to be extrapolated a short distance to the bottom and to the surface. Furthermore, it was desired to find a general parameterization for the velocity profile in the SP channel which might be used to predict the profile from a small number of velocity measurements. Unfortunately, such a parameterization does not seem to exist, but our efforts to find one are documented here.

The first step in the extrapolation process was to determine the roughness height, z_0, to be used in all of the following analysis. To find z_0, we fit a log law to the bottom four points (between $39cm$ and $54cm$ above the bed) at each time using the linear least squares method. The log law is given by Eq. 3.3. Statistics from these fits were analyzed to determine an appropriate roughness length scale, z_0. A histogram of z_0 is shown in Figure 3.18. The median value, $z_0 = 13cm$, was taken as the fixed roughness length for the purpose of extrapolation to the bottom throughout the experiment. Because the channel has a sand bottom, we do expect z_0 to change somewhat throughout the experiment, but uncertainty in z_0 due to its sensitivity to uncertainty in the data during the following fits is probably much greater than the actual change in z_0, so we decided to use a fixed z_0. We also note that for a fixed z_0 all of the curve fits described in the remainder of this section are linear least squares problems. If z_0 is an unknown, the following fits become nonlinear problems. We note that a better method may be to use a physically-based estimate of z_0, as the shape of the boundary layer is sensitive to the value of z_0 (Lorke, et. al. 2002).

Because the time scales of barotropic unsteadiness in the SP channel are not always longer than the turbulent time scales, the quasi-steady assumption behind the log law does not generally hold, and attempts to fit a log law to the entire veloc-

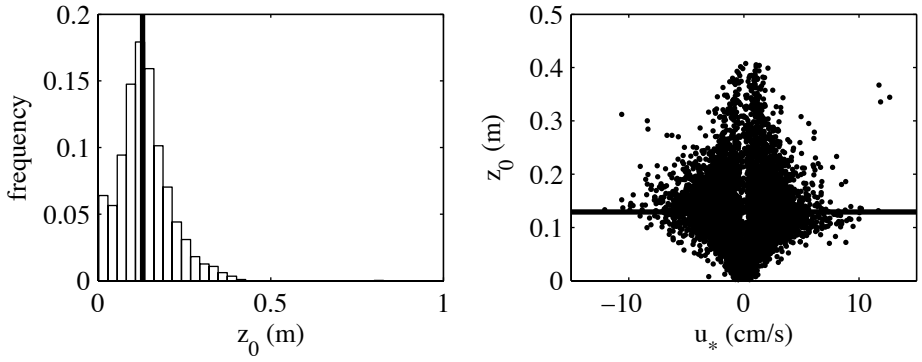

Figure 3.18: Fitting a log law to the bottom four points of the 2003 velocity profile data set resulted in the histogram of roughness height, z_0 shown on the left – the median value of z_0 is plotted as a vertical line. Roughness height is related to friction velocity, u_*, as shown on the right.

ity profile were disastrous. A log-wake law, recommended by Nezu and Nakagawa (1993) and originally from empirical work by Coles (1956), fit a small number of profiles very nicely, but was generally unsatisfactory. The failure of these profiles is not surprising, because they assume a statistically steady state, and the SP channel is far from steady, as discussed in Section 3.3.2.

The profile we used to fit and extrapolate the data is given in Eq. 3.7. This equation is the combination of a second-order accelerating boundary layer (ABL) profile, based upon physical arguments and developed in Soulsby and Dyer (1981), and the log-wake law recommended by Nezu and Nakagawa. H is the water depth; the Kármán constant is $\kappa = 0.41$; the constant $\gamma = 0.04$ was proposed by Soulsby and Dyer to be universal in weakly accelerating boundary layers; the acceleration length scale, Λ, is defined in Eq. 3.8 by the square of the friction velocity divided by its time derivative; β is a constant which, like γ, should be universal in weakly accelerating boundary layers; Π is a fitting parameter that is expected to depend on the particular profile.

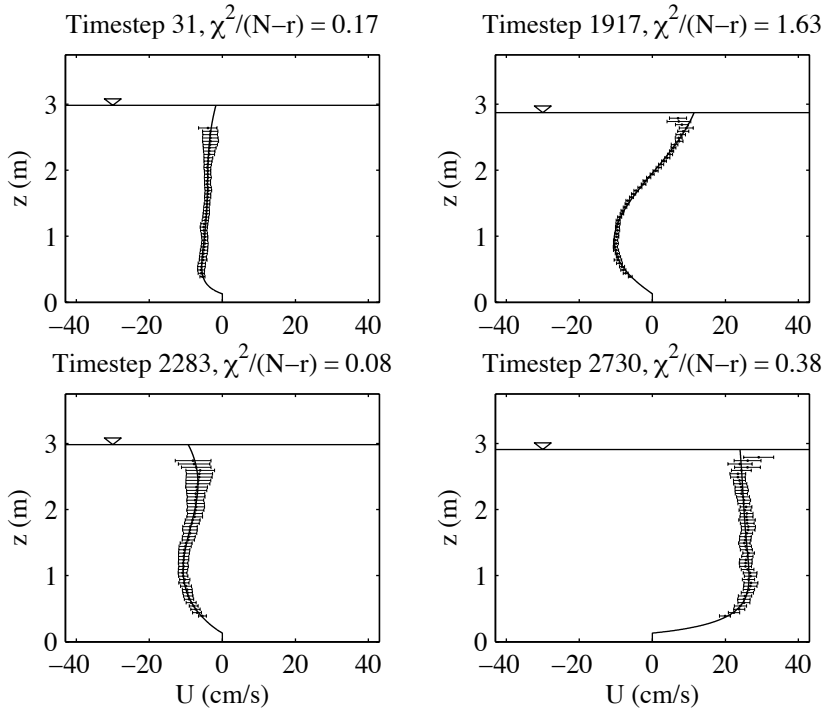

Figure 3.19: A few measured velocity profiles with fitted curves from 2003. Data and 95% confidence intervals are plotted with dots and error bars. The fitted curves, based on Eq. 3.7, are plotted with a solid line.

$$U(z) = \frac{u_*}{\kappa}\left[\ln\left(\frac{z}{z_0}\right) - \frac{z-z_0}{\gamma\Lambda} + \frac{(z-z_0)^2}{\beta\Lambda^2} + 2\Pi\sin^2\left(\frac{\pi}{2}\frac{z-z_0}{H-z_0}\right)\right] \tag{3.7}$$

$$\Lambda = \frac{u_* \mid u_* \mid}{i_*} \tag{3.8}$$

All fits were performed using linear least square minimization with free variables u_*, Λ, β, and Π. Data was weighted by the inverse of the variance representing its uncertainty interval, $\sigma_U^2 = (\delta U/2)^2$. A few of the fitted profiles are plotted in Figure 3.19.

The goodness of fit was estimated by the quantity $\chi^2/(N-r)$, computed as shown in Eq. 3.9, where N is the number of data points, $r = 4$ is the number of degrees of freedom in the linear least squares problem, U_n are the measured veloc-

ities, U_{fitted} are the corresponding fitted velocities, and δU_n is the 95% uncertainty interval for U_n. For 93.5% of the data, $\chi^2 \leq 1$, indicating that the fit was a good one.

$$\frac{\chi^2}{N-r} = \frac{1}{N-r}\sum_{n=1}^{N}\left(\frac{U_n - U_{fitted}}{\frac{1}{2}\delta U_n}\right)^2 \tag{3.9}$$

If Eq. 3.7 truly captures the physics of the boundary layer, we expect that the acceleration length scale, Λ, will be related to the friction velocity, u_*, and the time acceleration of the friction velocity, $\dot{u}_*$, by Eq. 3.8, as proposed by Soulsby and Dyer (1981). We also expect the constant β to be universal. We computed Λ from the fitted values of u_* using Eq. 3.8 and a central difference to compute the time derivative of u_* – we compared these values to the directly fitted values of Λ. The comparison is shown in Figure 3.20 along with a histogram of β. In the top left panel is a scatter plot of the two values of Λ. There appears to be no correlation whatsoever. The correlation function was computed to determine if the values were correlated for some time delay, and it is plotted in the upper right panel. We see that there truly is no correlation between the two values of Λ. Likewise, β does not appear to be universal. We conclude that while the velocity profile given in Eq. 3.7 provides a nice fit to our data and a convenient means for extrapolating to the bed and to the free surface, the acceleration length scale Λ does not have any physical significance. This is unfortunate. If Λ could have been computed from time histories of u_*, and if β had been universal, then because u_* is strongly correlated with the free stream velocities (see Section 3.3.6), we would be able to predict the shape of the second order accelerating velocity profile from a single point measurement. It is disappointing that this is not the case.

Once we obtained fitted curves, they were used to extrapolate the velocity

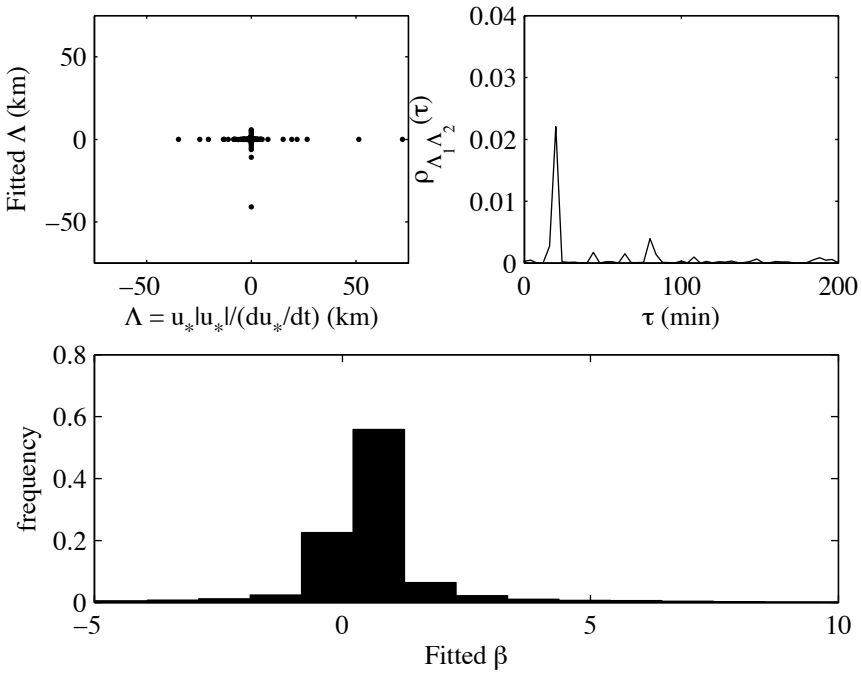

Figure 3.20: In the top left panel is a comparison of Λ from linear least square fit to the velocity data and Λ from Eq. 3.8, where u_* is from fitting the velocity data. In the top right panel is the cross-correlation of these two values of Λ, normalized by the standard deviations of each. In the lower panel is a histogram of β, which we expect to be a universal constant. None of our expectations were met regarding Λ or β.

profile to the surface and to the bed. The 95% uncertainty interval was also extrapolated. The uncertainty of the bottom-most data point was used between the bottom point and the bed. The uncertainty of the top-most point was linearly extrapolated to the surface with a slope given by the slope of the velocity profile near the surface – the velocity slope near the surface was computed from the topmost point and the third point from the top. The extrapolated long-stream velocity and its 95% uncertainty interval are plotted in Figure 3.22.

2002

Because in the 2002 experiment, the first bin is centered nearly an entire meter above the bed, at $z_1 = 0.80m$, we cannot attempt to characterize the bottom boundary layer from the 2002 data. In Section 3.3.6, we have developed a method to extrapolate velocities from the free stream to the bed and to estimate the extrapolation uncertainty – the method is based upon characterization of the boundary layer for 2003 data.

We extrapolate the 2002 data as follows: First, we linearly extrapolate the velocity and the velocity uncertainty to the surface. Then, we extrapolate the velocity to the bed following Eq. 3.5 with $C_d^{1/2} = 0.14$. Next, we compute the extrapolation uncertainty, $\breve{\delta}U(z)$, following Eq. 3.6 with $\breve{\delta}C_d^{1/2}(z) = (0.22m^{-1})z + 0.024$ (see Section 3.3.6). We note that this uncertainty, $\breve{\delta}U(z)$, is most likely due to an error that is correlated over the time scale of the outflow itself. We also expect the error in the measured velocity at $z_1 = 0.80m$ to affect our extrapolated velocities, so we take the uncertainty in the extrapolated boundary layer to be equal to the root sum square of the uncertainty of the velocity measured at $z_1 = 0.80m$ and the extrapolation uncertainty found using Eq. 3.6. In Figure 3.21 we plot the

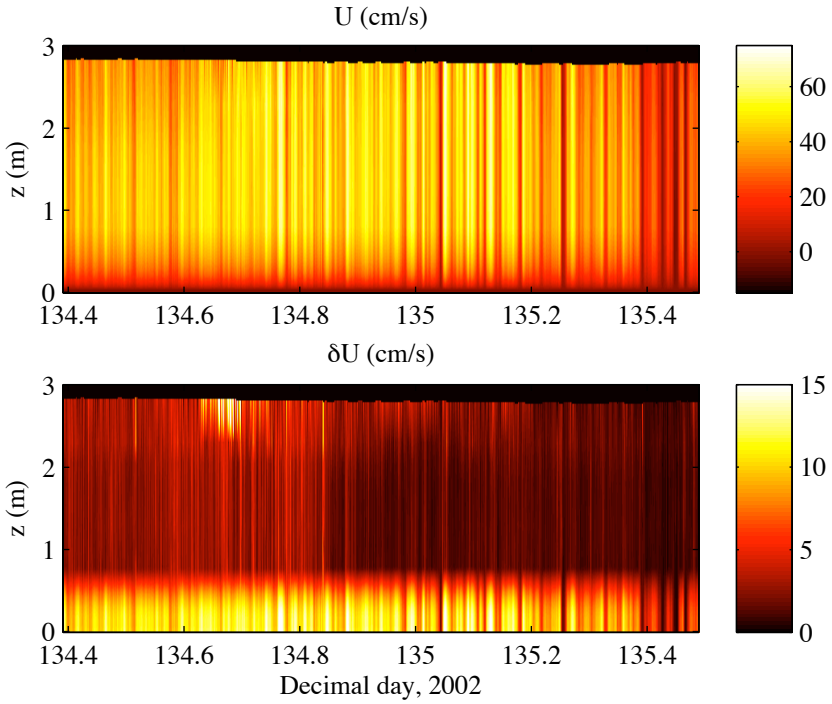

Figure 3.21: Extrapolated long-stream velocity profile and its 95% confidence interval for the 2002 dye experiment.

extrapolated velocity profile and the total uncertainty for the 2002 experiment.

3.3.8 Filling in Missing Data

2003

The 2003 data set was nearly continuous, but there were three periods during which, due to power failure, the ADCP did not measure data. These periods lasted $2.9hrs$, $12.3hrs$, and $10.7hrs$, respectively. To run a numerical model, continuous flow input is necessary, so we decided to fill in the gaps by pasting data from other times into them. We filled each of the three gaps with data from an equal time period coming immediately after the gap. We filled 35 smaller gaps between $4min$ and $28min$ in duration by linearly interpolating the velocity profile in time. For the 95% uncertainty interval at times where large chunks of data were patched, we

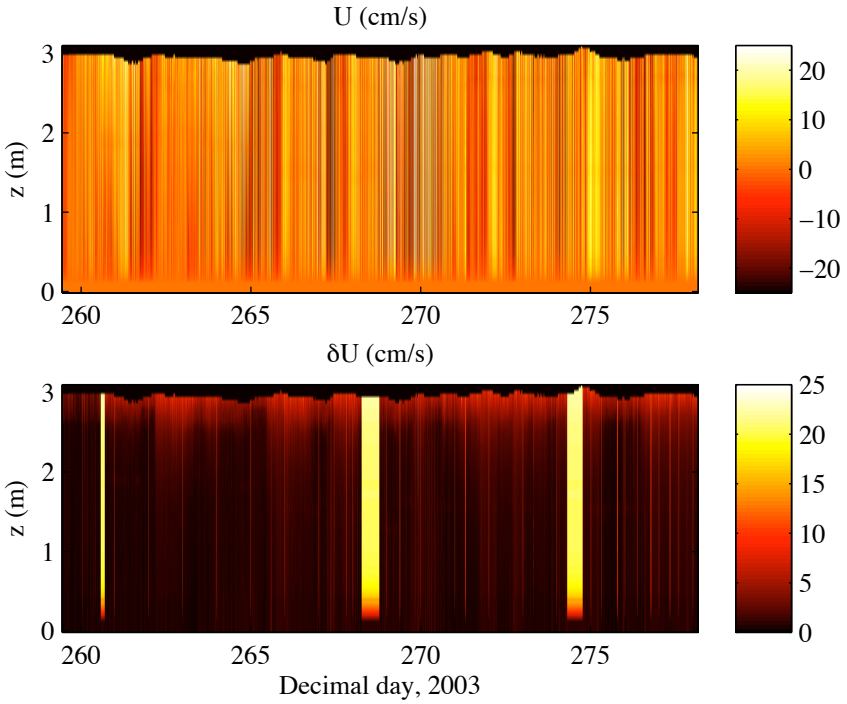

Figure 3.22: Extrapolated long-stream velocity and 95% uncertainty interval with missing data filled in for the 2003 dye experiment.

used twice the standard deviation of the velocity, computed at each depth from the entire time series. For the smaller chunks, we used one standard deviation. Figure 3.22 shows the extrapolated velocity profile with the missing data filled in along with the 95% confidence interval.

2002

There was no data missing in time for the May 2002 ADCP data. This was because we powered the ADCP with internal batteries, and the experiment was short enough that they lasted for all of it.

3.4 Horizontal Velocity Profiles

Here we analyze the $4.7hrs$ of horizontal velocity profile data collected with the $600kHz$ ADCP operating with only two beams and looking across the channel. Let us define a coordinate system so that x points in the long-channel direction toward LO, y points across the channel (roughly from east to west) with the origin on the east wall, and z points up – see Figure 2.10. Let us define U, V, and W to be the mean velocities in the x, y, and z directions, respectively. Finally, let us denote the channel half-width by d and the full channel width by D. Our goal is to parameterize the bulk velocity, $\overline{U}$, defined by Eq. 3.10, in terms of the centerline velocity $U_0 \equiv U(y = d)$.

$$\overline{U} \equiv \frac{1}{D} \int_0^D U(y) dy \tag{3.10}$$

3.4.1 Ensemble Averaging

By trial and error, an $8min$ ensemble length was found to resolve the acceleration and deceleration of flow through the channel while smoothing out turbulent fluctuations across the channel, so this interval was chosen for ensemble averaging. Ensembles for which more than 5% of the data was missing were thrown out entirely, leaving 21 ensemble-averaged velocity profiles.

3.4.2 Transforming from Beam to Channel Coordinates

The ADCP physically measures velocities pointing into each of its beams – these are the beam coordinate velocities. Our coordinate system, including the velocity vectors, is shown in Figure 3.23. Working under the assumption that velocities are

homogenous in the direction perpendicular to the beam bisector (over sufficiently long time scales), we converted ensemble-averaged beam velocities, U_3 and U_4, to channel coordinate velocities, U and V, using Eq. 3.11. Because only two beams were used, only two velocity components were measured, and there is no estimate of the error velocity. We examined the ratio of the cross-stream to long-stream ensemble-averaged velocities, V/U, and found that it was always small, as seen in Figure 3.24.

$$\begin{aligned} U &= \frac{U_3 - U_4}{2\sin\theta} \\ V &= -\frac{U_3 + U_4}{2\cos\theta} \end{aligned} \tag{3.11}$$

3.4.3 Extrapolating to the Walls

Because of acoustic blanking near the east wall and reflections in the bin containing the west wall, we did not measure velocities nearest to the wall. This is a problem because we are interested in boundary layer velocities. In order to compute bulk velocities, we again had to extrapolate the velocity to the walls. We used a linear least squares fit to Soulsby and Dyer's accelerating boundary layer profile given in Eq. 3.12 with constants $\kappa = 0.41$ and $\gamma = 0.04$, defining the roughness height y_0 to be the height of the corrugated steel piling ($22cm$ and $18cm$ for the east and west walls, respectively), and letting u_* and Λ be free variables.

$$U(y) = \frac{u_*}{\kappa}\left[\ln\left(\frac{y}{y_0}\right) - \frac{y - y_0}{\gamma\Lambda}\right] \tag{3.12}$$

All but one of the velocity profiles are plotted in Figure 3.25. The fitted accelerating boundary layer profiles are plotted as thick lines, and fitted logarithmic

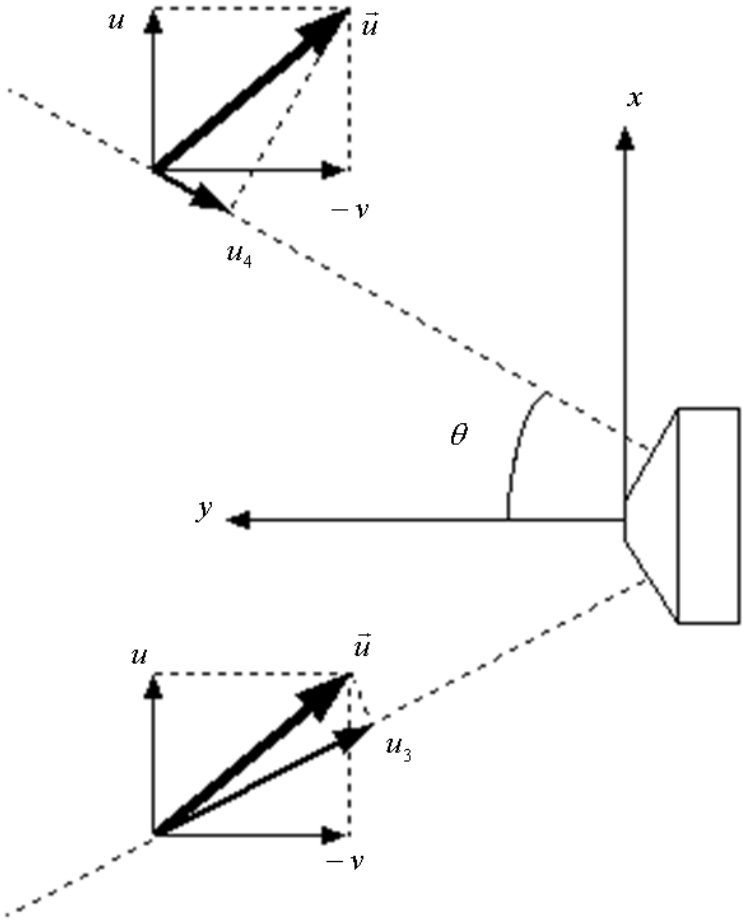

Figure 3.23: Coordinate system for the 2004 horizontal boundary layer experiment, showing dual beam configuration.

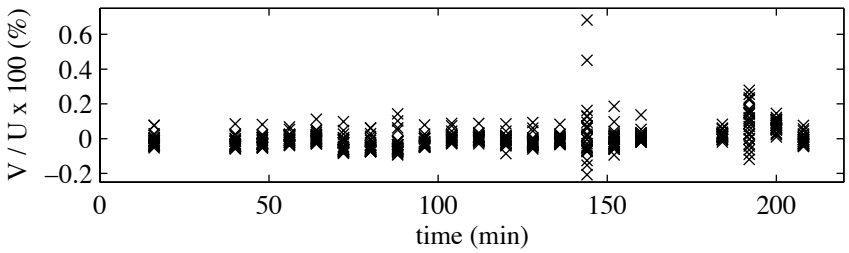

Figure 3.24: Ratio of cross-stream to long-stream velocity in each bin and at each time step during the 2004 experiment. Note that ratio is given in percent units, and it is very small.

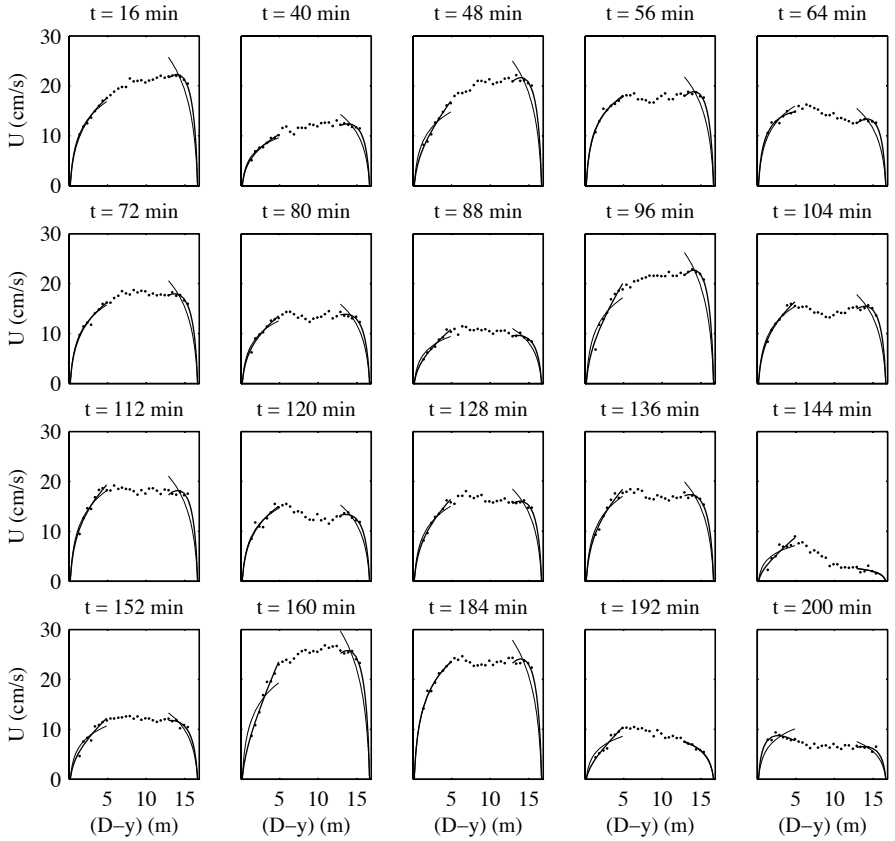

Figure 3.25: 20 of the 21 ensemble-averaged horizontal velocity profiles (the 21st did not fit nicely on the plot) are plotted as dots. The thin lines are logarithmic fits to the near-wall points. The thick lines are linear least square fits of Eq. 3.12 to the near-wall points.

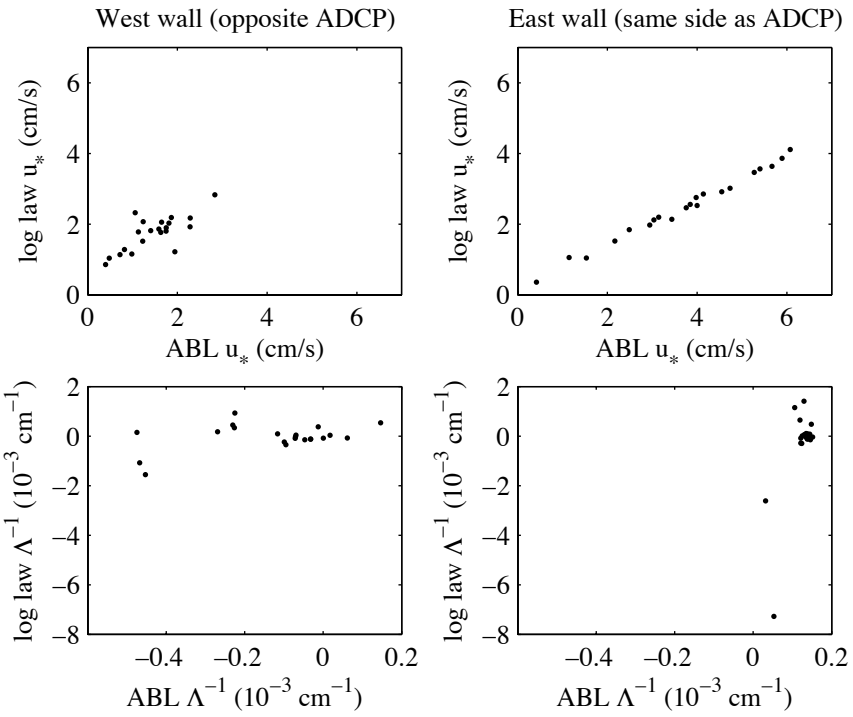

Figure 3.26: A comparison of u_* from the accelerating boundary layer (ABL) and log law fits to the near-wall points, and a comparison of Λ from the ABL fit and Λ computed from u_* and its time acceleration using Eq. 3.8.

profiles are plotted as thin lines. The accelerating boundary layer profile is clearly a better fit, although the difference that the linear term makes in the values of the extrapolated profile is minimal.

In Figure 3.26, we compare the values of u_* and Λ obtained by the linear least square fitting of Eq. 3.12 and the values obtained by a log law fit and the definition of Λ given in Eq. 3.8. We see that the values of u_* are well-correlated, but that the values of Λ are not. We reach the unfortunate conclusion that we cannot predict the value of Λ from u_*, as was the case for the bottom boundary layer (see Section 3.3.7).

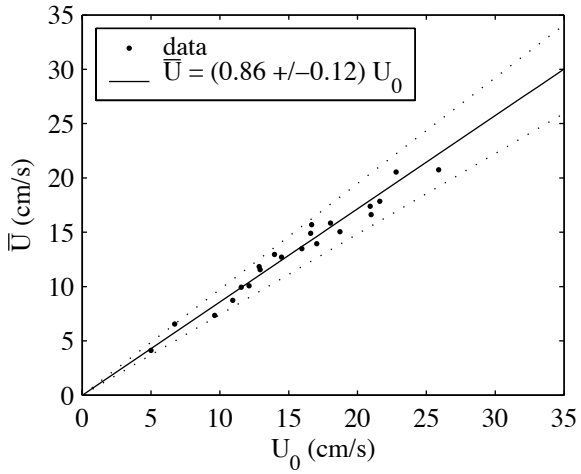

Figure 3.27: Linear fit to bulk velocity, $\overline{U}$, vs. centerline velocity, U_0, with 95% confidence interval.

3.4.4 Predicting Bulk Velocity from Centerline Velocity

The extrapolated profiles were integrated to obtain the bulk velocity as defined in Eq. 3.10, and the bulk velocity was found to vary linearly with the centerline velocity over the range of our measurements, as given in Eq. 3.13 with $\theta = 0.86$. The data and fitted line are plotted in Figure 3.27. There is quite a bit of excursion from this predictive curve, and it is likely that these excursions are due to physical processes that were not accounted for (as opposed to instrument noise), so for the purpose of predicting bulk velocities from centerline velocities, we wish to estimate the uncertainty of the linear fit. We directly compute the error for each data point, $\Delta\theta = \frac{\overline{U}}{U_0} - \theta$, and take twice its standard deviation to be the 95% confidence interval $\delta\theta = 0.12$. We will assume that the error leading to this uncertainty is correlated over the autocorrelation time scale of the outflow, and thus we denote $\delta\theta = \breve{\delta}\theta$.

$$\overline{U} = \theta U_0 \tag{3.13}$$

3.5 Computing Outflow

In this section we estimate outflow through the SP channel into LO from the continuous vertical velocity profiles, the results of the single horizontal boundary layer experiment, and the bathymetry of the channel cross-section. We propagate uncertainty from these various sources to find uncertainty in the outflow measurement.

2003

Beginning with centerline long-stream velocity measured by the $1200kHz$ ADCP as a function of depth and time, $U_0 = U$, we convert to bulk velocity using Eq. 3.13, where $\theta = 0.86$. This is a straightforward procedure, but propagating uncertainty in the various measured quantities is more subtle. Following Kline and McClintock (1953), the uncertainty $\delta\overline{U}$ is related to $\delta\theta$ and δU by Eq. 3.14.

$$\delta\overline{U} = \sqrt{(\theta\delta U)^2 + (U\delta\theta)^2} \tag{3.14}$$

As we will soon be integrating over the vertical coordinate z, it is important to determine whether the error $\Delta\overline{U}$ is biased or uncorrelated in z. Recall that the large part of ΔU is due uncertainty in the ensemble average over time. We may reason that uncertainty in the ensemble average is due to accelerations and decelerations, which will generally be correlated in space. Thus, we may expect ΔU to be biased in z. Because we have no reasonable argument for assuming that $\Delta\theta$ is uncorrelated in z, we will assume that it is also biased in z.

Later on, in computing residence times, we will be integrating in time as well, and it will be important to know how $\Delta\overline{U}$ is correlated in time. Because both ΔU and $\Delta\theta$ are correlated over the autocorrelation time scale of the outflow, as

we have reasoned in the preceding sections, $\Delta\overline{U}$ will also be correlated over this time-scale, and thus we denote the resulting uncertainty $\breve{\delta}\overline{U}$.

To convert bulk velocity to outflow, we multiply by the channel width, $D(z)$, and integrate discretely in z, as shown in Eq. 3.15, where $z_1 ... z_K$ span the entire water column. Channel width is plotted as a function of depth in Figure 2.9.

$$Q(t) = \sum_{k=1}^{K} D(z_k)\overline{U}(z_k, t)\Delta z \tag{3.15}$$

We estimate the uncertainty in measuring channel width (width was measured at the top of a channel with a tape measure, and calculated as a function of depth from the bathymetry data) as $\delta D = 0.5m$ – this error is biased in both space and time. Under these assumptions, and following Kline and McClintock (1953), our uncertainties propagate as given in Eq. 3.16, and the total uncertainty in outflow $Q(t)$ at time t is given by Eq. 3.17. Outflow and the two contributions to its uncertainty are plotted in Figure 3.28.

$$\begin{aligned} \bar{\delta}Q &= \sum_{k=1}^{K} \overline{U}(z_k, t)\delta D(z_k)\Delta z \\ \breve{\delta}Q &= \sum_{k=1}^{K} D(z_k)\breve{\delta}\overline{U}(z_k, t)\Delta z \end{aligned} \tag{3.16}$$

$$\delta Q = \sqrt{\bar{\delta}Q^2 + \breve{\delta}Q^2} \tag{3.17}$$

For the outflow measurements, errors which are neither biased indefinitely nor random in time are thought to be correlated over the autocorrelation time scale of the outflow. The autocorrelation of outflow, $Q(t)$ is plotted in Figure 3.29. After three ensemble-averaging periods (12 minutes), the autocorrelation function

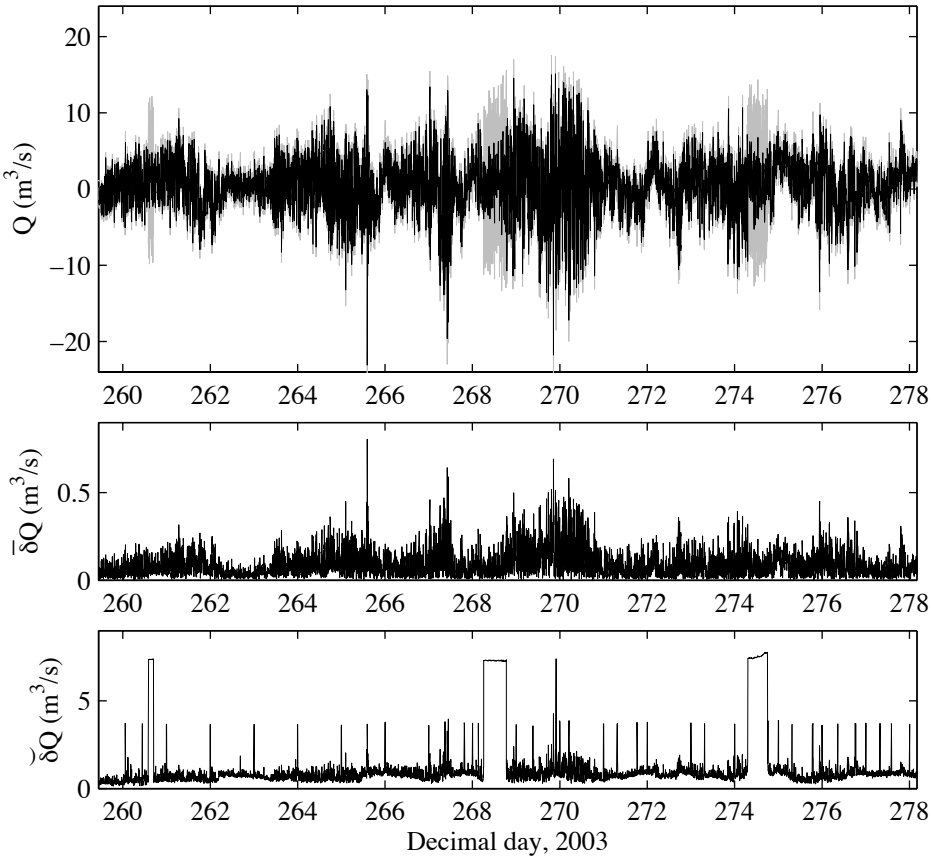

Figure 3.28: Outflow from SP, instantaneous 95% confidence interval (shaded area), and two contributions to total uncertainty that are correlated over different time scales during the 2003 experiment.

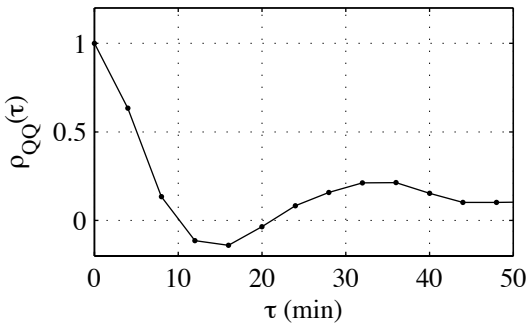

Figure 3.29: Autocorrelation of outflow from SP to LO for the 2003 experiment.

$\rho_{QQ}(\tau)$ has crossed below zero, so we take $\tau_Q = 12min$ to be the correlation time for $\breve{\delta}Q$.

We were interested to know how much difference correcting for the horizontal boundary layers using Eq. 3.13 makes in comparison to our uncertainty in Q. We estimated outflow by assuming that velocity is constant across the channel (i.e. avoiding Eq. 3.13). Let us call this outflow estimate Q_{old}. In Figure 3.30, we compare $Q - Q_{old}$ to the total uncertainty δQ and see that they are the same order of magnitude. A further inspection of the error sources (not shown) reveals that uncertainty in θ and U both contribute to first order to the uncertainty in Q, so that reducing uncertainty in these quantities would most effectively reduce the overall uncertainty.

After writing this section, the author has rethought the problem of estimating uncertainty in the velocity measurements. The idea behind the ensemble average was to find a mean velocity that was representative of flow across the entire channel. We chose the $4min$ ensemble window to average over turbulent fluctuations but avoid averaging over fluctuations due to inviscid quasi-periodic processes such as barotropic seiching. Our hope was that the velocity would be quasi-steady within this window. The high bootstrap uncertainty interval originates from trends in

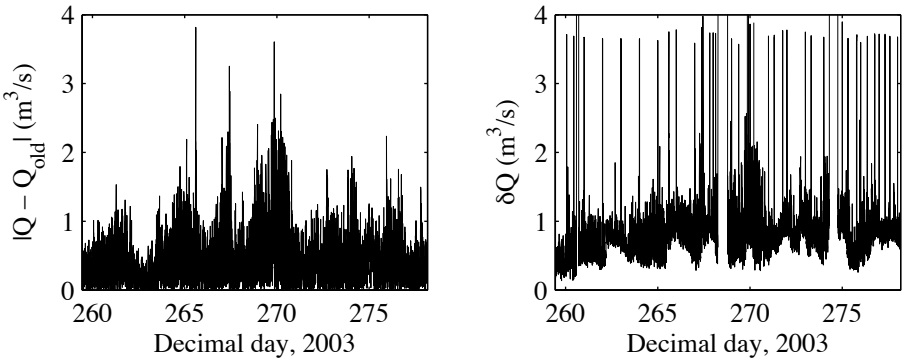

Figure 3.30: A comparison of the difference that correcting for horizontal boundary layers makes in the estimate of outflow and the total uncertainty in the outflow estimate. We see that they are very close in magnitude.

the data over the ensemble window, i.e. from the fact that "quasi" in "quasi-steady" is significant. Thus, we believe it would be better to estimate the mean velocity at each $5s$ time step in the ADCP record by taking an $4min$ moving average (or using another kind of filter). To estimate the uncertainty, we would subtract the moving average to get a de-trended fluctuating velocity, and find the 95% bootstrap confidence interval of the mean fluctuation. This uncertainty would be a better representation of our uncertainty in the mean flow, measured at the channel centerline, and representative of flow across the channel. It would be significantly smaller than the present value of δU. However, unless we could also reduce the uncertainty $\delta\theta$, δQ would not be reduced significantly. Thus, it is not worthwhile to do this rather time-consuming analysis unless we plan to better characterize the horizontal boundary layers.

2002

As for the 2003 experiment, we convert U to $\overline{U}$ using Eq. 3.13, and we estimate error in $\overline{U}$ using Eq. 3.14. Recall that by matching backscatter intensity with water surface elevation data that was referenced to IGLD85, we found that the elevation

of the bed underneath the ADCP during the 2002 experiment was $72.42m$ above IGLD85. Recall also that the deepest point in the channel is $71.58m$ above IGLD85. It appears that for the 2002 experiment, the ADCP was not at the deepest point in the channel, but rather $0.84m$ above the deepest point. We are not sure of this because we did not measure the bathymetry of the channel during the 2002 experiment – it is possible that the ADCP was in fact at the deepest point but that the channel was full of sediment from spring runoff. In order to compute our best estimate of the outflow, we will assume that the ADCP was $0.42m$ above the deepest point and attribute a 95% uncertainty of $0.42m$ to this assumption. This allows for the two extreme situations we have considered. We elongate the velocity profile in the middle to stretch it over an extra $0.42m$, and in this elongated portion, we attribute an uncertainty interval equal to the velocity itself. This uncertainty is due to a bias error, so we denote it by $\overline{\delta U}$.

$$\begin{aligned} \bar{\delta}Q &= \sum_{k=1}^{k=K} \sqrt{\left[D(z_k)\overline{\delta U}(z_k,t)\right]^2 + \left[\overline{U}(z_k,t)\delta D(z_k)\right]^2}\Delta z \\ \breve{\delta}Q &= \sum_{k=1}^{k=K} D(z_k)\breve{\delta}\overline{U}(z_k,t)\Delta z \end{aligned} \tag{3.18}$$

Outflow, Q, and its uncertainty intervals are computed exactly as for the 2003 experiment, except that the we have an additional bias error due to uncertainty in the channel bathymetry. Thus, the two contributions to uncertainty in outflow are computed according to Eq. 3.18. The outflow and its two sources of uncertainty for the 2002 experiment are plotted in Figure 3.31.

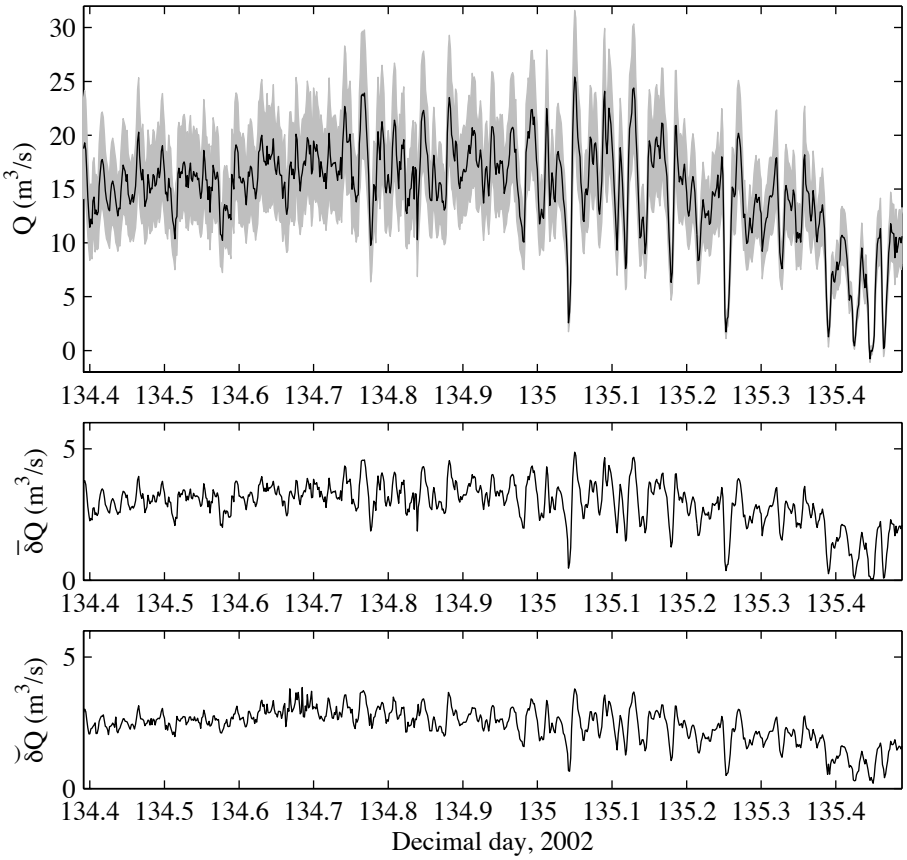

Figure 3.31: Outflow from SP, instantaneous 95% confidence interval (shaded area), and two contributions to total uncertainty that are correlated over different time scales during the 2002 experiment.

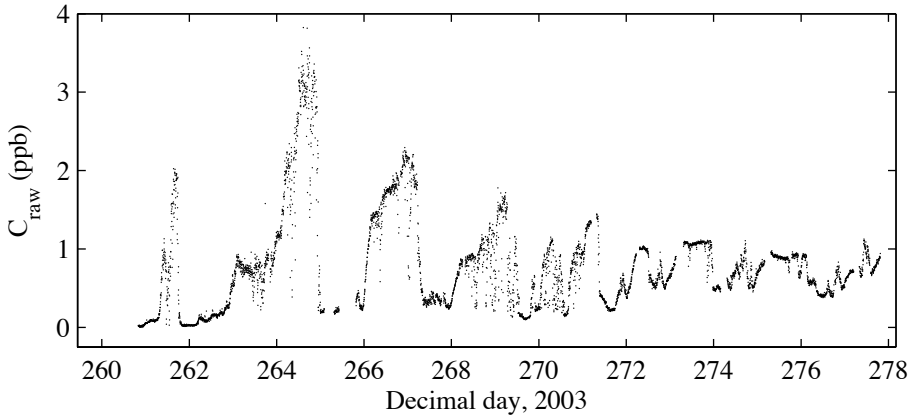

Figure 3.32: Time history of concentration in the channel as reported by the 10-AU (uncorrected) for the 2003 dye experiment.

3.6 Concentration

3.6.1 Raw Concentration Data

2003

The 10-AU operated nearly continuously for over 17 days during the 2003 experiment. The time series of concentration reported by the 10-AU is plotted in Figure 3.32 with a $21s$ time delay to account for travel time from the intake to the flow cell. Note that there are a few short chunks of missing data visible in this time series. These were lost due to power failure, and are later filled in by linear interpolation.

2002

The 10-AU operated for slightly over $7hrs$ before the concentration leveled out and we assumed the dye had mostly left the bay. The uncorrected concentration record is plotted in Figure 3.33 with a $21s$ time delay to account for travel time from the intake to the flow cell. Data is missing due to a $1hr$ power failure.

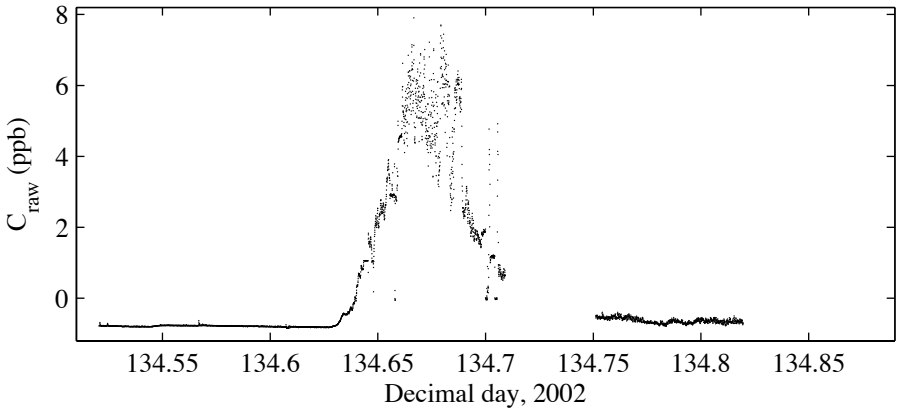

Figure 3.33: Time history of concentration in the channel as reported by the 10-AU (uncorrected) for the 2002 dye experiment.

3.6.2 Correcting Concentration Bias

2003

In Section 4.4.2 we recommend a procedure for keeping the flow cell of the 10-AU or any other flow-through fluorometer clean and calibrated during a long tracer study. It would have improved our measurements if we had periodically performed such a procedure during the 2003 dye experiment. As it is, we must do something to correct for fluorometer drift caused by the increasingly dirty flow cell. We use the ad-hoc Eq. 3.19 to make this correction, where $C_{raw}(t)$ is the concentration reported by the 10-AU, $C(t)$ is the corrected concentration, $C_0(t)$ is a function modeling drift of the zero concentration reading, and $A(t)$ is a function modeling attenuation of the concentration reading. Our ad-hoc hypothesis is that while the zero concentration reading was biased positively by the grime inside the flow cell, the amount of light that was able to pass through the flow cell was attenuated by that same grime, and thus the concentration reading was diminished by some multiplicative coefficient, $A(t)$.

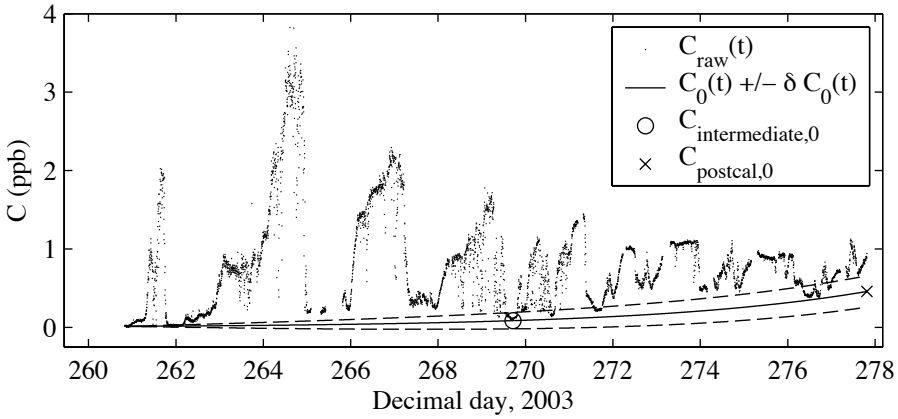

Figure 3.34: Time-dependent blank curve, $C_0(t)$ defined by the ad-hoc Eq. 3.20 and the two points (intermediate and postcal), plotted with uncertainty interval, $\delta C_0(t)$, defined by Eq. 3.23 along with raw 10-AU concentration data (plotted every $20sec$).

$$C(t) = A(t)\,[C_{raw}(t) - C_0(t)] \tag{3.19}$$

To model $C_0(t)$, we reason that the largely biological matter that we found inside the 10-AU flow cell probably accumulated exponentially, and we use the function described by Eq. 3.20, where $C_{0,postcal} = 0.46ppb$ is the concentration reported by the 10-AU for the post-calibration blank and $t_{postcal}$ is the time of post-calibration. To define K_0, we needed another blank. For this blank, we turn to the record of $C_{raw}(t)$, plotted in Figure 3.32, and look for a strong local dip in concentration. We see a strong dip down to $0.087ppb$ at decimal day 269.71. Examining the ADCP velocity record, we see that this dip falls after a $30min$ inrush of water from LO and after a $5hr$ period of flows mostly from LO into SP, so we have reason to believe that this water is relatively free of RWT, and we use this extra "blank" to compute $K_0 = 0.21/day$. The resulting blank curve, $C_0(t)$, is plotted in Figure 3.34.

$$C_0(t) = C_{0,postcal} e^{K_0(t-t_{postcal})} \tag{3.20}$$

$$A(t) = A_{postcal} e^{K_A(t-t_{postcal})} \tag{3.21}$$

$$A_{postcal} = \frac{\hat{C}_{3,postcal}}{C_{3,postcal} - C_{0,postcal}} \tag{3.22}$$

To model $A(t)$, we again use an exponential function, given by Eq. 3.21, where $A_{postcal}$ is the value of the attenuation coefficient at the time of post-calibration, computed as shown in Eq. 3.22. Here, $\hat{C}_{3,postcal} = 3.0ppb$ is the concentration of RWT in the fish tank used for the post-calibration standard, and $C_{3,postcal} = 3.16ppb$ is the concentration reported by the 10-AU for this standard. Eq. 3.22 gives us $A_{postcal} = 1.11$. Note that computing $A_{postcal}$ using the the $6.0ppb$ and $9.0ppb$ post-calibration standards gives the same value within 0.3% and 2%, respectively. The value of $A(t)$ at the beginning of the dye experiment is 1. These two points yield $K_A = 0.0063/day$.

Our biggest source of uncertainty in the 2003 concentration measurements is in the validity of Eq. 3.19, used to correct concentration, and of the exponential models used for $C_0(t)$ and $A(t)$. Since we observed the 10-AU reading change by $0.02ppb$ upon removing the hose at the end of the experiment, and since we observed the reading drop $0.15ppb$ when we flushed the flow cell with several batches of distilled water, we reason that towards the end of the experiment, the value of C_0 may have fluctuated by as much as $0.2ppb$ over short time scales in response to changing water quality. As an ad-hoc estimation of uncertainty for our ad-hoc model of C_0, we will use a function that linearly increases from $0ppb$ to $0.2ppb$ by the end of the experiment. This ad-hoc uncertainty approximation is given in

Eq. 3.23, where t is time and t_{cal} and $t_{postcal}$ are times of calibration and post-calibration, respectively – the uncertainty interval is plotted in Figure 3.34. We will assume that this error is correlated over a time scale of $\tau_C = 1day$, which is roughly the time scale of large observed changes in concentration in the channel. Choice of this time scale is somewhat arbitrary – our reasoning for choosing it is that this error is clearly not a bias error, but probably remains somewhat correlated between dramatic changes in flow conditions. We will denote all uncertainties due to errors that are correlated over time scale $\tau_C = 1day$ with at hat. For example, the uncertainty in C_0 is denoted $\hat{\delta}C_0$.

$$\hat{\delta}C_0(t) = (0.2ppb)\frac{t - t_{cal}}{t_{postcal} - t_{cal}} \tag{3.23}$$

Now, let us consider uncertainty in $A(t)$, beginning with $A_{postcal}$, the value at the time of post-calibration, computed using Eq. 3.22. Uncertainty in the concentration of the post-calibration standard solution propagates into uncertainty in $A_{postcal}$ as shown in Eq. 3.24. Note that with this uncertainty, there may not be any attenuation to speak of, as $A_{postcal} - \delta A_{postcal} = 1.11 - 0.09 = 1.02$, which corresponds to 2% attenuation. On the other hand, we might have 20% attenuation, so we will not scrap the model. As we did for $C_0(t)$, let us assume that our uncertainty in $A(t)$ increases linearly from 0 to 0.09 throughout the experiment, as given in Eq. 3.25. Let us assume that this error is correlated over time scale $\tau_C = 1day$, and denote the uncertainty $\hat{\delta}A(t)$.

$$\delta A_{postcal} = \frac{\delta \hat{C}_{postcal,3}}{C_{postcal,3} - C_{postcal,0}} = \frac{0.25ppb}{3.16ppb - 0.46ppb} = 0.09 \tag{3.24}$$

$$\hat{\delta}A(t) = 0.09\frac{t - t_{cal}}{t_{postcal} - t_{cal}} \tag{3.25}$$

2002

If our theory that the blank was contaminated with RWT is correct, and if the contaminating RWT became well-mixed during the blank reading so that the subsequent standard solution was biased by the same amount as the blank, then all of the concentration data for the 2002 experiment was biased by that same amount, and we may obtain the correct concentration using Eq. 3.26, where C_0 is a constant bias.

$$C(t) = C_{raw}(t) + C_0 \tag{3.26}$$

If this is the case, a single valid blank measurement with the calibrated 10-AU will tell us the value of C_0. We conveniently have over $2.5hrs$ of in-situ blank data before the dye arrives in the channel. We see that during this $2.5hr$ period, the raw concentration varies slowly between $-0.77ppb$ and $-0.82ppb$, with the exception of a few sharp spikes of order $0.1ppb$, dipping to the low of $-0.82ppb$ just before the plume arrives at the channel. We take the lowest sustained dip to be the blanking bias, $C_0 = 0.82ppb$, and correct the measured concentration data using Eq. 3.26. We note that $0.82ppb$ is over five times the maximum bias of $0.16ppb$ that we observed for changing light conditions, so we conclude that this large bias must have been due to either contamination of the original blank by RWT or fluorescent material in the watershed runoff from Sterling Creek.

Our problems with the blank are the largest source of uncertainty for the 2002 experiment. Let us now consider this uncertainty. We observe the 10-AU signal drift between -0.77 and $-0.82ppb$ while it is in the clean channel with a few sharp spikes of around $0.1ppb$ – this would suggest that our uncertainty in the blanking bias, C_0, is order $0.1ppb$. Let us consider a worst case scenario. Suppose that there

was RWT inside the pump during our calibration, that $0.82ppb$ was released into the tank during the blank, but then that suddenly, between the blank and the standard calibration, an extra $1ppb$ washed out and contaminated our standard solution. The standard concentration was something between $10ppb$ and $40ppb$ (exact value not in field notes – author was not present for experiment). This could have resulted in additional bias up to 10%. Considering all of this, we make a conservative judgement, and decide to attribute an uncertainty due to bias error of $\bar{\delta}C(t) = 0.1ppb + 0.1C(t)$ to our concentration data.

3.6.3 Some Other Sources of Uncertainty in 2003

For the 2003 experiment, sources of uncertainty in measured concentration include the sensitivity of the 10-AU itself, the sensitivity of the thermometer inside the 10-AU used for internal temperature corrections, uncertainty in the concentration of various calibration solutions and post-calibration solutions, the validity of the exponential models we pulled out of our hat to represent blank drift and attenuation within the flow cell, the validity of the model we used to estimate blank drift and attenuation in the first place, the changing effect of dirty hoses and pumps toward the end of the experiment, and information lost in the ensemble average (discussed in Section 3.6.6). We have already discussed uncertainty in our estimates of concentration due to the validity of our models of calibration drift and we will soon discuss information lost in the ensemble average. As none of the errors discussed so far is particularly large in the 2003 experiment, it is worthwhile to discuss some other possible significant sources of uncertainty, and we will do so in this section. We will follow the method described by Kline and McClintock (1953) throughout. Note that for the 2002 experiment, the sources of uncertainty

discussed in this section are small compared to the uncertainty estimated in other sections.

Sensitivity Error

According to the manual, the 10-AU sensitivity is the greater of $1/(5 \times 10^6)$ of full scale (in this case full scale is $20ppb$, so this corresponds to $0.000004ppb$), or $0.01ppb$ in potable water. We observed random fluctuations of $\pm 0.015ppb$ from measurement to measurement during our post-calibration, so we conclude that in the field, the 10-AU may be slightly less sensitive, and we take our uncertainty due to instrument sensitivity to be $\tilde{\delta}C_{sensitivity} = 0.015ppb$. Note that this error is uncorrelated in time, but that it leaves a bias error frozen into all calibration settings and post-calibration measurements. This frozen uncertainty is captured by a bootstrap of the mean for our post-calibration measurements, but for the original calibration, for which 15 samples were averaged by the 10-AU, but not reported, we may estimate the frozen error to have uncertainty $\bar{\delta}C_{sensitivity} = \frac{1}{\sqrt{15}}\tilde{\delta}C_{sensitivity} = 0.004ppb$. Compared to uncertainty stemming from bias error in the calibration solution concentration (to be discussed shortly), this uncertainty is very small, so we will ignore it in our analysis.

Temperature Correction Error

The 10-AU temperature correction package internally adjusts concentration measurements to account for the dependence of RWT fluorescence on temperature using Eq. 3.27 (Turner Designs, personal communication), where I_{raw} is the observed fluorescent intensity, I is the corrected fluorescent intensity, ΔT the difference between the sample temperature and the temperature of the sample at calibration,

and $n = 0.026/^oC$ is the temperature coefficient for RWT.

$$I = I_{raw} \exp\{n\Delta T\} \tag{3.27}$$

The 10-AU manual cites a temperature probe sensitivity of $\tilde{\delta}T = 0.09^oC$. Since there are sensitivity errors in both the measurement of sample temperature and calibration sample temperature, this results in an uncertainty in ΔT of $\sqrt{2}\,\tilde{\delta}T$, which propagates to produce a fluorescent intensity uncertainty of $\tilde{\delta}I = I\exp\{n\Delta T\}\sqrt{2}\,n\tilde{\delta}T$. Now we must determine how this uncertainty propagates into concentration measurements. The 10-AU computes concentration using Eq. 3.28, where the approximation holds when $I_{blank} \approx 0$, which is true in our case. We thus find that the uncertainty in concentration due to temperature sensitivity errors is given by $\tilde{\delta}C_{temperature} = C_{raw}\exp\{n\Delta T\}\sqrt{2}\,n\tilde{\delta}T$.

$$C_{raw} = C_{standard}\frac{I - I_{blank}}{I_{standard} - I_{blank}} \approx \frac{C_{standard}}{I_{standard}}I \tag{3.28}$$

We did not record the temperature of the sample used for calibration, but temperatures observed in the channel during the experiment were in the range 8^oC to 25^oC. For the worst case of $\Delta T = 17^oC$, this works out to an uncertainty in the concentration equal to $\tilde{\delta}C_{temperature} = 0.005C_{raw}$. Since our concentrations do not go above $4ppb$, we observe that uncertainty due to temperature probe sensitivity is almost always smaller than uncertainty due to fluorescence sensitivity, and usually much smaller. Thus, we will ignore uncertainty due to temperature fluctuations.

Calibration Error

Now let us consider uncertainty in the concentration of the various calibration and post-calibration solutions that we mixed. Errors made in mixing the calibra-

tion solution show up as bias errors in the concentration measurement, so they are important. Because we used the post-calibration measurements to adjust our raw concentration data, as described earlier in this section, uncertainties in the concentration of the post-calibration error are also important. A schematic of the procedure for mixing a calibration or post-calibration solution is shown in Figure 3.35. The concentration of the calibration solution, $\hat{C}$, is given by Eq. 3.29, and the total uncertainty in $\hat{C}$ is related to the values and uncertainties in the various concentrations and volumes involved in mixing the solution by Eq. 3.30. A table of these values and uncertainties and of the resulting values and uncertainties of the RWT concentration in our calibration and post-calibration solutions are given in Table 3.1. The pipettes used to mix the solutions were Wheaton Socorex 100-1000μL pipettes, and the flask was a Nalgene polypropylene screw-top volumetric flask. Our uncertainty estimates for volumes measured in the pipettes and flasks, listed in Table 3.1, are slightly conservative compared to the manufacturer specifications. Following Eq. 3.30 and the values in the table, we find that $\hat{C}_{20,cal} = 20.0 \pm 0.46 ppb$, and that $\hat{C}_{3,postcal} = 3.0 \pm 0.25 ppb$.

$$\hat{C} = \frac{C_S V_{P1} V_{P2}}{V_F V_T} \tag{3.29}$$

$$\begin{aligned} \delta\hat{C} \;=\; & \left(\left[\frac{V_{P1} V_{P2}}{V_F V_T} \delta C_S \right]^2 + \left[\frac{C_S V_{P2}}{V_F V_T} \delta V_{P1} \right]^2 + \left[\frac{C_S V_{P1}}{V_F V_T} \delta V_{P2} \right]^2 \right. \\ & \left. + \left[\frac{C_S}{V_F^2 V_T} \delta V_F \right]^2 + \left[\frac{C_S V_{P1} V_{P2}}{V_F V_T^2} \delta V_T \right]^2 \right)^{1/2} \end{aligned} \tag{3.30}$$

The 10-AU computes the concentration C_{raw} that it reports using Eq. 3.31, where $\hat{C}_{20,cal}$ is the concentration programmed in for the standard, $I_{standard}$ and I_{blank} are the corresponding fluorescent intensities measured during calibration,

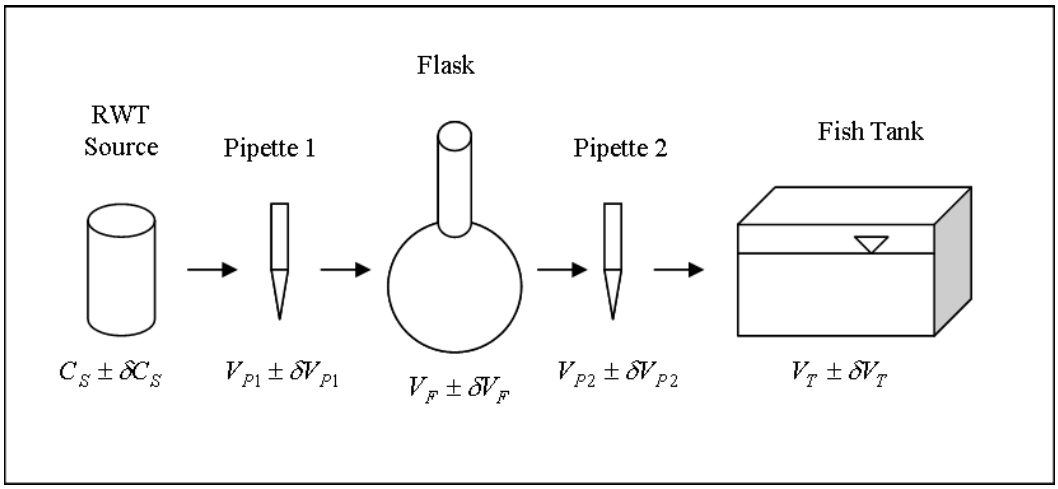

Figure 3.35: Schematic showing how calibration and post-calibration solutions were mixed. A volume of V_{P1} was extracted from a source of RWT with known concentration, C_S, and added to a flask containing volume V_F of distilled water. A volume of V_{P2} was then extracted from the mixed solution in the flask and transferred to a fish tank containing volume V_T of water.

Table 3.1: Concentrations and volumes involved in mixing RWT solutions for calibration and post-calibration. The concentration of the solution, $\hat{C}$, and its uncertainty, $\delta\hat{C}$ are computed from the first five items in the table using Eqs. 3.29 and 3.30, respectively.

	Calibration	Post-calibration
$C_S \pm \delta C_S$	0.20 ± 0.00	0.025 ± 0.001
$V_{P1} \pm \delta V_{P1}$	$0.350 \pm 0.007mL$	$0.420 \pm 0.007mL$
$V_F \pm \delta V_F$	$250 \pm 2mL$	$250 \pm 2mL$
$V_{P2} \pm \delta V_{P2}$	$1.000 \pm 0.007mL$	$1.000 \pm 0.007mL$
$V_T \pm \delta V_T$	$14000 \pm 50mL$	$14000 \pm 50mL$
$\hat{C} \pm \delta\hat{C}$	$20.0 \pm 0.46ppb$	$3.0 \pm 0.25ppb$

and I is the sample intensity. Thus, uncertainty in the concentration of the standard solution during calibration propagates into uncertainty in the raw reported concentration following Eq. 3.32. The uncertainty represents a bias error, which we denote with an over-bar.

$$C_{raw} = \hat{C}_{20,cal} \frac{I - I_{blank}}{I_{standard} - I_{blank}} \tag{3.31}$$

$$\bar{\delta} C_{raw} = \frac{C_{raw}}{C_{20,cal}} \delta \hat{C}_{20,cal} = \frac{C_{raw}}{20ppb} (0.46ppb) = 0.023\, C_{raw} \tag{3.32}$$

3.6.4 Photolysis of Rhodamine WT

RWT is broken down by sunlight at a slower rate than most fluorescent tracers, so that phyotolysis of RWT is not an issue for short dye studies such as the 2002 study, but for the 2003 study it may have been significant. In this section, we present the photolysis model developed by Suijlen and Buyse (1994) and apply it to SP for the 2003 dye study to determine whether decay of the dye due to photolysis was significant.

For long-term experiments with light conditions that do not vary much from day-to-day, the decay of RWT due to photolysis is described by Eq. 3.33. In this equation, $M(t)$ is the RWT mass at time t, M_0 is the initial mass, k is the photolysis coefficient for RWT, $E(t)$ is the total irradiation of the water surface from the beginning of the experiment to time t, and μ is the ratio of surface irradiance to vertically-averaged subsurface downwelling irradiance (the irradiance that passes through the water column).

$$\frac{M(t)}{M_0} = e^{-\mu k E(t)} \tag{3.33}$$

The total irradiation of the water surface, $E(t)$, may be calculated using Eq. 3.34, where the intensity of short-wave radiation, R_{sw}, is taken to represent the scalar irradiance over a broad spectrum – we measured R_{sw} at the weather station near SP throughout the dye studies.

$$E(t) = \int_0^t R_{sw}(t')dt' \tag{3.34}$$

Suijlen and Buyse (1994) found that $k = 3.5 \times 10^{-9} m^2/J$ for RWT. The coefficient μ depends on the water depth, H, and the light extinction coefficient, K, according to Eq. 3.35, where γ is the light-transmission factor at the air-water interface – we did not measure γ, but $\gamma \leq 1$, so we may conservatively set $\gamma = 1$ to arrive at an estimate of maximum decay. Following Rueda and Cowen (2005b), we may roughly estimate the light extinction coefficient, K, from secchi depth, s, following Eq. 3.36.

$$\mu = \gamma \frac{1 - e^{-HK}}{HK} \tag{3.35}$$

$$K = \frac{1.7}{s} \tag{3.36}$$

The total irradition of the water surface during the 2003 dye study, beginning at the time of release and ending when the equipment was pulled from the water was measured to be $E(t) = 1.9 \times 10^8 J/m^2$ at the LSB weather station. Estimation of the appropriate depth for this simple model is somewhat subjective – a better photolysis model would account for the spatial distribution of the RWT in time – as it is, we do not have a precise model of this distribution. However, we observed by eye that for the first few days of the experiment, much of the dye resided in SC, a few hundred meters upstream of the dye release site. Since the most

decay occurs in the beginning of the study, we will use this region to estimate water depth and secchi depth. The average depth in SC is $H = 3m$. We are waiting for our collaborators on the Biocomplexity Project to send us secchi depth measurements that were taken in SC during the 2003 experiment, but for now we may make a rough estimate based on measurements in LSB published in Rueda and Cowen (2005b) – LSB is less turbid than SC and SP, so we will estimate a secchi depth of $s = 0.5m$. These parameters, which should be checked, lead to the estimate that 6% of the RWT decayed during the experiment – this is not significant within the experimental uncertainty toward the end of the experiment. However, if we take the maximum secchi depth measured in LSB, $s = 1.5m$, then we arrive at an estimate that 17% of the RWT decayed, and this is significant. We must obtain secchi depth measurements from our coleague and add a photolysis model to the analysis – if we cannot account for the spatial distribution of the dye in a satisfactory way, we should at least consider photolysis in our uncertainty. We have not done this analysis at this point, but plan to do so before publishing the data for the 2003 dye study.

3.6.5 Filling in Missing Data

2003

For the 2003 experiment, we are missing very little data considering the length of the total record – we linearly interpolate to fill in missing data.

2002

In 2002, we are missing $1hr$ of data due to power failure. Compared to the $7hr$ experiment duration, this is a significant amount of time. It appears that by the

time the power failed, the concentration curve had begun to decay exponentially. We expect this type of behavior for a well-mixed system at constant flow rate. Thus, we interpolate the log of the concentration curve to fill in the missing data. Where data is missing, we estimate a precision error of $\tilde{\delta}C(t)$ that begins at $1ppb$ at the beginning of the missing chunk and drops linearly to $0.2ppb$ by the end of it – these are the magnitudes of the intermittent fluctuations that we observe shortly before and after the missing chunk, respectively.

3.6.6 Ensemble Averaging

2003

The final step in processing the concentration data was to take $4min$ ensemble averages, centered on the same time axis used for the ADCP data. The uncertainty due to ensemble averaging is estimated by taking a bootstrap of the ensemble averages with a 95% confidence interval. This uncertainty is rather small, never exceeding $0.07ppb$, which is surprising because it was the largest source of uncertainty for the velocity data. We will assume that this error is correlated over the same time scale as the corresponding error in outflow, $\tau_Q = 12min$, and thus denote the uncertainty $\breve{\delta}C(t)$.

2002

We take $2min$ ensembles of the 2002 concentration data to match the time axis of the ensemble-averaged outflow record. Fluctuations of instantaneous concentration from the ensemble average concentration can be quite high during the 2002 experiment, in contrast to the 2003 experiment – this indicates that in that longer experiment, dye had become more mixed horizontally and vertically before arriving

at the channel. To estimate uncertainty due to non-uniform concentration in the channel, we use the 95% confidence interval of the bootstrapped ensemble average. We will assume that this error is correlated over the autocorrelation time scale of the outflow, $\tau_Q = 12min$, and thus we denote it $\breve{\delta}C$.

3.6.7 Concentration Estimates and Uncertainty

2003

Our final corrected and ensemble averaged estimate of concentration for the 2003 experiment is plotted in Figure 3.36 along with the total instantaneous 95% uncertainty interval. Summarizing the previous sections, four sources of uncertainty affect our concentration estimate to first order: $\bar{\delta}C_{raw}$ – the uncertainty in the raw concentration reading due to calibration error, $\hat{\delta}C_0(t)$ – the ad-hoc uncertainty we have attributed to our ad-hoc model of blank drift, $\hat{\delta}A(t)$ – the ad-hoc uncertainty we have attributed to our ad-hoc model of attenuation, and $\breve{\delta}C(t)$ – the uncertainty due to ensemble averaging. These four sources of uncertainty propagate through Eq. 3.19 to uncertainty in $C(t)$, our estimate of concentration. Eq. 3.37 summarizes the uncertainty in $C(t)$ – $\bar{\delta}C(t)$ represents bias error, $\breve{\delta}C(t)$ represents error that we assume to be correlated over the time scale $\tau_Q = 12min$, and $\hat{\delta}C(t)$ represents an error that we assume to be correlated over the time scale $\tau_C = 1day$. $\delta C(t)$, the total instantaneous uncertainty at time t, is the root sum square of the three uncertainty terms which are correlated over different time scales. These three contributions to the total instantaneous uncertainty are plotted in Figure 3.36.

$$
\begin{aligned}
\bar{\delta}C(t) &= 0.023\, A(t)\, C_{raw}(t) \\
\hat{\delta}C(t) &= \frac{t - t_{cal}}{t_{postcal} - t_{cal}} \sqrt{[A(t)(0.2ppb)]^2 + [0.09(C_{raw}(t) - C_0(t))]^2} \\
\delta C(t) &= \sqrt{\left[\bar{\delta}C(t)\right]^2 + \left[\hat{\delta}C(t)\right]^2 + \left[\breve{\delta}C(t)\right]^2}
\end{aligned} \tag{3.37}
$$

2002

Our final estimate of concentration for the 2002 experiment is plotted in Figure 3.37 along with the total instantaneous 95% uncertainty interval and three contributions to the total uncertainty that are correlated over different time scales. In the 2002 experiment, the biggest sources of uncertainty are the problems with the blank, our failure to cover the 10-AU tubing, the large chunk of missing data, and the fact that during such a short experiment the dye in the channel may not have been well-mixed. These uncertainties are larger than uncertainties due to instrument sensitivity, or even uncertainties in mixing the calibration solution.

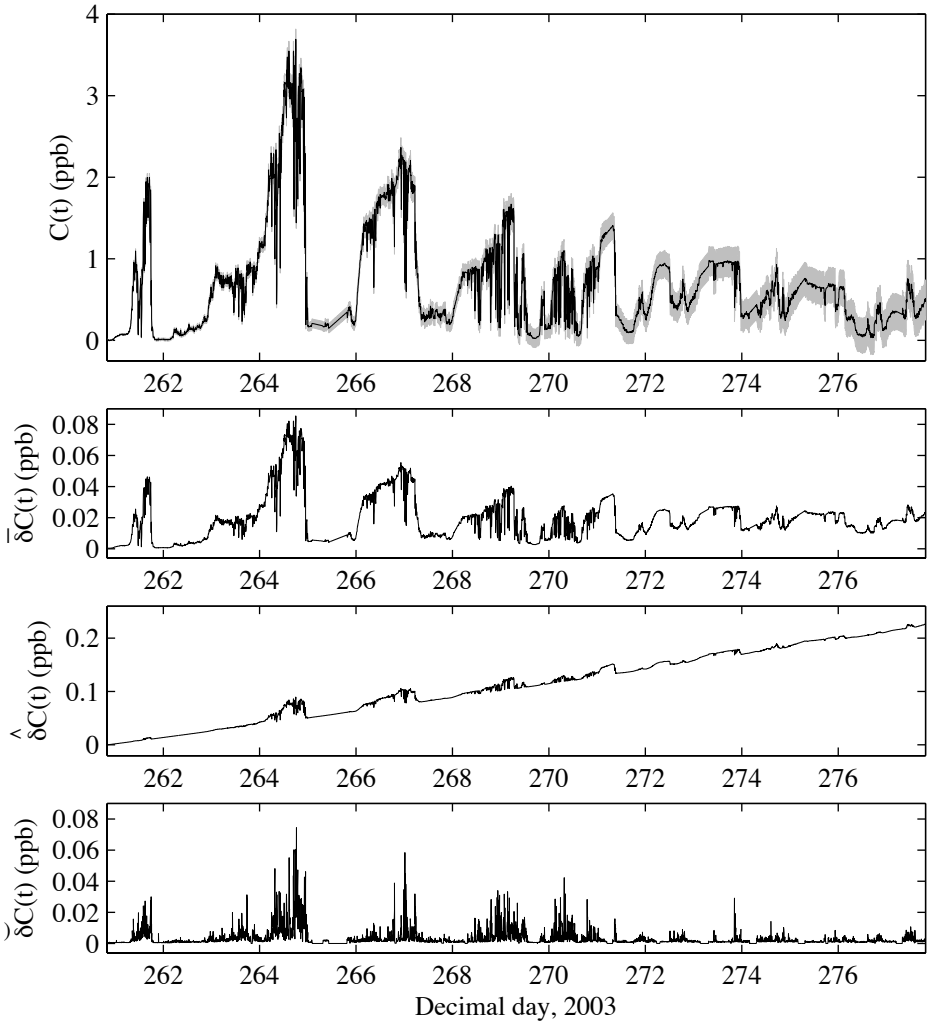

Figure 3.36: Corrected and ensemble averaged concentration data, $C(t)$, for the 2003 dye study along with instantaneous 95% confidence interval (shaded region), and three contributions to total uncertainty: $\overline{\delta}C(t)$ is uncertainty due to bias error in the calibration, $\hat{\delta}C(t)$ is uncertainty due to error in our model of the dirty flow cell that is correlated over time scale $\tau_C = 1day$, and $\breve{\delta}C(t)$ is uncertainty due to ensemble averaging error that is correlated over time scale $\tau_Q = 12min$.

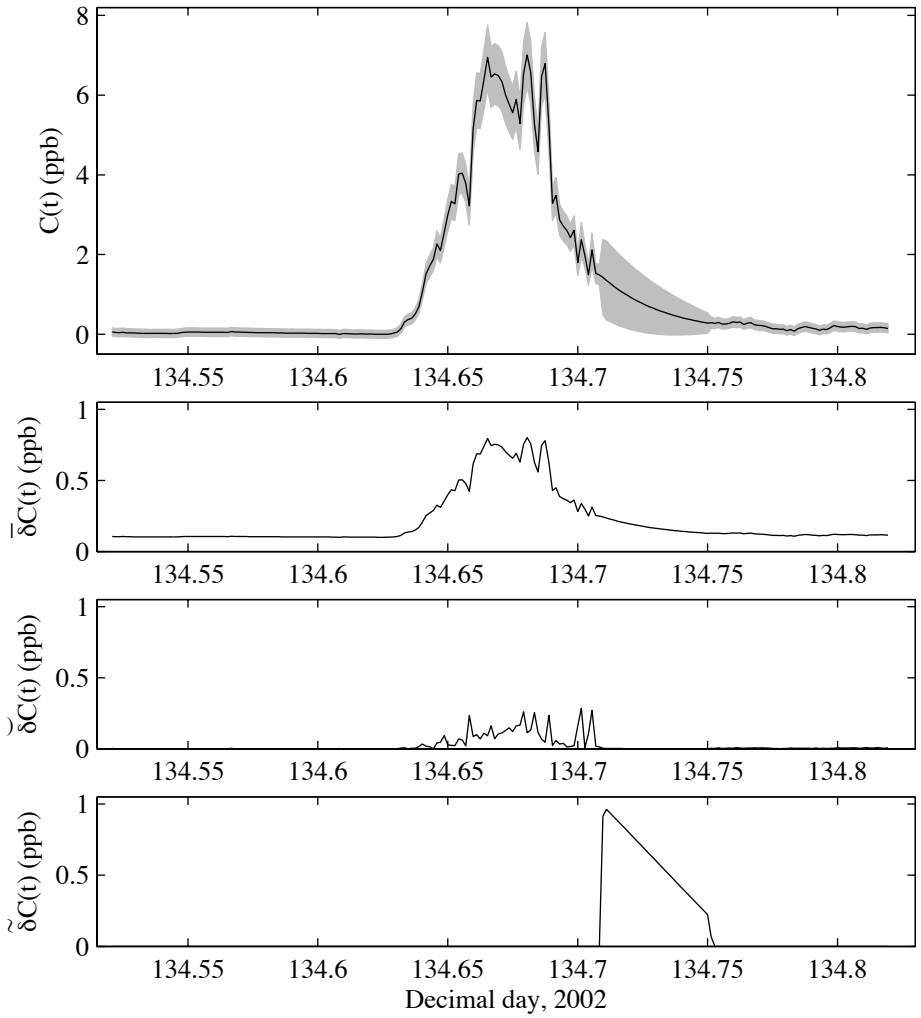

Figure 3.37: Corrected and ensemble averaged concentration data, $C(t)$, for the 2002 dye study along with instantaneous 95% confidence interval (shaded region), and three contributions to total uncertainty: $\overline{\delta}C(t)$ is uncertainty due to bias error in the calibration, $\breve{\delta}C(t)$ is uncertainty due to ensemble averaging error that is correlated over time scale $\tau_Q = 12min$, and $\tilde{\delta}C(t)$ is uncertainty due to precision error.

3.7 Residence Time

3.7.1 Residence Time Distribution

At this point, it is straightforward to compute the RTD, $r(t)$, using Equation 3.38. Errors in $r(t)$ propagate from flow rate, $Q(t)$, concentration, $C(t)$, and the total volume of RWT released in the pond, V_0. We have not yet addressed errors in V_0, and will do so here. The error in V_0 is biased in time, so we will denote the corresponding uncertainty $\bar{\delta}V_0$. For each release, we estimate that only 98% of the dye was released (assuming that the remaining 2% was left in the tubing), and we take 2% of the total volume to be the uncertainty due to bias. We propagate the uncertainties due these three types of errors following Kline and McClintock (1953) as shown in Eq. 3.39.

$$r(t) = \frac{Q(t)C(t)}{V_0} \tag{3.38}$$

$$\begin{aligned}
\bar{\delta}r(t) &= \sqrt{\left[\frac{Q(t)C(t)}{V_0^2}\bar{\delta}V_0\right]^2 + \left[\frac{C(t)}{V_0}\bar{\delta}Q(t)\right]^2 + \left[\frac{Q(t)}{V_0}\bar{\delta}C(t)\right]^2} \\
\hat{\delta}r(t) &= \left|\frac{Q(t)}{V_0}\right|\hat{\delta}C(t) \\
\breve{\delta}r(t) &= \sqrt{\left[\frac{C(t)}{V_0}\breve{\delta}Q(t)\right]^2 + \left[\frac{Q(t)}{V_0}\breve{\delta}C(t)\right]^2} \\
\tilde{\delta}r(t) &= \left|\frac{Q(t)}{V_0}\right|\tilde{\delta}C(t) \\
\delta r(t) &= \sqrt{\left[\bar{\delta}r(t)\right]^2 + \left[\hat{\delta}r(t)\right]^2 + \left[\breve{\delta}r(t)\right]^2 + \left[\tilde{\delta}r(t)\right]^2}
\end{aligned} \tag{3.39}$$

The residence time distributions, $r(t)$, for the two experiments are plotted in Figures 3.38 and 3.39 along with their total instantaneous uncertainties and the various contributions to those uncertainties.

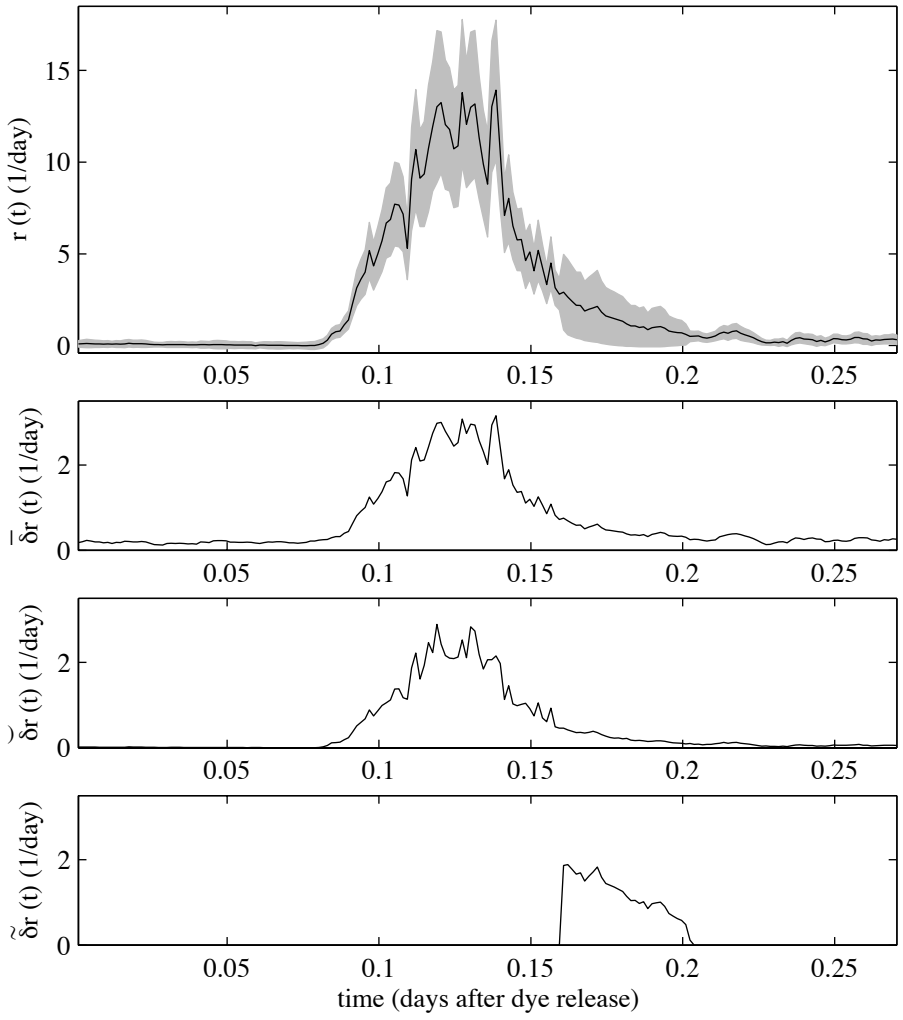

Figure 3.38: RTD, $r(t)$, for the 2002 experiment along with instantaneous 95% confidence interval (shaded area) and three contributions to the total uncertainty that are correlated over different time scales.

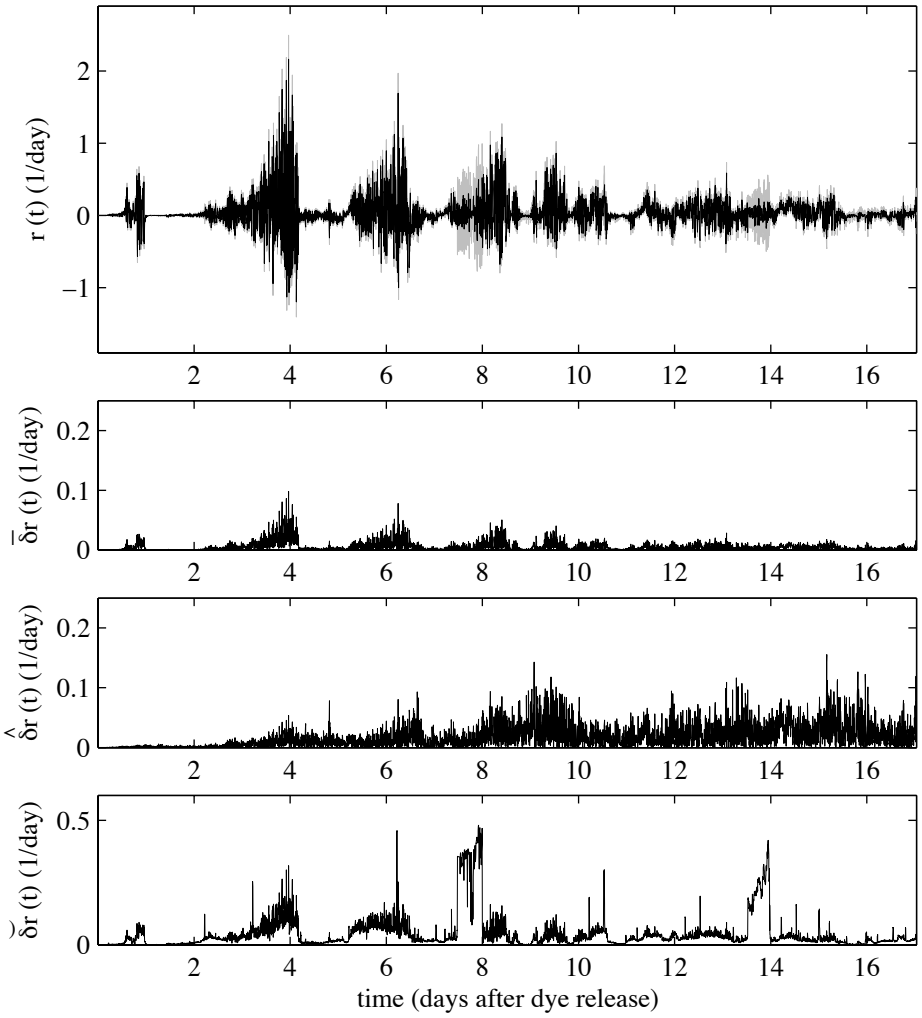

Figure 3.39: $r(t)$ for the 2003 experiment along with instantaneous 95% confidence interval (shaded area) and three contributions to the total uncertainty that are correlated over different time scales. Note that in this case, $r(t)$ is not the RTD because dye re-enters SP, but $r(t)$ does have the same mean as the RTD.

3.7.2 Cumulative Residence Time Distribution

In our dye experiment, we like to say that we measured variables continuously, but at this point in our analysis, we have discrete measurements of flow and transport, $Q(t_i)$ and $C(t_i)$, where $t_i = t_{i-1} + \Delta t$ and Δt is the length of the ensemble averages. From the discrete data, we compute the cumulative residence time distribution, $R(t_k)$, which represents the total mass fraction of tracer which has exited SP at a given time t_k according to Eq. 3.40.

$$R(t_k) \approx \sum_{i=1}^{k} r(t_i)\Delta t \tag{3.40}$$

We have thus far in this analysis carefully separated the uncertainties due to bias error, precision error, and error correlated over time scales $\tau_Q = 12min$ and $\tau_C = 1day$. As shown in Appendix A, these errors propagate differently through time integration. This is the reason we have carefully kept them separate through the whole analysis.

The cumulative residence time distributions, $R(t)$, for the two dye experiments are plotted in Figures 3.40 and 3.41 along with the 95% confidence intervals. The correlation time scale of the various errors was taken into account in computing $\delta R(t)$ as shown in Appendix A.

3.7.3 Extrapolation and Mean Residence Time

It is common in passive tracer studies that an experiment will come to an end before the entire RTD has been obtained. This was the case in both of our experiments. Recall that $R(t)$ represents the fraction of dye that has exited and remains outside SP at time t. When $R(t) = 1$, all the dye has left the pond. In Figures 3.40 and

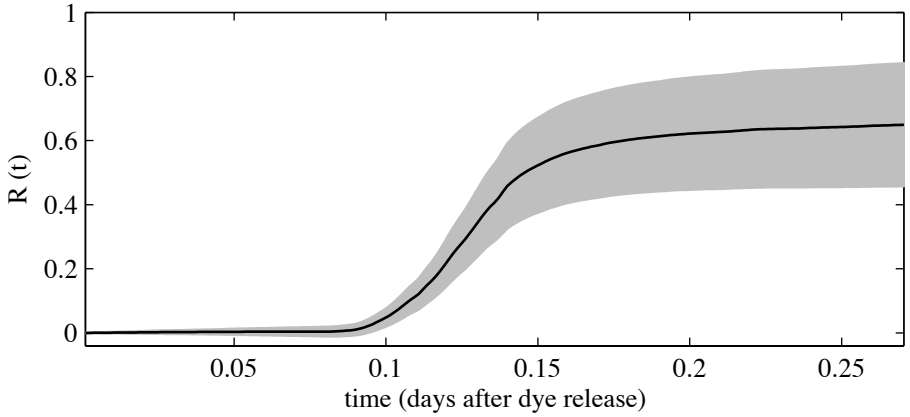

Figure 3.40: CRTD, $R(t)$, with 95% confidence interval for the 2002 dye study.

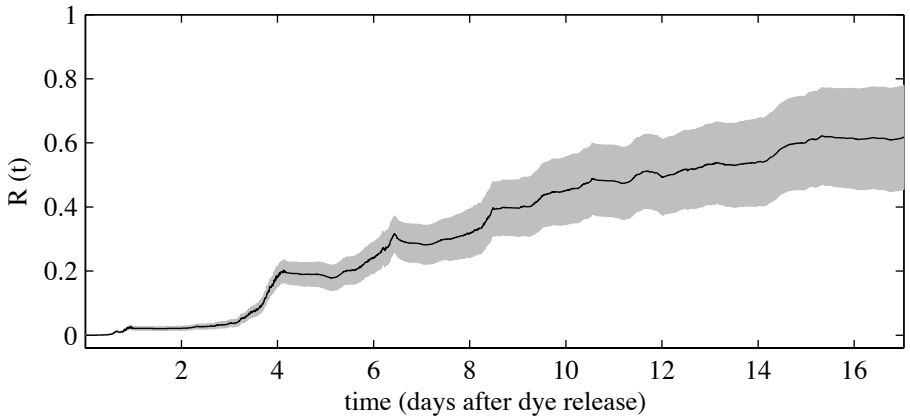

Figure 3.41: $R(t)$ with 95% confidence interval (shaded area) for the 2003 dye study. Note that $R(t)$ is not the CRTD because dye re-enters SP during the 2003 experiment, but $R(t)$ does represent the fraction of dye which has exited and remains outside of SP at time t.

3.41, we see that only 65% of the dye had left the pond by the end of the 2002 experiment and only 62% of the dye had left the pond by the end of the 2003 experiment.

If we are satisfied with these $r(t)$ and $R(t)$ curves as benchmarks for a numerical model of flow through macrophytes, then we need not worry that the entire $r(t)$ curve is not captured during our experiments. However, if we wish to compute statistics of residence time, we cannot do so with an incomplete $r(t)$ – even the mean is highly sensitive to the shape of the $r(t)$ tail. Thus, in order to estimate mean residence times for the dye studies, we must extrapolate the tails of the measured curves. In this section, we discuss our method of extrapolating $r(t)$ and estimating mean residence times. We discuss the 2002 experiment first because $r(t)$ has a simple form and represents the exact RTD.

2002

It is common practice to extrapolate by fitting an exponential tail to the end of residence time distributions (e.g. Rueda and Cowen 2005b). The form of such a tail is given by Eq. 3.41, where r_0 and k are fitting parameters. This extrapolation method is legitimate if the system (in our case SP) has become well-mixed toward the end of the measurements so that a single decay rate can be deciphered from the tail of the measured curve. If the system has, indeed, become well-mixed toward the end of the experiment, then exponential extrapolation of the $r(t)$ tail will result in a corresponding $R(t)$ curve that approaches 1, i.e. all of the dye will leave the system as time approaches infinity.

$$r(t) = r_0 e^{-kt} \tag{3.41}$$

In the case of the 2002 experiment, we can easily fit an exponential curve to the tail, but using the tail to extrapolate results in only 68% of the dye leaving SP at infinite times. This is only 3% more dye than had left before we added a tail. Thus, it is clear that SP was not well-mixed towards the end of the 2002 experiment.

In King, et. al. (2006) (see Appendix B), we have shown that a dead-zone model, crafted after that of Andradóttir and Nepf (2000a,b), explains the 2002 residence time curve very well – both fitting the curve and providing a reasonable explanation of the physics. This model suggests that during periods of high flow, SP is divided into two regions: a "channel" region of high flow where advection and longitudinal dispersion account for tracer transport, and a region of relatively quiescent "dead zones", which communicate with the channel through bulk diffusion. In the first stages of tracer transport, according to the dead-zone model, the time-scales of advection and longitudinal dispersion dominate, but toward the later stages, the time-scale of transfer between the dead-zones and the channel dominates. We believe that the 2002 experiment was terminated during the period of transition between the faster dispersion time scale and the slower bulk-diffusion time scale. The dead-zone model allows us to estimate this later, slower time scale which determines the shape of the RTD tail and thus strongly affects our estimate of mean residence times. We will not discuss the dead-zone model in detail in this thesis, but we note that the best-fit dead-zone model to the 2002 data yields a mean residence time of $0.88 days$, and that other fits which also fall within the uncertainty bounds yield mean residence times between $0.6 days$ and $1.8 days$ – a detailed sensitivity and uncertainty analysis is yet to be performed.

For now, we turn our attention to another method for extrapolating the RTD.

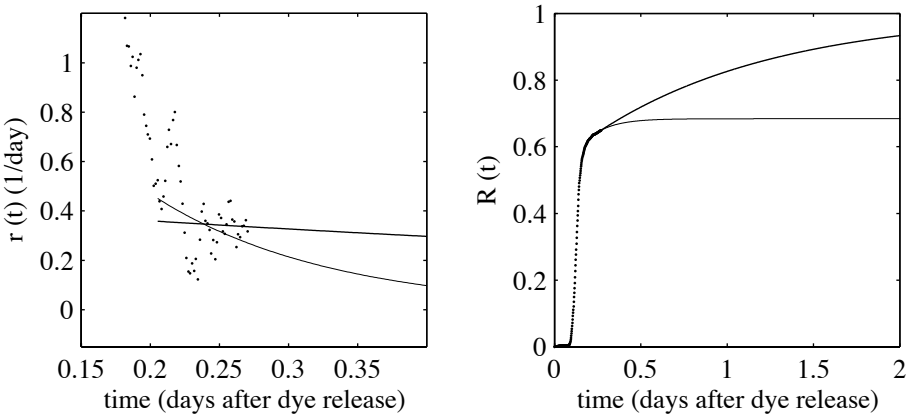

Figure 3.42: Fitting of exponential tails to the RTD and CRTD for the 2002 experiment. The unsuccessful fit of Eq. 3.41 to $r(t)$ and the corresponding $R(t)$ curve are plotted with thin lines; the successful fit of Eq. 3.42 to $R(t)$ and the corresponding $r(t)$ curve are plotted with thick lines.

In this method, we extrapolate the tail of the RTD using an exponential curve as before, but we further impose the condition that all of the dye must eventually exit SP. The exponential model under this constraint is given by Eq. 3.42, where t_N is the time of the final measurement and the decay rate, k, is the only fitting parameter.

$$R(t) = 1 - [1 - R(t_N)]\, e^{-k(t-t_N)} \tag{3.42}$$

We found that it is easier to fit $R(t)$ than $r(t)$, probably because $R(t)$ is more linear towards the end of the experiment. In order to fit a curve to the tail, we must decide what we consider to be the tail. We take all data measured after time $0.204 days$ (days after the dye release) to be the tail – this is the data coming immediately after the large data gap and continuing to the end of the experiment. The fitting of Eq. 3.42 to this tail is shown in Figure 3.42. Using this fit to extrapolate $R(t)$ until over 99% of the dye has left the bay results in a mean residence time estimate of $0.55 days$.

Imposing the condition that all of the tracer leave the system eventually and then fitting an exponential tail to $R(t)$ following Eq. 3.42 results in a model that is valid if SP became well-mixed at the very instant the experiment was terminated. As we have discussed, it is likely that at some point the decay rate of $r(t)$ transitions from being dominated by longitudinal dispersion to being dominated by transfer from dead zones to the main channel – this eventually results in exponential decay to zero. We do not know when this transition takes place – we may have data after the transition but there is not enough to be sure. Extrapolation using Eq. 3.42 assumes that the transition takes place immediately, so it probably gives a low estimate of mean residence times. Nonetheless, we will consider this extrapolation model further by estimating uncertainty in the mean residence time based solely on uncertainty in the measured RTD (i.e. assuming that the extrapolation model is valid, even though it is probably not).

In order to parameterize uncertainty in the mean residence time based upon uncertainty in the data, we compile statistics by sampling from the space of possible $r(t)$ curves, extrapolating according to Eq. 3.42 for each curve, and finally examining statistics of the mean residence times. We sample from the space of possible $r(t)$ curves using MATLAB 6.5's Gaussian random variable generator. In each iteration, we generate a single bias error from a Gaussian random variable having mean 0 and standard deviation $\frac{1}{2}\overline{\delta}r(t)$, a time series of uncorrelated precision errors having mean 0 and standard deviation $\frac{1}{2}\tilde{\delta}r(t)$, and a time series of errors that are correlated over time τ_Q in discrete chunks and uncorrelated between the chunks – the starting time of the first chunk is chosen randomly from the time interval $[0, \tau_Q]$ – this error is sampled from a Gaussian random variable with mean

0 and standard deviation $\frac{1}{2}\breve{\delta}r(t)$[2]. We add the three errors to the expected value of $r(t)$ from our measurement to arrive at a sample of $r(t)$. Next we compute $R(t)$ and perform a fit similar to that shown in Figure 3.42 so we may compute a mean residence time. One mean residence time estimate is generated every iteration. The median, $2.5th$ percentile, and $97.5th$ percentile of the mean residence times are then directly computed to give the expected value and 95% confidence interval. We examined convergence of the these three percentiles with the number of $r(t)$ samples.

Statistics for independent sample sets having different numbers of samples are plotted in Figure 3.43 – we see that all three statistics appear to converge. Also plotted in Figure 3.43 are results for different choices of the "tail" used for fitting. We see that there is not a strong dependence on our choice of tail. Using the tail that begins $0.204days$ after the dye release and a set of 10000 samples of $r(t)$, we estimate a mean residence time of $0.55days$ and a 95% confidence interval of $[0.20days, 3.0days]$. Recall that this interval gives an underestimate of our uncertainty in mean residence time as it does not account for uncertainty in the extrapolation model; however, our best estimate of mean residence time from the dead-zone model does fall on this interval.

2003

For the 2003 experiment, extrapolating with an exponential tail using Eq. 3.41 is especially difficult because the $r(t)$ curve becomes negative, but it is straightforward to extrapolate $R(t)$ using Eq. 3.42, and this is what we do. The resulting

[2]It would be better to chose a realistic autocorrelation function that is not discontinuous (for example an exponential function with decay rate $1/\tau_Q$) for the purpose of stochastic extrapolation, and we hope to do this in the future.

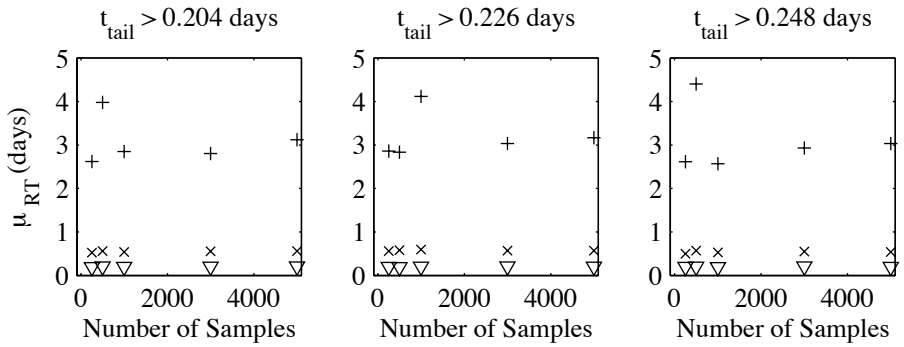

Figure 3.43: Statistics of the mean residence time estimated from different numbers of 2002 $r(t)$ samples to test convergence. The sample sets are independent. Median values of mean residence time are plotted with crosses, the $2.5th$ percentile with triangles, and the $97.5th$ percentile with pluses. These statistics are plotted for each of three tails used to fit the data – the tail is indicated by its starting time at the top of each plot.

extrapolated $R(t)$ curve and the fitted and extrapolated tail of $r(t)$ are plotted in Figure 3.44.

We estimate the mean residence time and the uncertainty in mean residence time due to experimental error (neglecting uncertainty due to the exponential extrapolation method) using the same stochastic method described for the 2002 experiment. Again, we examine convergence (see Figure 3.45) and see that the median, $2.5th$ percentile, and $97.5th$ percentile of the mean residence time appear to converge. We also test tails fitted to data beginning at $8days$ and $11days$, finding that the definition of the tail is slightly more important for the 2003 experiment than it was for the 2002 experiment, especially for the upper bound. Taking $10,000$ samples for the tail beginning on day 11, we estimate a mean residence time of $19days$ with a 95% confidence interval of $[13days, 40days]$. Recall that this confidence interval accounts only for uncertainty in the measured data and does not account for uncertainty in the model used for extrapolation.

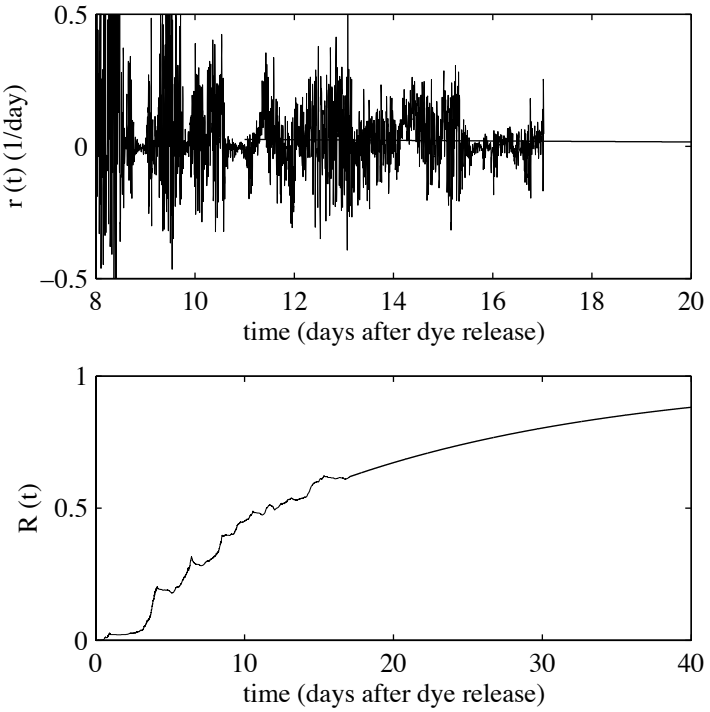

Figure 3.44: Extrapolation of $R(t)$ with an exponential tail for the 2003 experiment. The extrapolated tail is plotted with a thick line and the measured data is plotted with a thin line – the corresponding fitted and extrapolated tail of $r(t)$ is also shown.

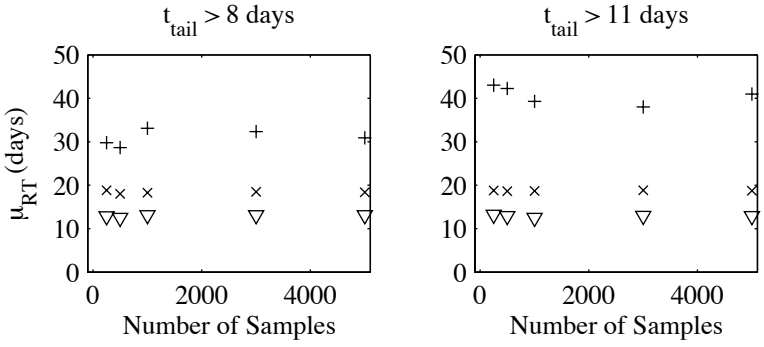

Figure 3.45: Statistics of the mean residence time estimated from different numbers of 2003 $r(t)$ samples to test convergence. The sample sets are independent. Median values of mean residence time are plotted with crosses, the $2.5th$ percentile with triangles, and the $97.5th$ percentile with pluses. These statistics are plotted for each of three tails used to fit the data – the tail is indicated by its starting time at the top of each plot.

Chapter 4

Results and Discussion

In this chapter, we present and discuss the reduced data sets obtained from our two passive tracer release studies. First, we will present the variables that represent the physical environment of SP during the dye studies – these include bathymetry of SP, LO, and SC, flow from SP to LO, water surface elevations in SP, temperature profiles in LO, SP, and SC, meteorological conditions in the vicinity of SP, and macrophyte distributions within SP. Then we will present the measured residence time curves and discuss residence time in context of the physical forcing and response of SP.

4.1 Bathymetry

Recall that bathymetry is plotted in Figure 2.1 – this contour plot was made from the data cited in Section 2.8.1 and processed as described in Section 3.1.

4.2 Results of the 2002 Dye Study

In this section we present the results of the 2002 dye study. For easy reference, measurement sites are mapped in Figure 4.1.

4.2.1 Flow from Sterling Pond to Lake Ontario

The flow rate from SP to LO during and after the 2002 dye study is plotted in Figure 4.2. During the residence time measurements, from days 134.55 through 134.82, the outflow averaged $17 m^3/s$, which is very high for SP – the experiment followed

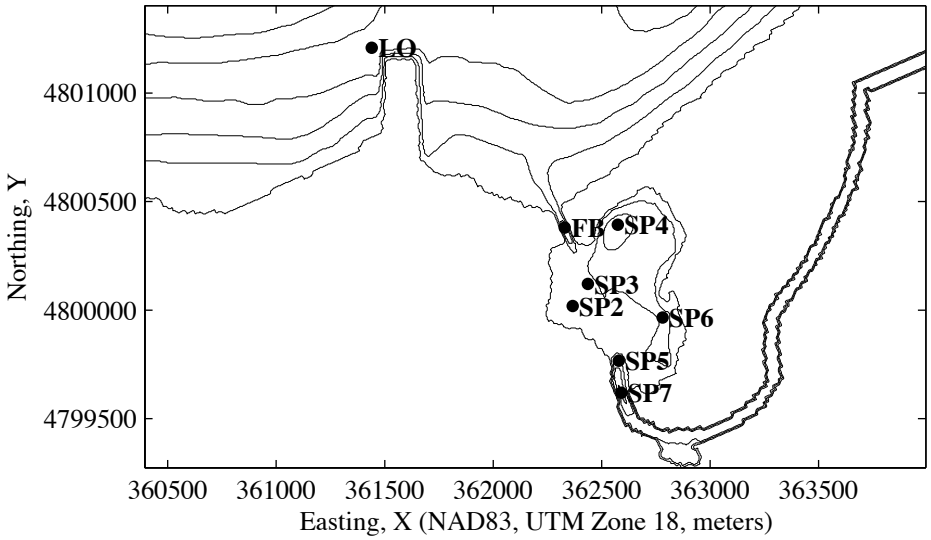

Figure 4.1: Measurement sites for the 2002 dye study. GPS coordinates of these sites are given in Table 2.1.

a period of spring snow melt. During the experiment, the outflow remained fairly constant, oscillating between $10m^3/s$ and $24m^3/s$, but never reversing direction. In summary, the 2002 experiment was conducted during a period when flow was high and as near to steady-state as we have observed in SP. After the residence time measurements had terminated (after day 134.82 – recall only 68% of the mass had left SP at this time), flow remained fairly constant until day 135, when it first began to oscillate with a higher amplitude and then dropped toward zero.

4.2.2 Water Surface Elevation in Sterling Pond

Water surface elevation measured in SP (at site SP5) during and after the 2002 dye study is plotted in Figure 4.3. While absolute water surface elevations are only accurate to about $\pm 10cm$, elevation changes over the course of a few hours are accurate to less than $1cm$. Over the course of a day beginning with the dye release, the water surface elevation dropped by about $5cm$. This drop was most

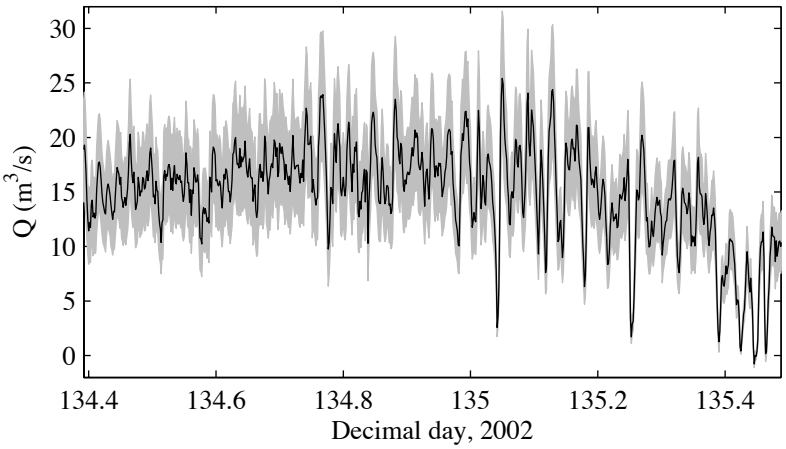

Figure 4.2: Flow rate from SP to LO measured during and after the 2002 dye experiment. Shaded region indicates total instantaneous 95% confidence interval – for a breakdown of the uncertainty into terms correlated over different time scales, see Figure 3.31.

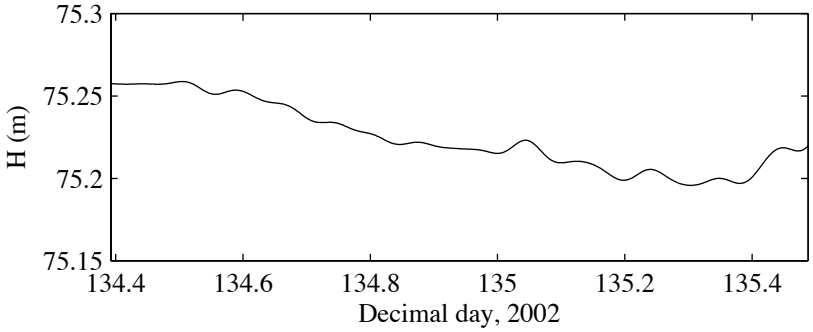

Figure 4.3: Water surface elevation measured in SP during the 2002 dye experiment. The record has been filtered with a $1.5hr$ low-pass Butterworth filter.

likely due both to storage of water in SP that was subsequently drained and to a drop in LO water surface elevations. In Section 3.2, we saw that water surface elevation in SP generally follows that of LO and that $5cm$ is a typical change in water level over the course of one day.

4.2.3 Temperature Profiles

Temperature profiles from LO and SP measured during the 2002 dye study are plotted in Figure 4.4. We see that temperature did not play a significant role in hydrodynamic forcing during the 2002 experiment as temperatures across the SP and LO sites never differ by more than 2^oC. We can see slight differential heating of SP and LO – especially the morning of day 135 in which LO stratifies very slightly and SP warms. We also see very slight stratification (1^oC) in the northeast lobe of the pond (site SP4) toward the end of the residence time measurements (day 134.82) and until the morning of day 135 – this is during a period of high flow, so the fact that the northeast lobe of the pond was able to stratify lends credence to the dead-zone model in which the lobes of the pond are relatively quiescent and advection occurs in a central channel.

4.2.4 Macrophytes

The complete data set for the May 23, 2002 (decimal day 142 – one week after the dye study) macrophyte survey may be found in Appendix C. The data includes total biomass density (dry weight per square area), species composition (percentage of total dry weight), and mean stem length in each of the 41 sampling plots – sampling plot locations are mapped in Figure 2.12.

Here we show a summary of some of the results. Biomass density and plant length are plotted in Figure 4.5, and a brief look at species composition is plotted in Figure 4.6 – densities are plotted in units of $50g/m^2$, which is considered to be on the low end of dense. We see that throughout the southwest portion of the pond, macrophytes were relatively sparse, but dense beds of *Ceratophyllum demersum*, *Elodea sp.*, and *Potamogeton crispus* occupied the northeast portion of the pond,

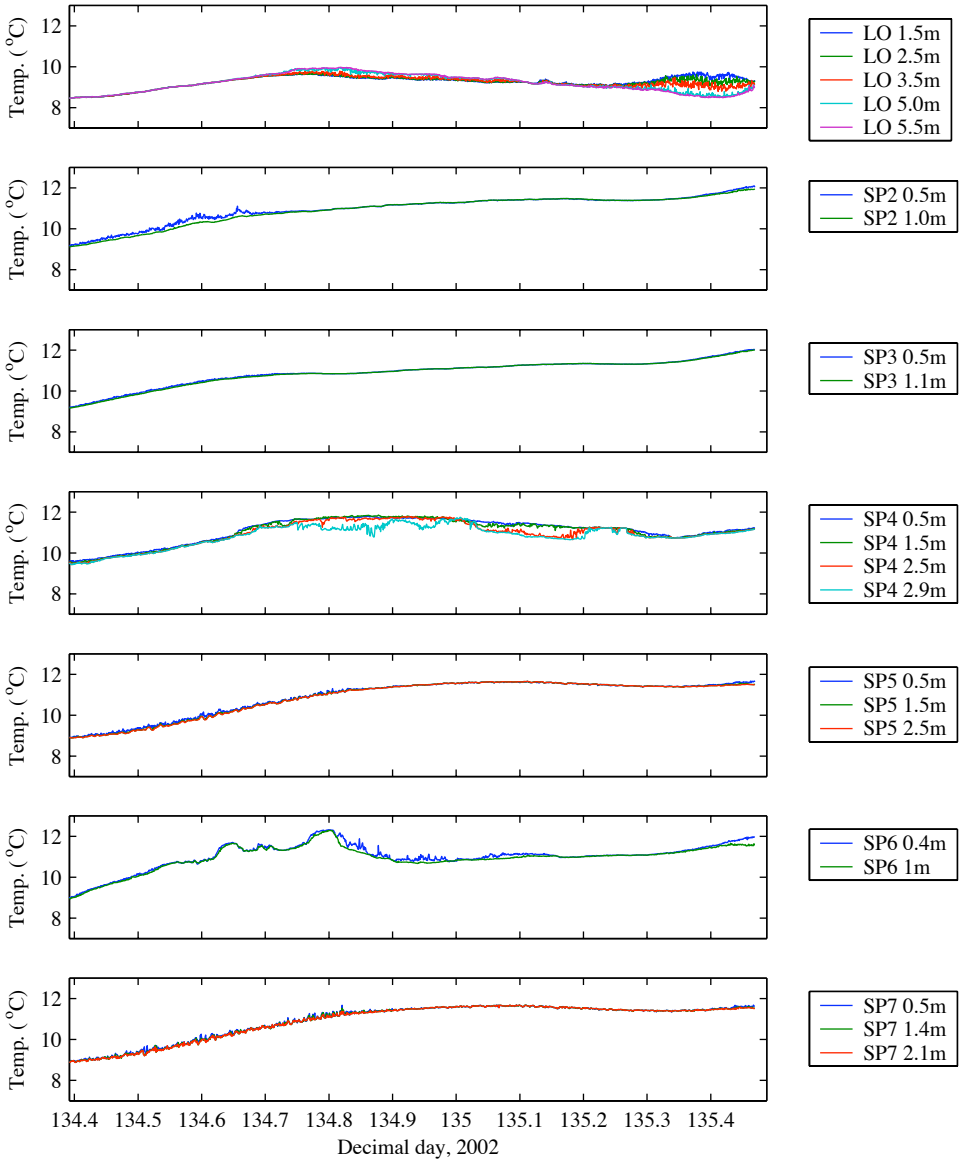

Figure 4.4: Temperature profiles measured in LO and SP during the 2002 dye study. Measurement sites and thermistor depths (distances below the surface) are indicated in the legend – the locations of these measurement sites are plotted in Figure 4.1 and their GPS coordinates are given in Table 2.5.

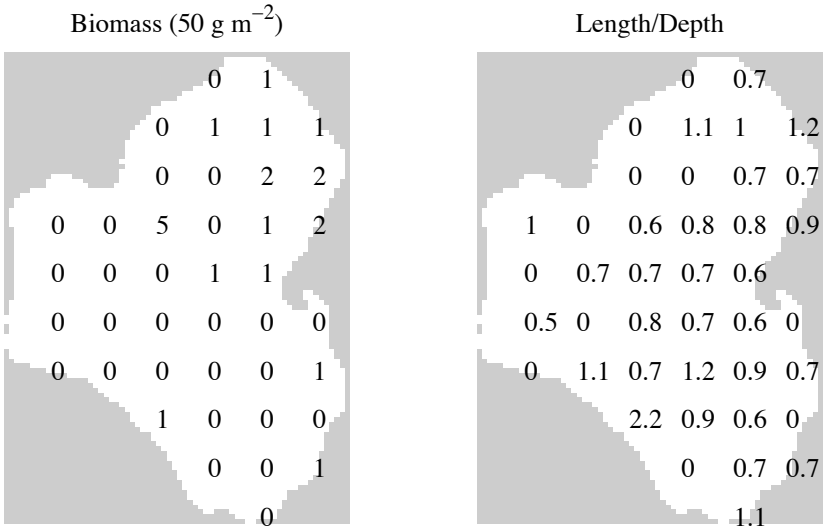

Figure 4.5: Some results of the 2002 macrophyte survey. Biomass density (units are $50g$ dry weight per m^2) and mean stem length (normalized by water depth) are plotted here.

and a patch of $250g/m^2$ occupied the east side of the channel entrance. We would expect this macrophyte distribution to reinforce the dead-zone-like behavior of the northeast lobe of the pond.

Since by eye there appeared to be be few macrophytes in SP when we conducted the 2002 dye experiment, we were hoping that this experiment could serve as a benchmark for a numerical model that does not include macrophytes, and that the 2003 experiment could complement the 2002 experiment as the with-macrophyte case – the macrophyte survey data, however suggests that macrophytes may have to be considered for the 2002 experiment as well.

4.2.5 Meteorological Data

Meteorological data collected during the 2002 dye experiment is plotted in Figure 4.7. This is raw data from the meteorological station located on the east shore of LSB (see Figure 2.14). It includes atmospheric pressure (P_a), air temperature (T_a),

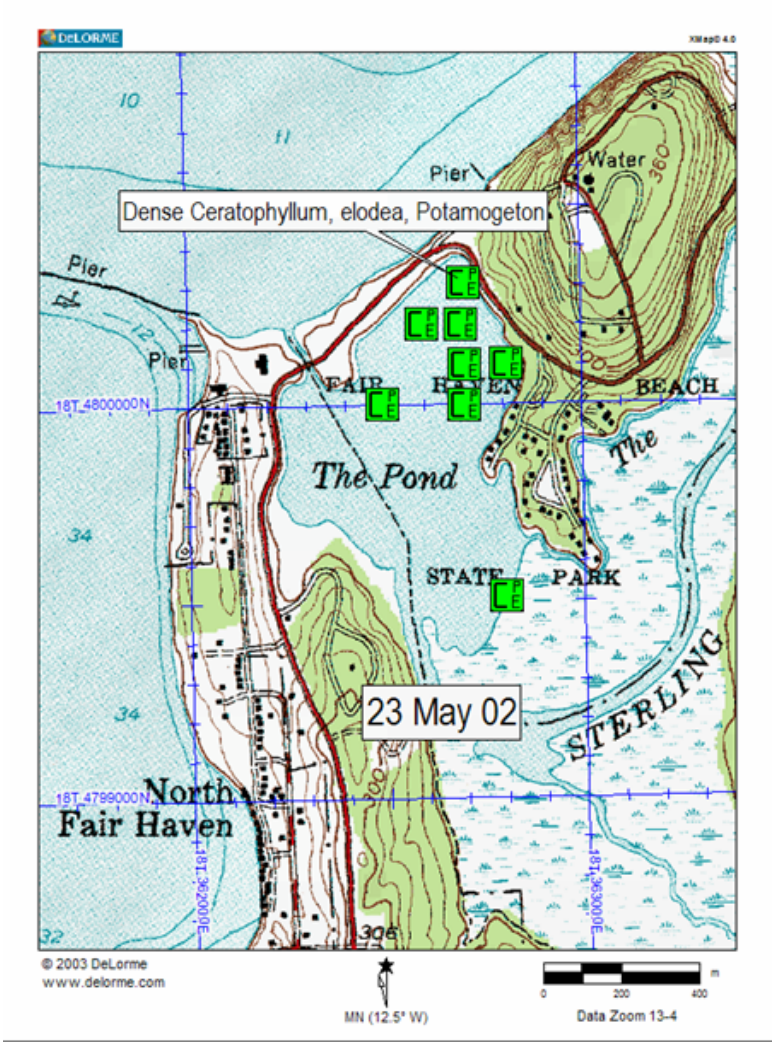

Figure 4.6: Cartoon showing species composition during the May 23, 2002 macrophyte survey. Plots are labeled if they contain over $50 g/m^2$ dry weight of *Ceratophyllum demersum*, *Elodea sp.*, and/or *Potamogeton crispus*. Used with permission of Robert Johnson.

relative humidity (R.H.), shortwave radiation (R_{sw}), and wind velocity (U_w and V_w are the components pointing toward true east and true north, respectively). A description of the weather station and its components along with estimates of measurement error may be found in Section 2.8.2.

Comparing air temperatures to water temperatures, we see that both SP and LO water temperatures were very close to the air temperature during the 2002 experiment. We also note the high westerly wind blowing across SP during the dye study. This wind was noticed in the field, and some dye was observed by eye to blow into the southeast corner of SP shortly after the release.

4.2.6 Residence Time Distribution

Recall that the dye release took place at time 134.55 (see Table 2.4). The RTD, $r(t)$, for the 2002 experiment is plotted in Figure 4.8. As there is no return-flow of RWT into SP, $r(t)$ represents the true RTD.

The RTD is useful as a benchmark for numerical modeling of the 2002 dye experiment, and for this purpose we need not estimate mean residence time. For the Biocomplexity Project, however, we would like to do so. Because only 65% of the dye left the bay during the experiment, this requires extrapolation of the RTD – the extrapolation method is explained in Section 3.7.3. The mean residence time is thus estimated to be $0.55 days$ and the 95% confidence interval for the mean residence time is estimated from the experimental uncertainty to be between $0.20 days$ and $3.0 days$. Note that this uncertainty interval neglects error incurred by extrapolating the measured RTD.

As discussed in Appendix B, a dead-zone model successfully explains the shape of the 2002 RTD. This model accounts for advection and longitudinal dispersion

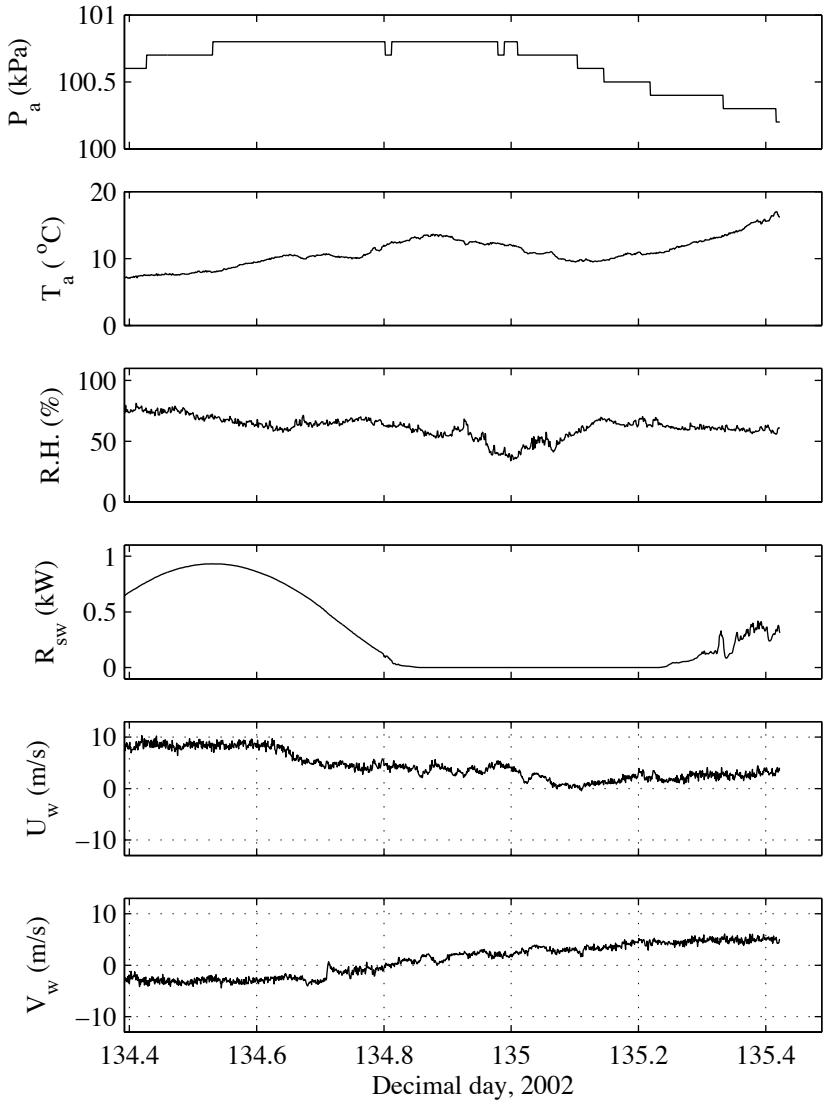

Figure 4.7: Meteorological data measured during the 2002 dye study at the LSB weather station.

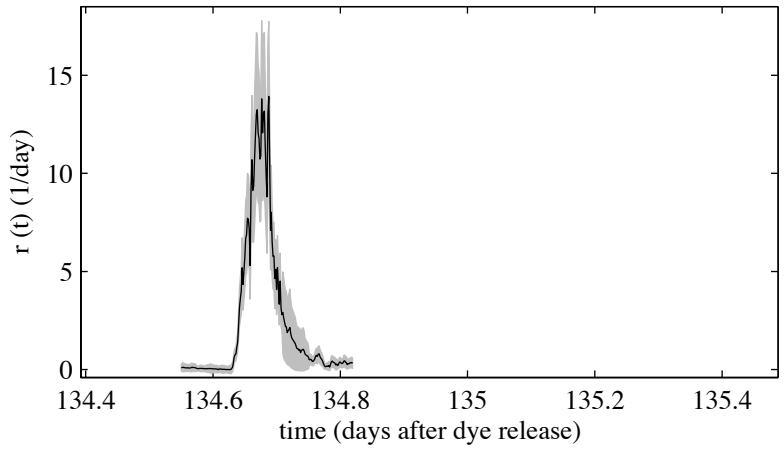

Figure 4.8: RTD measured during the 2002 dye experiment. Shaded region indicates total instantaneous 95% confidence interval – for a breakdown of the uncertainty into terms correlated over different time scales, see Figure 3.38.

in a channelized section of the pond and diffusive exchange between this "channel" and near-quiescent "dead-zones". In the solution of the dead-zone model for the 2002 experiment, the RTD is similar to the solution of the 1-D advection-dispersion equation (see for example Fischer, et. al. 1979) except that the dead-zone model solution has a long tail resulting from storage and subsequent release by the dead zones. We may expect to see this type of RTD in SP during periods of high runoff and weak forcing from LO. The low macrophyte densities in the center of SP and high densities in the northeast lobe most likely reinforce this behavior. Conversely, the macrophyte distribution is probably promoted by the dead-zone/channel distinction, as macrophytes grow more readily in quiescent water.

4.3 Results of the 2003 Dye Study

In this section we present the results of the 2003 dye study. For easy reference, measurement sites are mapped in Figure 4.9.

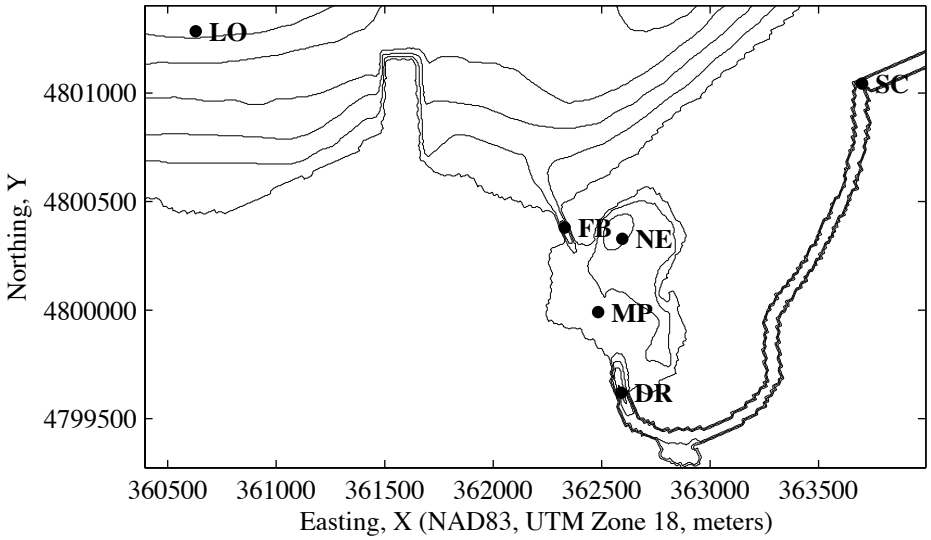

Figure 4.9: Measurement sites for the 2003 dye study. GPS coordinates of these sites are given in Table 2.2.

4.3.1 Flow from Sterling Pond to Lake Ontario

The title of this section is somewhat a misnomer – while flow during the 2003 dye study was on average from SP to LO, flow reversals occurred frequently so that flow was often from LO to SP. The outflow time series is plotted in Figure 4.10. Flow is low to moderate throughout the dye study and reversals occur on average every $10 - 15min$. The vertical velocity profile measured in the center of the channel connecting SP to LO is also plotted in this figure, and we will discuss it later on.

4.3.2 Water Surface Elevation in Sterling Pond

Water surface elevation measured in SP (at site DR) during and after the 2003 dye study is plotted in Figure 4.11. The fluctuations in LO water levels – which SP water levels follow closely (see Section 3.2) appear to be the primary driving force

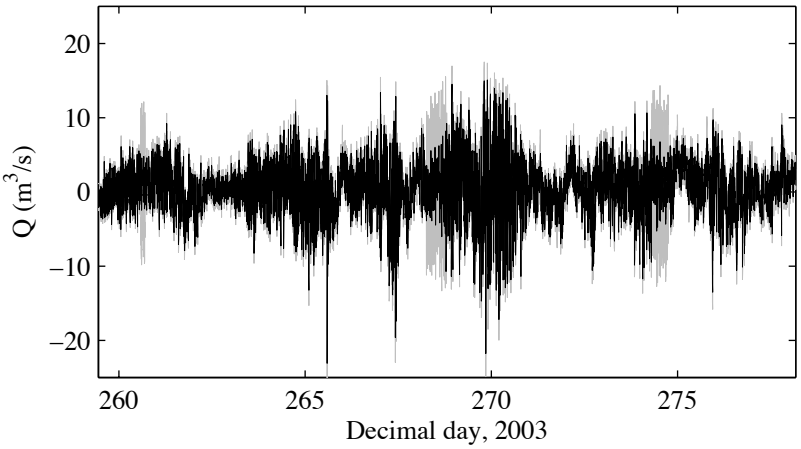

Figure 4.10: Flow rate from SP to LO measured during the 2003 dye experiment. Shaded region indicates total instantaneous 95% confidence interval – for a breakdown of the uncertainty into terms correlated over different time scales, see Figure 3.28.

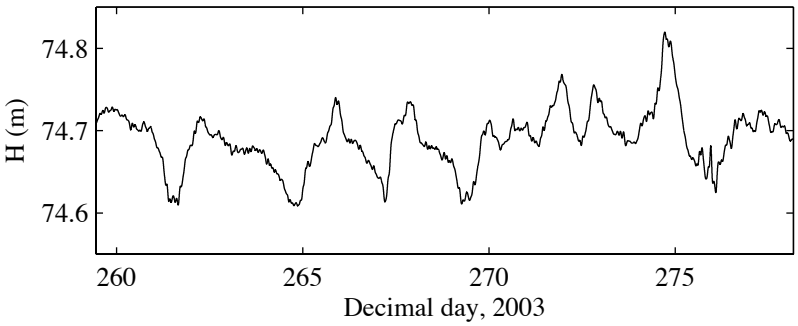

Figure 4.11: Water surface elevation measured in SP during the 2003 dye experiment. The record has been filtered with a $1.5hr$ low-pass Butterworth filter.

behind the oscillatory flow observed in the channel connecting SP to LO, and thus the dominant mechanism of exchange between SP and LO.

4.3.3 Temperature Profiles

Temperature profiles from the 2003 experiment are plotted in Figure 4.12. Coastal upwelling of Lake Ontario may be observed in the LO data roughly between days 260 and 266. LO hypolymnetic water appears to be present in the channel connecting LO to SP on days 262 and between days 265 and 266. It appears that

some of this water remained permanently in SP – notably at the bottom of the northeast lobe (site NE).

The velocity profile measured in the center of the channel connecting SP to LO is plotted in Figure 4.13. The velocity profile, $U(z)$, has been averaged over $6hr$ time windows so that stratified exchange flow is visible during the upwelling event. We see that two-layer exchange flow rarely took place in the channel connecting LO to SP, even though LO hypolymnetic water was clearly present in the channel for sustained periods of time (see Figure 4.12).

4.3.4 Macrophytes

The complete data set for the September 25, 2003 (decimal day 267) macrophyte survey may be found in Appendix C. The data includes total biomass density (dry weight per square area), and species composition (percentage of total dry weight)[1] in each of the 41 sampling plots – plot locations are mapped in Figure 2.12.

Here we show a summary of some of the results. Biomass density is plotted in Figure 4.14, and a brief look at species composition is plotted in Figure 4.15. In summary, biomass was extremely dense during the 2003 experiment, such that it was very difficult to get a boat across SP to deploy and retrieve the field equipment. Thus, we expect that the macrophytes strongly affected the bulk flow and transport through SP during this experiment. We do note that considering other surveys of SP (for example a survey conducted in August of 2002, not included in this thesis but available from Robert Johnson's group), macrophytes during the 2003 dye experiment were relatively uniform in density.

The presence of *Nitellopsis obtusa* in SP is interesting from an ecological stand-

[1]Mean stem length data should soon be available as well.

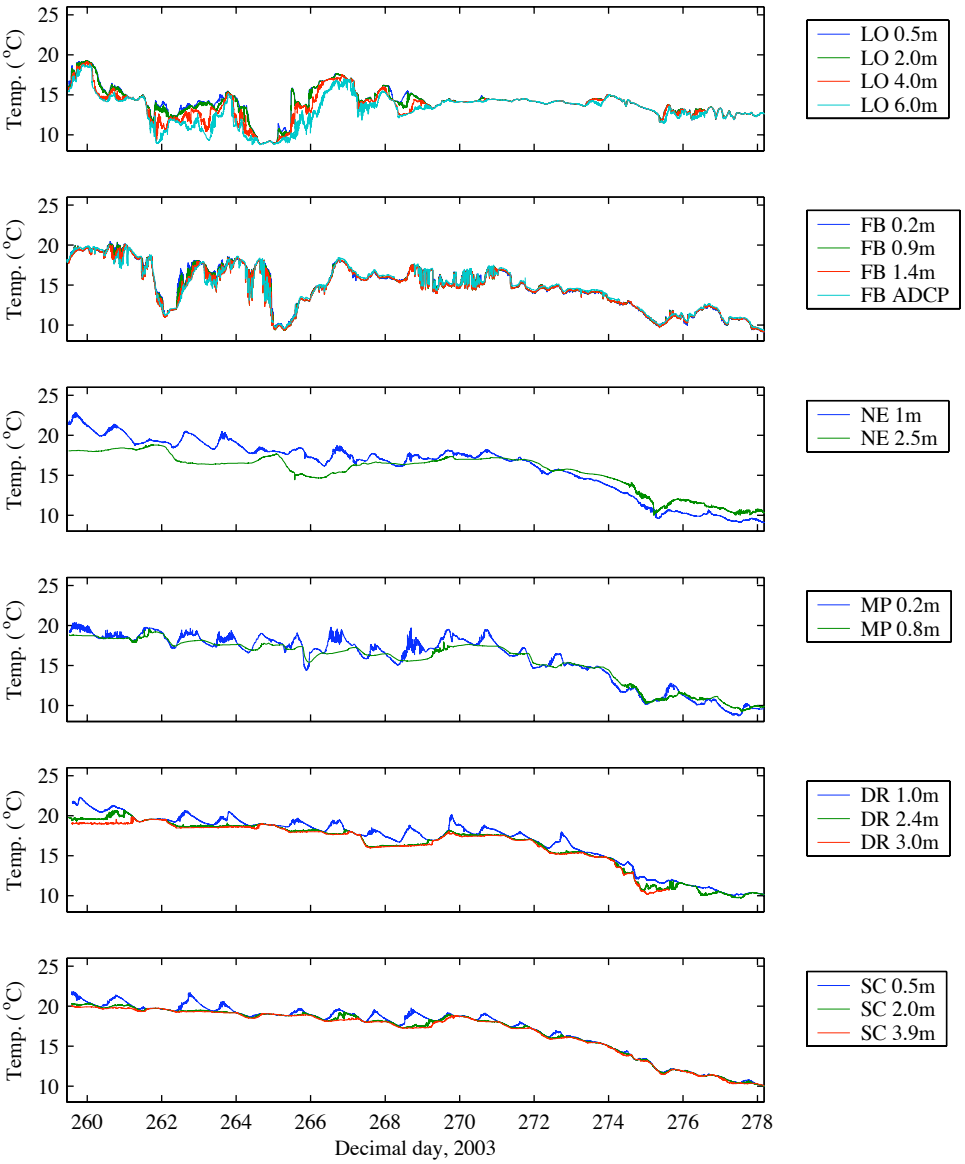

Figure 4.12: Temperature profiles measured in LO, SP, and SC during the 2003 dye study. Measurement sites and thermistor depths (distances below the surface) are indicated in the legend – the locations of these measurement sites are plotted in Figure 4.9 and their GPS coordinates are given in Table 2.6. Note that the time series labeled "FB ADCP" (not in the table) is from the $1200kHz ADCP$ located at the bottom center of the channel connecting SP to LO ($3m$ depth) while the other FB records are from the west side of the channel and measured by more accurate thermistors.

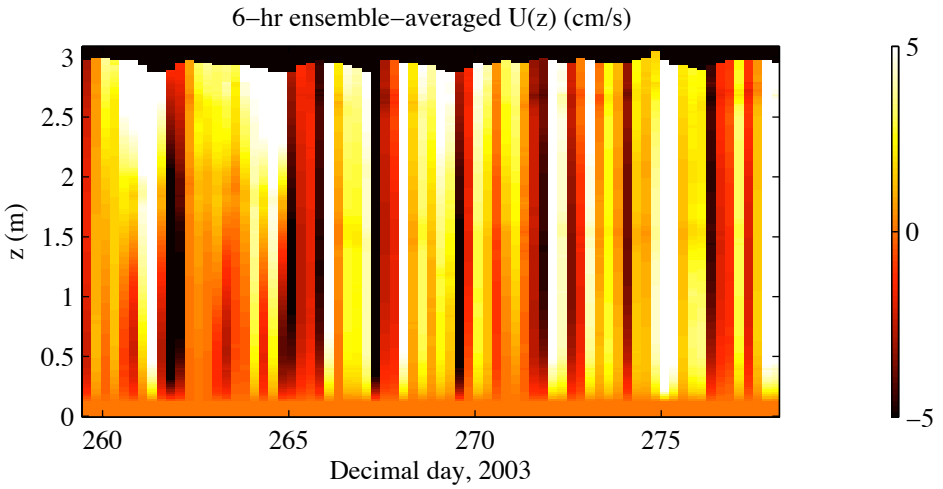

Figure 4.13: Vertical velocity profile measured in the channel connecting SP to LO during the 2003 dye study. $U(z)$ is the long-channel component of velocity averaged over $6hr$ time windows.

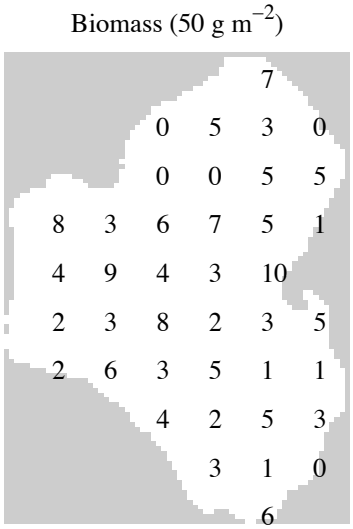

Figure 4.14: Some results of the 2003 macrophyte survey – biomass density (units are $50g$ dry weight per m^2).

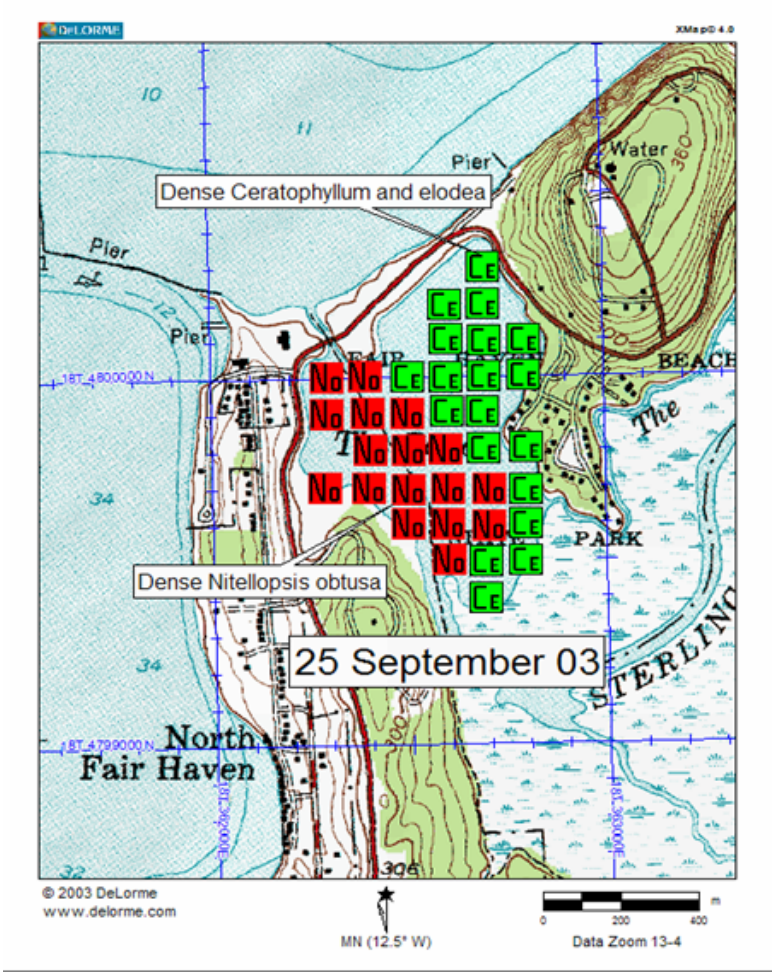

Figure 4.15: Cartoon showing species composition during the September 25, 2003 macrophyte survey. Plots are labeled if they contain over $50 g/m^2$ dry weight of the labeled species – *Ce* indicates *Ceratophyllum demersum* and *Elodea sp.*, and *No* indicates *Nitellopsis obtusa*. Used with permission of Robert Johnson.

point. This species is an invasive macro-algae which is classified as an endangered species in both Japan and Great Britain. It was first found in SP by the Johnson group in 2002, but not identified until 2003 as it is a rare species in the NY region. During 2003 it took over the southwest half of SP, as can be seen in Figure 4.15.

4.3.5 Meteorological Data

Meteorological data collected during the 2003 dye experiment is plotted in Figure 4.16.

4.3.6 Residence Time Distribution

Recall that the dye release took place at time 260.78 (see Table 2.4). It is important to keep in mind, as discussed in Section 2.2.1, that the residence time distribution (RTD) represents water entering Sterling Pond from Sterling Creek at the time of the dye release, and that the measured RTD only represents this inasmuch as the dye acted as a passive and conservative tracer[2]. It is also important to keep in mind, as discussed in Section 1.2, that what we call the "RTD" is not really a probability distribution in cases where there is return flow through the channel emptying SP into LO (such as during this 2003 experiment), but that the true RTD and our quantity $r(t)$ share the same mean. The $r(t)$ curve for the 2003 experiment is plotted in Figure 4.17.

This curve is useful as a benchmark for numerical modeling of the 2003 dye experiments, and for this purpose we need not estimate mean residence time. For the Biocomplexity Project, however, we would like to do so. Because only 62%

[2]In the 2003 experiment, we did not dilute the 20% solution of Rhodamine WT, so the solution had a specific gravity of about 1.15.

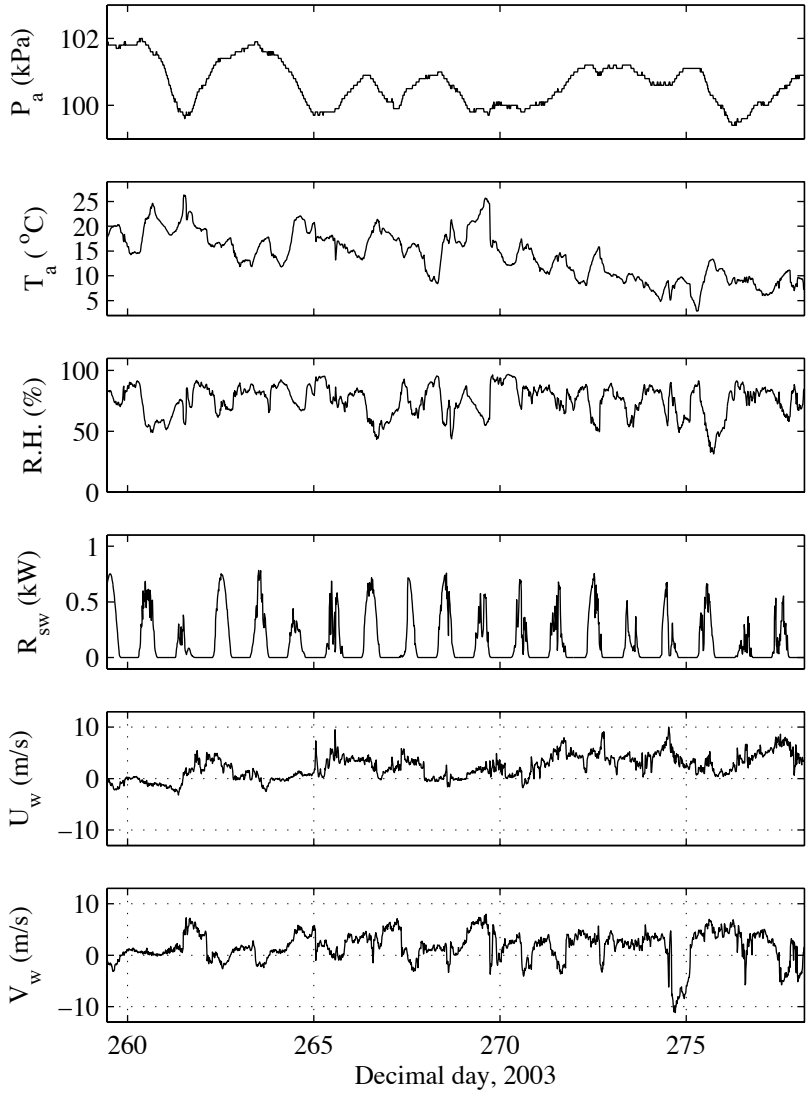

Figure 4.16: Meteorological data measured during the 2003 dye study at the LSB weather station.

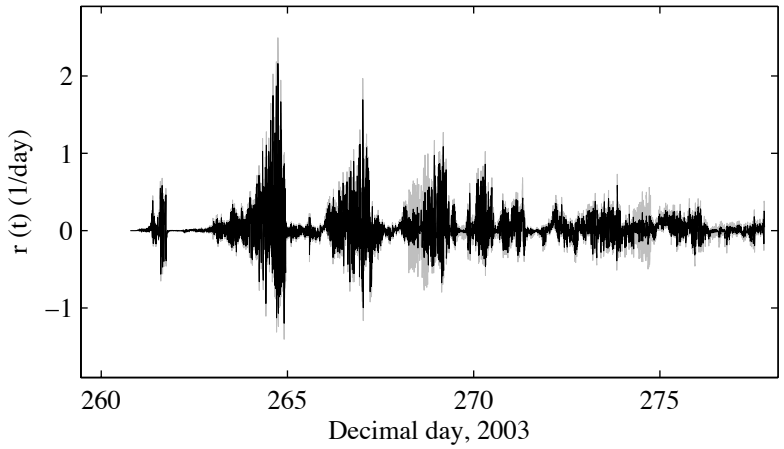

Figure 4.17: The normalized RWT flux from SP to LO, $r(t)$, measured during the 2003 dye experiment. Shaded region indicates total instantaneous 95% confidence interval – for a breakdown of the uncertainty into terms correlated over different time scales, see Figure 3.39.

of the dye leaves the bay during the experiment, this requires extrapolation of $r(t)$ – the extrapolation method is explained in Section 3.7.3. The mean residence time is thus estimated to be $19 days$, and the 95% confidence interval for the mean residence time is estimated from the experimental uncertainty to be between $13 days$ and $40 days$. Note that this uncertainty interval neglects error incurred by extrapolating the measured $r(t)$ curve.

We caution that photolysis of RWT has not been accounted for in the 2003 study, but that it may have decreased concentrations as much as 17% by the end of the study – as decay is exponential and depends on water depth and clarity, the propagation of this error to mean residence time estimates is not straightforward. It is more likely that the decay was closer to 6%, which should not affect our estimates of mean residence time much, but we will closely consider this issue in the near future.

4.4 Other Discussions of General Interest

4.4.1 The Importance of Horizontal Boundary Layers in Narrow Channels

In this section we discuss the broader significance of our horizontal boundary layer measurement in the the channel. As we saw in section 3.3.7, measuring velocity in a vertical profile gives us much more information than measuring velocity at a point, at least in a highly unsteady channel, because the velocity varies in the vertical direction in a way that is only very roughly predictable. Likewise, we saw in section 3.4 that the variation of the velocity across the channel can be significant. We decided to conduct the horizontal boundary layer experiment because our modeling studies suggested that we were under-predicting outflow, and we hypothesized that the horizontal boundary layers were to blame. We found that the horizontal boundary layers on average reduce the bulk velocity through the upper portion of the channel by 14%. In this section we will compare this to the reduction we might expect to find using pre-existing knowledge about channel flow.

We wish to predict the ratio $\overline{U}/U_0$ where $\overline{U}$ is the bulk velocity defined by equation 3.10 and $U_0 \equiv U(y = d)$ is the centerline velocity. We would like to know if this ratio depends on the width of the channel. It turns out that the appropriate dependent variable is the centerline Reynolds number, $Re_0 \equiv U_0 d/\nu$, where ν is the kinematic viscosity. Let us assume that the channel is infinitely deep, that flow is statistically stationary, and that the log law extends all the way from the wall to the channel centerline. None of these assumptions hold in the SP channel, but we may make first order estimates by making these assumptions. Following Pope (2000, Chapter 7), we may expect that the ratio between the bulk velocity

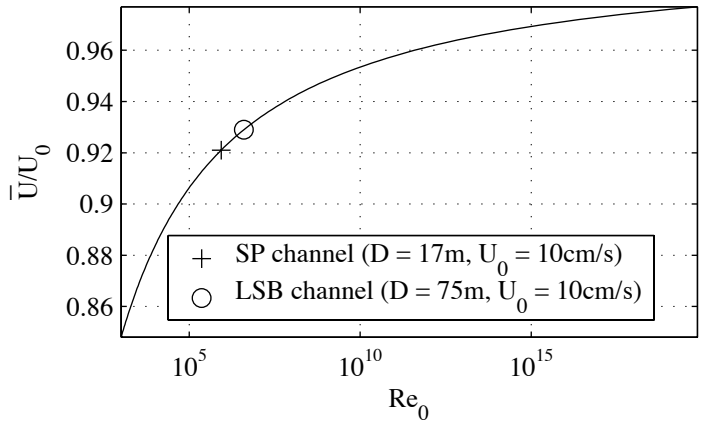

Figure 4.18: Ratio of bulk and centerline velocities as a function of centerline Reynolds number, as predicted for an infinitely deep channel by equation 4.1. Predictions for typical values of the centerline Reynolds number seen in the SP and LSB channels are plotted as well.

and the centerline velocity depends on the centerline Reynolds number as shown in 4.1, with constants $\kappa = 0.41$, $B = 5.2$, and $B_1 = 0.7$. This relationship is plotted explicitly in figure 4.18 along with the typical positions of the SP and LSB channels on the curve. We see that if the SP channel were infinitely deep and the flow were statistically stationary, we would expect the bulk velocities to be roughly 8% lower than the centerline velocities we measured with the ADCP. Because it was necessary to make so many invalid assumptions to come to this estimate, we performed the horizontal boundary layer experiment described in Section 2.5.3, and found in Section 3.4 that the velocity deficit due to the boundary layers can be as much as 50% higher in a real channel.

$$\left(1 - \frac{\overline{U}}{U_0}\right)^{-1} = \ln\left[\kappa Re_0 \left(1 - \frac{\overline{U}}{U_0}\right)\right] + \kappa(B + B_1) \tag{4.1}$$

4.4.2 Recommended Maintenance for Making Long-Term Measurements with a Flow-Through Fluorometer

From the 2003 dye experiment, we gained a great deal of knowledge about operating a flow-through fluorometer in the field for weeks at a time. We recommend the following procedure to anyone conducting a long-term RWT release experiment and monitoring with a flow-through fluorometer, especially in water where plant matter or sediment is present. Perform this procedure every few days, or more often if large amounts of plant matter or sediment are present in the water.

1. Stop the fluorometer, and pull it out of the water.

2. Perform a post-calibration. That is, observe the concentration reading for a known blank and standard, but do not alter the fluorometer settings.

3. After the post-calibration, run a soultion of diluted bleach through the fluorometer until the concentration reading is zero. In our experience, this will clean out the flow cell; if the fluorometer reading does not reach zero, manual cleaning may be necessary.

4. Thoroughly wash away the bleach solution (which reacts with RWT) by flushing the fluorometer with plain water several times. Make sure to dispose of the bleach solution far from the field site.

5. If the fluorometer is not as stable as the 10-AU, perform another post-calibration.

6. After the post-calibration(s) and cleaning, return the fluorometer to its regular operations.

Chapter 5

Conclusions

5.1 Residence Time Scales in Sterling Pond

In two passive tracer release studies, we have directly measured the mean residence time of water entering SP from its watershed through SC. We conducted the experiments under different environmental conditions, hoping to sample different extremes of the residence times characterizing SP.

During the 2002 experiment, which took place in mid-May after a snow-melt event, flow from SC through SP to LO was high, macrophyte populations were relatively sparse, and the macrophytes that were present tended to intensify flow from SC to LO by defining a channel through the middle of the pond. In this experiment we measured a mean residence time of $\mu_{RT} = 0.55 days$ with a 95% confidence interval between $0.20 days$ and $3.0 days$. This confidence interval does not account for uncertainty in our model for extrapolating the residence time distribution, which only accounted for 65% of the dye. Our extrapolation method is biased towards low mean residence time estimates, as it assumes that the pond becomes instantaneously well-mixed as soon as we terminate the experiment. In King, et. al. (2006), we explore the use of a physically-based dead-zone model for fitting and extrapolating the RTD. We find that the best-fit model gives an estimate of mean residence time of $\mu_{RT} = 0.88 days$, and that by the end of the dye experiment, SP may, indeed, have been near to well-mixed. However, mean residence time estimates from the dead-zone model vary widely for different models that fall within the experimental uncertainty, and we are yet to do an detailed uncertainty analysis.

The 2003 experiment took place during a dry year with low flow from the SP watershed. SP was populated by a thick, emergent bed of macrophytes that was fairly uniform in density across the pond for the duration of this study. LO was fairly active – strong wind-induced barotropic oscillations were the dominant forcing mechanism for exchange between SP and LO. Weak coastal upwelling of LO occurred during the 2003 experiment, and LO hypolymnetic water entered SP, though the mechanism of exchange still appears to be a combination of barotropic forcing and turbulent mixing, as very little exchange flow was observed in the channel connecting SP to LO, but some LO water appears to have remained in SP, notably at the bottom of the northeast lobe. In the 2003 experiment, we measured a mean residence time of $19 days$ with a 95% confidence interval between $13 days$ and $40 days$. This confidence interval does not account for uncertainty in our model for extrapolating the residence time distribution, which in this case accounted for only 62% of the dye. These estimates do not account for photolysis of RWT, which may have reduced dye concentrations by as much as 17% during the 2003 study, though a reduction of 6% is more likely. Photolysis depends on water depth and water clarity – we will obtain secchi depth measurements from our colleagues on the Biocomplexity Project in the near future and estimate photolytic decay from this data to obtain better estimates of mean residence time. We do not expect our estimates to change by more than a factor of 2, but we will repeat the analysis in this thesis accounting for photolysis and its associated uncertainty when we have secchi dada. We note that the 2003 mean residence time does not precisely represent water entering SP from its watershed, as some of the dye was observed to wash upstream of the dye release – the residence times precisely represent water at the dye release site at the time of the dye release.

In summary, we have observed mean residence times between $0.5 days$ and $20 days$ for water entering SP from its watershed. While the longer mean residence time of $20 days$ has a high associated uncertainty (a factor of $2 - 5$), these measurements give us some idea of the range of residence time scales for water entering SP from SC. The two experiments were conducted under very different environmental conditions, the first during high flow through sparse macrophytes and the second during a period of low net flow and moderate barotropic exchange through extremely dense macrophtyes.

Rueda and Cowen (2005a,b) have shown that coastal upwelling of LO is the most efficient mechanism for exchange between LO and LSB. LSB is an embayment near SP which is more strongly connected to LO, deeper, and has a tiny watershed. In LSB, baroclinic exchange flow induced by upwelling of LO results in much shorter residence times than barotropic exchange. In SP, which is a smaller embayment, it is likely that the relative influence of barotropic exhange is stronger than that up baroclinic exchange. During periods of low LO activity, we may expect to observe residence time scales even longer than that observed during the 2003 study. If we have to estimate the range of mean residence times for water entering SP from its watershed, we would estimate a range of $0.1 days$ to $100 days$, where we emphasize that the number of significant digits in our estimate is 1.

5.2 Potential Benchmark for Numerical Models of Flow Through Macrophytes

After a few small adjustments – namely, adding a photolysis model to the analysis for 2003, entering macrophyte stem length data from a lab notebook for the 2003

study, and characterizing the stem frontal area density and flexural rigidity of the macrophyte species sampled during the two dye studies, we will have a unique field data set that may be used for benchmarking models of flow through flexible vegetation in aquatic systems.

During each of the dye studies, we have extensively characterized the macrophyte distributions in SP (note that macrophytes were sparse in SC and not present at all in LO during the studies). We continuously monitored water surface elevations in SP, flow from SP to LO, temperatures in LO and SC, and wind velocity over the SP – these terms enter the force balance across SP. We have monitored standard meteorological variables that enter the energy budget. We have measured temperature profiles in SP itself – these provide initial conditions and a check of model validity. Residence time distributions, which we measured during each of the dye studies, provide an excellent global-scale check for numerical models as they characterize bulk flow and transport through SP.

We note that ideally, we would have measured the water surface elevation gradient across the surface of SP, as it is this gradient that constitutes the barotropic forcing term in the force balance across SP[1]. Bottom stress, wind stress, and macrophyte drag all provide resistance to barotropic forcing – our measurement of flow rate from SP to LO is the result of barotropic forcing damped by these drag sources. Thus, we cannot tease apart the effect of these different processes. If we

[1]In low-energy freshwater systems such as SP, it is extremely difficult – even impossible, to measure the water surface elevation gradients that drive flow as these gradients are only a few centimeters per kilometer in amplitude. It is impossible, with currently available GPS technology, to determine absolute elevation within more than $1cm$. Instrument settling into the mud bottom of SP creates uncertainty on the order of several centimeters on top of this, so even if we had obtained the latest GPS devices, we would have had to install invasive moored sampling systems to capture the highest amplitude water surface elevation gradients driving flow across SP.

had measured the water surface elevation gradient across SP, we would be able to drive a numerical model with this gradient and test various models for macrophyte drag by comparing the modeled flow from SP to LO to the flow that we measured. Models for wind stress and bottom stress are older and better-validated, so we may tease out these effects by trusting existing models. As it is, we have not measured water surface elevation gradients – if a model is driven with flow rates measured during the dye studies, it should be kept in mind that these flow rates represent the combined effect of barotropic forcing, surface and bottom drag, and macrophyte drag.

Appendix A

Propagation of Correlated Error

Say we measured a time series $F_m(t_i)$ for $i = 1...N$, but the true values are $F(t_i)$. We define the *measurement error* at each time t_i to be $\Delta F(t_i) \equiv F(t_i) - F_m(t_i)$. Note the measurement error is also a time series. Since we can never know what the true value $F(t_i)$ or the measurement error $\Delta F(t_i)$ actually are, we model the error as a random variable and try to estimate its range of possible values. For example, we may say that $F(t_i) = F_m(t_i) \pm \delta F(t_i)$ with 95% confidence, and we call $\delta F(t_i)$ the 95% *uncertainty interval*. The expected value of an error is always zero for a measurement that is not know to be biased. The uncertainty interval is more difficult to estimate. For errors caused by instrument noise, we may measure the noise before the experiment to obtain a distribution. The distribution of instrument noise is generally Gaussian with some standard deviation $\sigma_{\Delta F}$, and corresponding 95% uncertainty interval $\delta F = 2\sigma_{\Delta F}$. Other errors are not so easily quantified, and may not have Gaussian distributions.

Now say we want to integrate $F(t_i)$ discretely in time and let us define

$$V \equiv \sum_{i=1}^{N} F(t_i)\Delta t. \tag{A.1}$$

V is not itself a measured variable, but we have derived it from the measured variables $F(t_i)$, and we may be interested in reporting V along with an appropriate 95% uncertainty. This is not always a simple task because the uncertainty of V depends on how the errors $\Delta F(t_i)$ are correlated in time.

Let us now define the *autocorrelation* $R_{\Delta F}(t_i, t_j)$ and the *correlation coefficient*

$\rho_{\Delta F}(t_i, t_j)$ as follows,

$$\begin{aligned} R_{\Delta F}(t_i, t_j) &\equiv E\left\{\Delta F(t_i)\Delta F(t_j)\right\} \\ \rho_{\Delta F}(t_i, t_j) &\equiv \frac{R_{\Delta F}(t_i, t_j)}{\sigma_{\Delta F}(t_i)\sigma_{\Delta F}(t_j)} \end{aligned}$$

where $E\{\ \}$ is the expected value operator.

The most common errors discussed in the literature of experimental science are *bias* errors and *precision* errors (Moffat 1988). A bias error is an error that does not change in time. For example, if a scale is zeroed while wind exerts a force on the scale equivalent to $0.2g$, a bias error of $0.2g$ will be present in every measurement taken with the scale. A precision error, on the other hand, is statistically independent of previous and future errors. Instrument noise is usually a precision error. The correlation coefficient of bias and precision errors represent two extremes. For a bias error, $\rho_{\Delta F}(t_i, t_j) = 1$ for all (t_i, t_j), and for a precision error,

$$\rho_{\Delta F}(t_i, t_j) = \begin{cases} 1 & \text{for } t_i = t_j, \\ 0 & \text{otherwise.} \end{cases} \tag{A.2}$$

In general, the correlation coefficient may be any function having values between 0 and 1, provided that the two properties $\rho_{\Delta F}(t_i, t_i) = 1$ and $\rho_{\Delta F}(t_i, t_j) = \rho_{\Delta F}(t_j, t_i)$ are satisfied. In fluid mechanics, we often encounter errors that are somewhere in between bias errors and precision errors. These errors are correlated in time, but the correlation does not persist indefinitely. For example, in order to estimate the drag coefficient in a logarithmic boundary layer, we may measure the Reynolds stress by taking the time average of uv, where u and v are perpendicular components of the fluctuating velocity vector. The difference between any one-time measurement of uv and the actual Reynolds stress is correlated for some finite

time (Heathershaw and Simpson 1978). Thus the error in our measurement of the Reynolds stress is neither a bias error nor a precision error.

Let us now consider the general case where the correlation coefficient of our error, $\rho_{\Delta F}(t_i, t_j)$, may be any reasonable function. Given the measured quantities $F(t_i)$ for $i = 1...N$, each having 95% uncertainty $\delta F(t_i)$, and given V, which may be any function of $F(t_i)$, we may wish to compute δV, the 95% uncertainty of V. If all of our errors have Gaussian distributions, we know that $\delta V = 2\sigma_{\Delta V}$, thus we may accomplish this by first finding the error ΔV as a function of the errors $\Delta F(t_i)$, and then computing the variance of the error ΔV, which is simply defined as

$$\sigma^2_{\Delta V} \equiv E\left\{(\Delta V - E\{\Delta V\})^2\right\}. \tag{A.3}$$

This is a straightforward procedure that we may execute for any V that is a function of variables having Gaussian errors.

As a specific example, let us consider the function V defined above by A.1. First, let us calculate ΔV as a function of $\Delta F(t_i)$ as

$$\begin{aligned}
\Delta V &= V - V_m \\
&= \sum_{i=1}^{N} F(t_i)\Delta t - \sum_{i=1}^{N} F_m(t_i)\Delta t \\
&= \sum_{i=1}^{N} \left[F(t_i) - F_m(t_i)\right]\Delta t \\
&= \sum_{i=1}^{N} \Delta F(t)\Delta t.
\end{aligned}$$

Now let us calculate $\sigma^2_{\Delta V}$, the variance of ΔV as follows, making use of the fact

that $E\{\ \}$ is a linear operator,

$$\begin{aligned}
\sigma_{\Delta V}^2 &= E\left\{(\Delta V - E\{\Delta V\})^2\right\} \\
&= E\left\{(\Delta V - 0)^2\right\} \\
&= E\left\{\Delta V^2\right\} \\
&= E\left\{\left(\sum_{i=1}^{N} \Delta F(t_i)\Delta t\right)\left(\sum_{j=1}^{N} \Delta F(t_j)\Delta t\right)\right\} \\
&= (\Delta t)^2 \sum_{i=1}^{N}\sum_{j=1}^{N} E\left\{\Delta F(t_i)\Delta F(t_j)\right\} \\
&= (\Delta t)^2 \sum_{i=1}^{N}\sum_{j=1}^{N} \sigma_{\Delta F}(t_i)\sigma_{\Delta F}(t_j)\rho_{\Delta F}(t_i,t_j)
\end{aligned}$$

It follows that

$$\delta V = \Delta t \sqrt{\sum_{i=1}^{N}\sum_{j=1}^{N} \delta F(t_i)\delta F(t_j)\rho_{\Delta F}(t_i,t_j)}. \tag{A.4}$$

Note that for a bias error, Eq. A.4 reduces to

$$\delta V = \sum_{i=1}^{N} \delta F(t_i)\Delta t, \tag{A.5}$$

and for a precision error, Eq. A.4 reduces to

$$\delta V = \Delta t \sqrt{\sum_{i=1}^{N} \left[\delta F(t_i)\right]^2}. \tag{A.6}$$

Now we may propagate bias errors, precision errors, and any errors for which we can estimate an autocorrelation function through discrete integration provided that the errors are Gaussian.

Appendix B

PPNW10 Conference Proceedings

B.1 Introduction

The following text will appear in the proceedings of the 10th European Workshop on Physical Processes in Natural Waters, cited as King, et. al. (2006) in this thesis. Coastal embayments and wetlands, as mediators between their watersheds and deeper lakes or the ocean, filter watershed runoff, alter its temperature, and provide habitat and breeding grounds for aquatic species that are often important to the ecosystem of the deeper water body.

B.1.1 Physical Processes

The time-dependent velocity and temperature fields and resulting transport time scales of coastal embayments and wetlands are determined by boundary conditions including surface wind stress, surface heating and cooling, and barotropic and baroclinic forcing from the watershed and the larger water body, and by internal conditions including bathymetry, bed roughness, and aquatic vegetation.

B.1.2 Residence Time

Water residence time, defined as the amount of time a water parcel remains in an aquatic system, is a bulk measure of embayment hydrodynamics. Residence time is a function of starting time and location, $(t, \vec{x})$, and for a given $(t, \vec{x})$, is a stochastic variable described by a residence time distribution (RTD – Monsen et. al. 2002). Mean residence time tends to be set by the time scales of physical

processes driving exchange with adjacent systems and the time scales of mixing within the system itself (Rueda and Cowen, 2005b).

The RTD at time t and location $\vec{x}$ may be measured directly by releasing an instantaneous pulse of a passive and conservative tracer at $\vec{x}$ and monitoring the tracer flux out of the system (Hilton et. al. 1998). If the system has only one outlet, and if the tracer is well-mixed across that outlet, then the RTD is given by Eq. B.1, where $r(t)$ is the RTD, $Q(t)$ is volumetric flow rate out of the system, $C(t)$ is the concentration of the tracer at the outlet, and V_0 is the total volume of tracer released.

$$r(t) = \frac{Q(t)C(t)}{V_0} \tag{B.1}$$

As discussed in Hilton et. al., $r(t)$ is not technically the RTD in cases where tracer re-enters the system, but it always has the same mean, and we will loosely refer to $r(t)$ as the RTD. The time integral of $r(t)$, defined as $R(t)$ in Eq. B.2, is the fraction of tracer which no longer remains in the system at time t, and we will loosely refer to $R(t)$ as the cumulative residence time distribution (CRTD).

$$R(t) = \int_0^t r(\tau)d\tau \tag{B.2}$$

B.1.3 Study Site

Sterling Pond (SP) is a small and shallow freshwater embayment that drains Sterling Creek, bordering wetlands, and a large watershed ($210km^2$) into Lake Ontario (LO) through a long, narrow, and shallow manmade channel ($100m \times 17m \times 3m$) – a bathymetric map of SP is provided in Figure B.1. From late spring through early

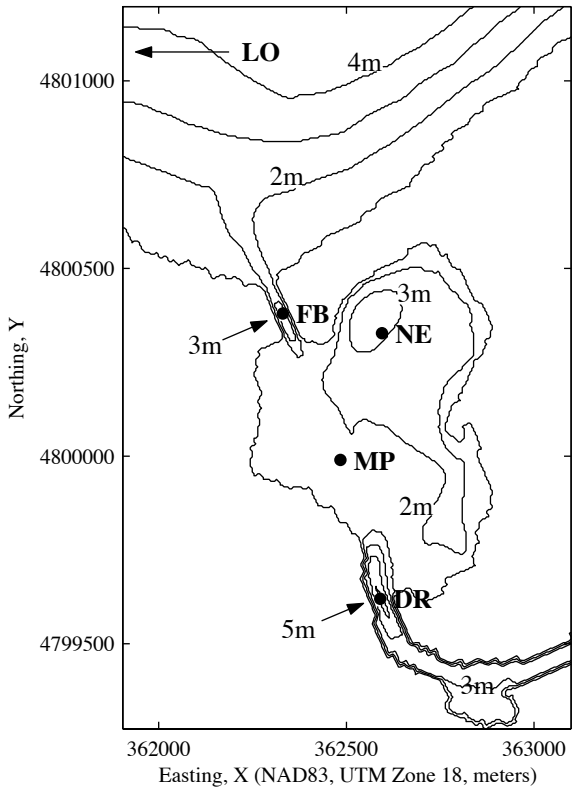

Figure B.1: Bathymetry of Sterling Pond and equipment locations. The LO site is located $1.5km$ to the west on the $6m$ isobath of Lake Ontario.

fall, SP is home to diverse populations of submerged aquatic vegetation (macrophytes) which undergo one or more periods of dense growth.

B.1.4 Objective and Approach

Because of its small size, large watershed, strong connection to LO, and highly variable macrophyte populations, the hydrodynamics and resulting water residence times of SP result from the interaction of all of the physical processes discussed above. To decipher these processes and to characterize the residence time scales of SP, dye studies were conducted in synchrony with extensive macrophyte surveys and continuous monitoring of temperature, water surface elevation, channel

flow rate, and meteorological conditions. The results of these studies comprise a benchmark data set for investigation of flow through macrophyte-dominated coastal embayments.

B.2 Materials and Methods

B.2.1 Dye Release Studies

The two dye release studies discussed in this paper commenced on May 15, 2002 and September 18, 2003. The 2002 experiment was conducted during a period of high watershed flows following a spring snow-melt event. The 2003 experiment was conducted during a period of intermittent coastal upwelling in LO and high lake level oscillations instigated by high winds following hurricane Isabel.

Each experiment began with the release of a plug of $3.79L$ (2002) or $7.57L$ (2003) of Rhodamine WT (20% by weight solution) through a vertical line-source diffuser at site DR (see Figure B.1). After the release, the volumetric flow rate, $Q(t)$, from SP to LO was continuously monitored at site FB as was the concentration of RWT, $C(t)$.

Flow rate was measured as follows – a vertical velocity profile was measured in the center of the channel with an RDI $1200kHz$ Workhorse Monitor acoustic Doppler current profiler (ADCP) looking upward from the bed. The horizontal boundary layers were characterized in a separate experiment, and combining the results of this experiment with measured channel bathymetry and the vertical centerline velocity profiles, an accurate estimate of $Q(t)$ was obtained.

Concentration was measured with a Turner Designs 10-AU flow-through fluorometer. The fluorometer intake tube was positioned in the center of the channel

to sample water exiting SP near the ADCP. The sampling intervals for concentration and velocities were between $0.33s$ and $5s$ – time series were ensemble averaged over a time scale longer than the longest turbulent time scale but shorter than the high energy barotropic oscillations (see Lohrmann et. al. 1990), determined from longitudinal velocity spectra (not shown) to be $2min$ in 2002 and $8min$ in 2003.

B.2.2 Continuous Monitoring

Throughout the dye studies, water temperatures in SP and LO were monitored in vertical profiles with chains of Sea Bird Electronics SBE-39 thermistors recording at $1-2min$ time intervals. Thermistor chains were located in Lake Ontario (site LO in Figure B.1), at the dye release site (DR), at the midpoint of the pond (MP), at the deepest point in the northeast lobe (NE), and in the channel connecting SP to LO (FB). Water surface elevation in SP was monitored at $1-2min$ intervals with an SBE-39 temperature/pressure recorder on the bed at DR. Meteorological conditions, including wind speed, wind direction, air temperature, atmospheric pressure, relative humidity, and short wave radiation were recorded in $15min$ intervals at a station located $1km$ west of SP on the shore of neighboring Little Sodus Bay. Together with these measured variables, flow rate from SP to LO, monitored as part of the dye release study described above, completes the measured history of external hydrodynamic forcing and the internal response of SP during the dye studies.

B.2.3 Macrophyte Surveys

Macrophyte abundance, height, and species composition were sampled in 41 $100m\times 100m$ quadrates in SP on a monthly (and sometimes more frequent) basis through-

out the 2002 and 2003 growing seasons. Macrophytes were hand-harvested by diving and cutting the stems at the substrate-water interface. Samples were taken from a $0.25m$ square frame randomly tossed in each quadrate. Plant heights were measured in the field. Species were separated in the lab and dried for $48hrs$ at 105^oC to determine dry biomass on a per-species basis.

B.3 Analysis and Results

B.3.1 Hydrodynamic Forcing

A summary of the forces driving hydrodynamics and resulting water residence times in SP during the two dye studies is provided in Figure B.2. In order to decipher to some extent the relative impact of barotropic forcing from the watershed and LO, the bulk velocity in the channel, u, was decomposed into a $12hr$ moving average time series, $\langle u \rangle$, and the root $12hr$-mean square residual, $\langle u'^2 \rangle$. The $12hr$ averaging period was chosen to distinguish the barotropic modes of LO from the longer time-scale watershed processes (Hamblin 1982, Rueda and Cowen 2006b). The magnitude of barotropic forces (per unit width) from the watershed and from LO were then estimated by Eqs. B.3 and B.4, respectively, where ρ is water density and H is the time-dependent water depth at site FB. The baroclinic force (per unit width) from LO was estimated from the bulk density difference between site DR and LO by Eq. B.5. The wind force may also be estimated, but its effect is thought to be small compared to that of the other forces (Andradóttir and Nepf 2000b, Rueda and Cowen 2005b). Note that these are simple order-of-magnitude estimates and that the ratio of the barotropic to baroclinic forces is the square of the Froude number.

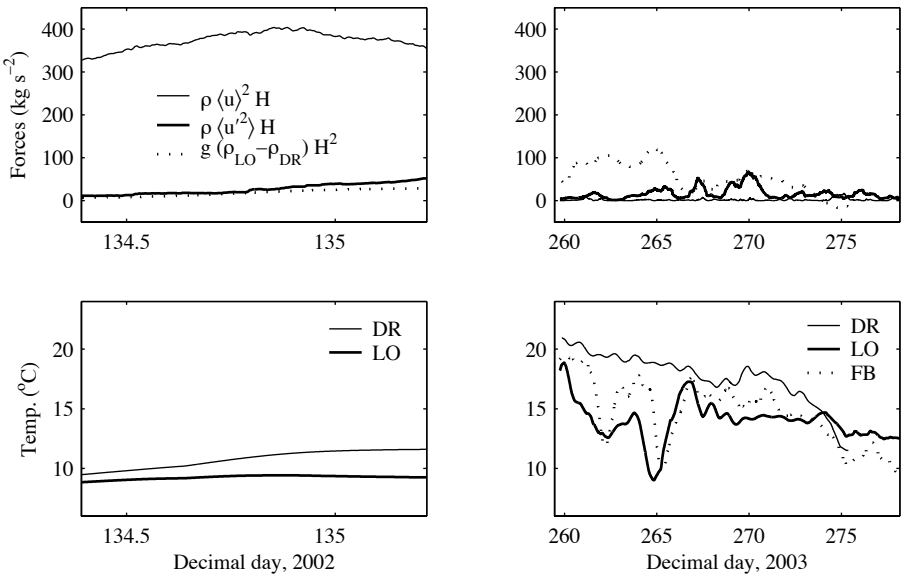

Figure B.2: Barotropic forcing from the watershed, barotropic forcing from Lake Ontario, and baroclinic forcing from Lake Ontario (see Eqs. B.3-B.4) during the 2002 and 2003 dye experiments are plotted in the top two panels. The temperatures at sites DR and LO are plotted in the bottom two panels. For the 2003 experiment, the temperature at site FB is also plotted. All temperatures are averaged over the top $3m$ of the water column.

$$F_{bt,w} = \rho \langle u \rangle^2 H \tag{B.3}$$

$$F_{bt,L} = \rho \langle u'^2 \rangle H \tag{B.4}$$

$$F_{bc,L} = g(\rho_{LO} - \rho_{DR}) H^2 \tag{B.5}$$

In Figure B.2, we see that during the 2002 dye study, barotropic forcing from the watershed dwarfed all forcing from LO. In contrast, during the 2003 study, barotropic forcing from the watershed was extremely weak and baroclinic and barotropic forcing from LO were of moderate magnitude. The effect of these forces on the dynamics of SP is not immediately clear, but the temperature time histories plotted in Figure B.2 give some indication of the impact of baroclinic forcing – we see that during coastal upwelling of LO (days 260-267), cold hypolymnetic water

from LO appears to enter SP through the channel. Time histories at NE and MP (not shown) also indicate an inrush of LO hypolymnetic water.

B.3.2 Macrophyte Distributions

As shown in Figure B.3, macrophytes were sparse during the 2002 dye study, although some biomass was located in the northeast lobe of the pond and near the channel, whereas during the 2003 study, macrophytes were both thick and relatively uniform in density. Species composition (not shown) in SP is highly dynamic – during the 2002 study, dense patches consisted primarily of *C. demersum*, *E. nuttalli*, and *P. crispus*; during the 2003 study, the west side of the pond was dominated by *N. obtusa* while *C. demersum* and *E. nuttalli* occupied the northeast lobe. Efforts are underway to characterize the frontal area per unit volume and the drag coefficient for these macropyhte species and to investigate the importance of vegetative drag and longitudinal dispersion (see Nepf 1999, Lightbody and Nepf 2006).

B.3.3 Residence Time

For each experiment, $r(t)$ was computed from $Q(t)$ and $C(t)$ measured at site FB using Eq. B.1. Uncertainty due to bias error, precision error, and errors correlated over intermediate time scales were considered separately so that uncertainty in time-integrated statistics, such as $R(t)$ and mean residence time could be estimated accurately. The raw time series of $r(t)$ are plotted in Figure B.4 and the time series of $R(t)$ with error bars are plotted in Figure B.5. Roughly 60% of the dye exited SP during each of the studies. In order to compute statistics of residence time, $r(t)$ had to be extrapolated until over 99% had left. The standard procedure is to fit

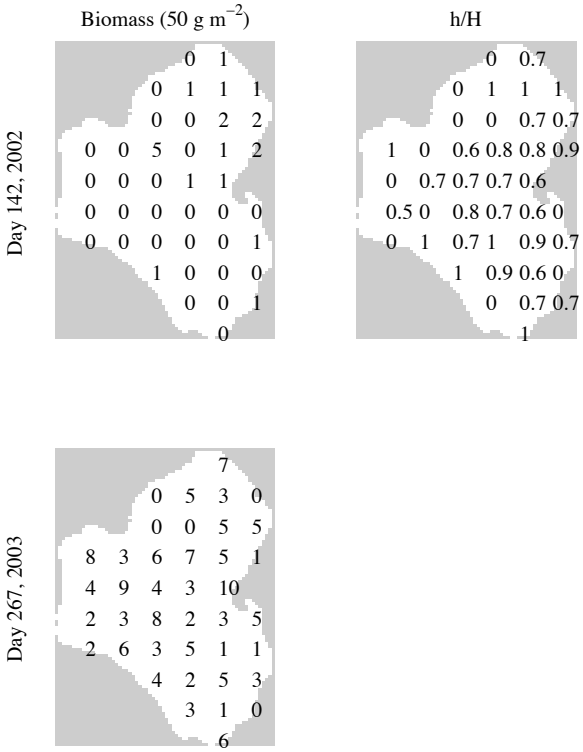

Figure B.3: Total above-ground macrophyte dry weight (biomass) and emergence ratio, h/H, measured in 41 $100m \times 100m$ quadrates eight days after the 2002 dye study and during the 2003 study (emergence ratio not shown for the 2003 study as data processing is ongoing). Note that biomass is plotted in units of $50g/m^2$ so that 1 unit is near the lower limit of what is considered "dense" vegetation.

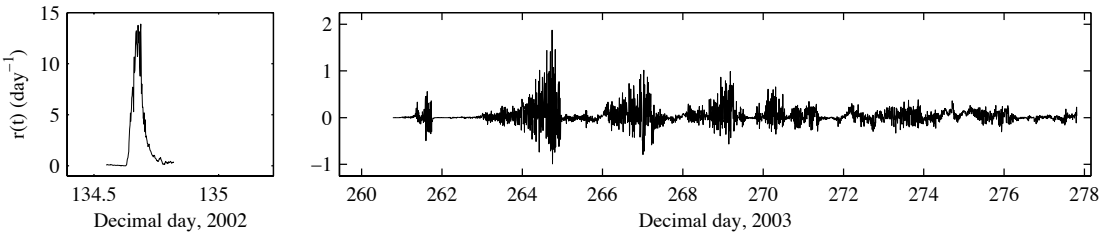

Figure B.4: Measured RTD's for the 2002 and 2003 dye studies. Each time series begins at the time of dye release. Note that error bars are not shown because they would obscure detail – see Figure B.6 for instantaneous uncertainty in the 2002 RTD, and see Figure B.5 for cumulative uncertainty in both experiments.

an exponential tail – this is reasonable if the embayment is well-mixed toward the end of the experiment, resulting in exponential decay toward zero. For these two studies, however, such a fitted exponential tail predicts that significantly less than 100% of the dye leaves the embayment. An alternative method is to extrapolate $R(t)$ by finding the decay rate k which minimizes the mean-square residual for Eq. B.6 under the constraint that all of the mass eventually exits the embayment. This constraint requires that r_0 and k satisfy Eq. B.7 where t_N is the time of the final measurement. For each study, $R(t)$ was extrapolated by this method, and mean residence time was estimated from the corresponding extrapolated time history of $r(t)$.

$$R(t) = 1 - r_0 e^{-kt} \tag{B.6}$$

$$r_0 = \big(1 - R(t_N)\big) e^{kt_N} \tag{B.7}$$

There are two types of error implicit in this extrapolation method. The first is error in the exponential model – this error is clearly present because if the embayment were indeed fully mixed toward the end of the experiment as the

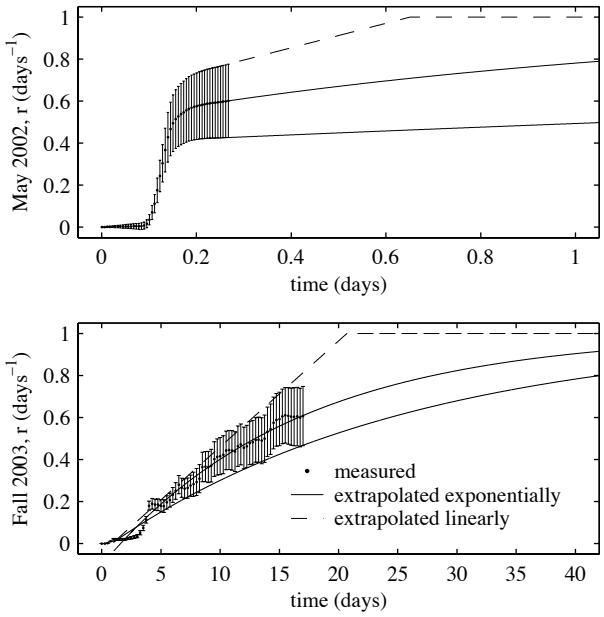

Figure B.5: Measured CRTD with error bars for the 2002 and 2003 experiments along with extrapolated tails. The tail of the expected value and the lower bound are extrapolated exponentially while the tail for the upper bound is extrapolated linearly to give a conservative estimate of the lower bound on mean residence time.

exponential model assumes, then a straightforward fit to the tail of $r(t)$ would predict that all of the mass exits the embayment, and this condition had to be imposed artificially. The second error propagates from the measured data. This error was estimated by extrapolating the upper and lower bounds of $R(t)$ – a more rigorous method would be to stochastically fit the curve accounting for the time correlation of the various contributions to uncertainty in $R(t)$, but fitting the upper and lower bounds gives a first order uncertainty estimate. The upper bound was extrapolated linearly to obtain a more conservative lower bound on the mean residence time. The resulting mean residence times with upper and lower bounds estimated from measurement error are given in Table B.1. The model error is not accounted for here but is explored in the next section by using a more physically valid model to extrapolate the 2002 RTD.

Table B.1: Estimates of mean residence time (*days*) for each dye experiment and each extrapolation method.

	extrapolated	dead-zone
2002	$[0.22, 0.56, 0.79]$	0.88
2003	$[16.1, 18.1, 19.9]$	–

B.3.4 Dead-Zone Model

For the 2002 experiment, a dead-zone model was fitted to the data in order to explore the physical processes and extrapolate the tail of the RTD. This type of model was developed to explain enhanced dispersion in rivers with side-lobes (e.g. Valentine and Wood 1977) and further developed for use in wetlands by Andradóttir and Nepf (2000a,b). The idea is that a channel exhibiting classic plug-flow with longitudinal dispersion is coupled to a stationary "dead zone" through bulk diffusion. The model equations for transport of a conservative passive tracer are given by Eqs. B.8 and B.9 where C_c is the tracer concentration in the channel, C_d is the tracer concentration in the dead zone, u is longitudinal velocity, L is the length of the system, $q = A_c/(A_c + A_d)$ where A_c and A_d are the cross-sectional areas of the channel and dead zone, respectively, K_x is longitudinal dispersion, and $\alpha^* = \Delta Q/Q$ is the ratio of the volumetric channel/dead zone exchange rate, ΔQ, and the channel flow rate, Q.

$$\frac{\partial C_c}{\partial t} + u\frac{\partial C_c}{\partial x} = K_x\frac{\partial^2 C_c}{\partial x^2} + \frac{\alpha^* u}{L}(C_d - C_c) \tag{B.8}$$

$$\frac{\partial C_d}{\partial t} = -\frac{\alpha^* u}{L}\frac{q}{1-q}(C_d - C_c) \tag{B.9}$$

Eqs. B.8 and B.9 were solved using an upwind differencing scheme with time-

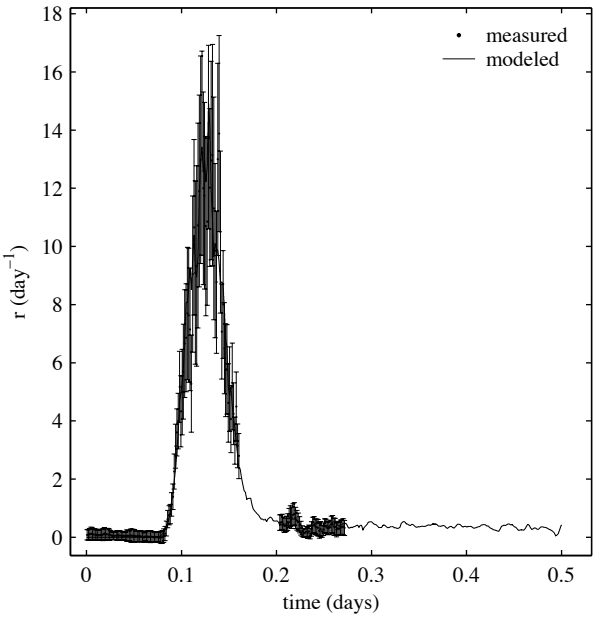

Figure B.6: Measured RTD with error bars (indicating total instantaneous uncertainty) for the 2002 experiment along with the best-fit dead-zone model solution. Time 0 is the dye release time.

dependent velocity and longitudinal dispersion. Length, L, was taken to be $835m$, corresponding to the distance between DR and FB. Time-dependent velocity was computed from the outflow and cross-sectional area measured at site FB by $u = Q/(\theta A_{FB})$ where θ is a dimensionless parameter relating the time-dependent area of the channel under the footbridge, A_{FB} to the mean cross-sectional area of the channel, A_c. Time-dependent longitudinal dispersion was computed from velocity by $K_x = \gamma h u$, where $h = 2m$ is the estimated average depth of the channel and γ is a dimensionless constant which in a natural stream is about 0.6 (Fischer et. al. 1979).

The equations were solved on a domain of length $3L$ and the concentration gradient was set to zero on the boundaries. The concentration fields were initialized at zero with the exception of the channel concentration at $x = L$, which was initialized at $V_0/(\Delta x \theta A_{FB})$. The time series of concentration at $x = 2L$ was

compared with the measured time series of concentration at site FB, and the model was fitted to the data by varying the parameters γ, α^*, q, and θ to minimize the sum-square error. Andradóttir and Nepf (2000b) suggest that during periods of high flow, $\alpha^* \approx 1$, and q may be roughly predicted from the length to width ratio L/W of the wetland (or embayment) and the spreading rate of the entering jet, $\beta \approx 1$, by $q \approx \beta L/W$. For SP this works out to $q \approx 0.15$. These estimates were used as a starting point in the search for a best fit. The sum square residual was minimized by the parameters $\gamma = 4.5$, $\alpha^* = 0.55$, $q = 0.25$ and $\theta = 4$. All of these parameters are within an order of magnitude of the values predicted by simple scaling analysis.

The dead zone model fits the data splendidly and provides a more physically based means to extrapolate the tail of the measured RTD. Solving the best-fit dead zone model using flow rates measured after the end of the dye study yields a mean residence time of $0.88 days$. The mean residence time is quite sensitive to model parameters, and for other solutions falling within the error bounds of the measured data, mean residence times between $0.6 days$ and $1.8 days$ are obtained. This uncertainty is due to the sensitivity of mean residence time to the shape of the RTD tail and to the fact that the experiment was terminated before the shape of the tail was well-established. Towards the end of the residence time curve for the dead zone model, exponential decay is approached, but along the way the decay rate itself decays – we may now see that this is the reason exponential extrapolation of the 2002 RTD without the conservation of mass constraint failed. We observe that with the constraint of mass conservation, exponential extrapolation of the CRTD predicts mean residence time within 60% of that predicted by the dead-zone model for the 2002 experiment. This gives us some estimate of our confidence

in the extrapolated 2003 RTD.

B.4 Conclusions

The dye studies and extensive macrophyte surveys discussed herein comprise a unique data set for investigating flow and transport through macrophyte-dominated coastal embayments and wetlands. Scaling analysis suggests that barotropic forcing from the watershed and both barotropic and baroclinic forcing from the adjacent lake can all be important in this type of system. Mean residence time scales were estimated for two different forcing regimes and a dead-zone model was used to explain the physics in one of the experiments where barotropic watershed forcing dominated. The measured residence time distributions are integrated measures of embayment hydrodynamics and can be used in the future to calibrate and verify models accounting explicitly for the effect of macrophytes.

Appendix C

Macrophyte Survey Data

Table C.1: Data from the macrophyte survey conducted on May 23, 2002 (decimal day 142). Data from each plot includes biomass density in terms of dry weight (D. W.), mean stem length (L), and species composition (S.C.) in terms of percent dry weight.

Plot	L (m)	D. W. (g/m^2)	Species	S. C. (% D. W.)
2	1.19	19.6	*Nuphar advena*	82
			Potamogeton pusillus	14
			Ceratophyllum demersum	3.6
			Elodea sp.	1.0
3	1.19	53.5	*Ceratophyllum demersum*	98
			Utricularia vulgaris	1.4
			Lemna trisulca	0.74
			Potamogeton pusillus	0.15
			Elodea sp.	0.037
4	1.17	8.84	*Nuphar advena*	96
			Potamogeton pusillus	4.0
6	3.25	33.3	*Ceratophyllum demersum*	53
			Potamogeton zosteriformis	17
			Elodea sp.	15
			Potamogeton pusillus	13
			Myriophyllum sibricum	1.8
			Zosterella dubia	0.33
7	1.31	11.1	*Potamogeton pusillus*	98
			Elodea sp.	1.5
8	1.2	22.2	*Potamogeton pusillus*	86
			Nuphar advena	10
			Myriophyllum sibricum	2.7
			Elodea sp.	1.1
			Potamogeton crispus	0.20
10	1.17	27.1	*Ceratophyllum demersum*	95
			Lemna trisulca	3.9
			Potamogeton pusillus	0.92
11	1.49	0.336	*Ceratophyllum demersum*	43
			Lemna trisulca	33
			Elodea sp.	24
12	1.25	5.52	*Potamogeton pusillus*	100

Table C.1 (Continued)

Plot	L (m)	D. W. (g/m^2)	Species	S. C. (% D. W.)
13	1.06	18.7	*Potamogeton pusillus*	74
			Potamogeton zosteriformis	10
			Ceratophyllum demersum	10
			Elodea sp.	3.3
			Myriophyllum sibricum	1.1
			Chara vulgaris	0.43
			Lemna trisulca	0.43
			Potamogeton crispus	0.43
14	1.35	10.8	*Potamogeton pusillus*	100
16	0.73	5.91	*Potamogeton pusillus*	63
			Ceratophyllum demersum	25
			Vallisneria americana	5.0
			Elodea sp.	4.6
			Chara vulgaris	1.4
			Lemna trisulca	1.4
18	1.25	1.85	*Potamogeton pusillus*	100
19	1.14	2.09	*Potamogeton pusillus*	100
20	1.12	1.75	*Elodea sp.*	57
			Potamogeton crispus	20
			Ceratophyllum demersum	8.9
			Lemna trisulca	4.6
			Myriophyllum sibricum	4.6
			Potamogeton pusillus	4.6
22	1.21	43.1	*Elodea sp.*	75
			Myriophyllum sibricum	18
			Ceratophyllum demersum	3.5
			Lemna trisulca	1.8
			Potamogeton crispus	1.2
			Potamogeton pusillus	0.19
23	1.65	26.7	*Elodea sp.*	37
			Ceratophyllum demersum	28
			Potamogeton crispus	21
			Potamogeton pusillus	14
			Myriophyllum sibricum	0.31
24	1.56	5.42	*Ceratophyllum demersum*	66
			Elodea sp.	31
			Potamogeton pusillus	3.4
25	1.44	1.43	*Potamogeton pusillus*	80
			Potamogeton zosteriformis	16
			Chara vulgaris	3.7
27	1.54	6.00	*Myriophyllum sibricum*	92

Table C.1 (Continued)

Plot	L (m)	D. W. (g/m^2)	Species	S. C. (% D. W.)
			Potamogeton crispus	3.3
			Potamogeton pusillus	2.0
			Chara vulgaris	1.3
			Lemna trisulca	1.3
29	1.65	236	*Potamogeton crispus*	99
			Elodea sp.	0.66
			Ceratophyllum demersum	0.60
30	1.85	22.3	*Potamogeton crispus*	90
			Elodea sp.	9.3
			Ceratophyllum demersum	1.0
31	1.76	52.5	*Ceratophyllum demersum*	99
			Elodea sp.	1.0
			Zosterella dubia	0.092
32	1.66	90.8	*Lemna trisulca*	65
			Ceratophyllum demersum	34
			Myriophyllum sibricum	0.65
			Zosterella dubia	0.62
33	1.46	93.5	*Ceratophyllum demersum*	52
			Potamogeton crispus	32
			Lemna trisulca	9.1
			Myriophyllum sibricum	2.8
			Zosterella dubia	2.0
			Elodea sp.	1.6
			Myriophyllum spicatum	0.17
34	1.8	119	*Elodea sp.*	71
			Potamogeton crispus	18
			Ranunculus trichophyllus	5.2
			Ceratophyllum demersum	3.9
			Lemna trisulca	2.1
			Zosterella dubia	0.33
			Najas flexilis	0.067
38	3.2	63.5	*Ceratophyllum demersum*	96
			Potamogeton crispus	3.1
			Elodea sp.	0.81
39	2.32	53.9	*Ceratophyllum demersum*	54
			Potamogeton crispus	41
			Elodea sp.	3.4
			Zosterella dubia	0.66
			Myriophyllum sibricum	0.39
40	1.97	31.2	*Ceratophyllum demersum*	89
			Elodea sp.	6.9

Table C.1 (Continued)

Plot	L (m)	D. W. (g/m^2)	Species	S. C. (% D. W.)
			Potamogeton crispus	4.1
			Lemna trisulca	0.26
41	1.12	53.1	*Elodea sp.*	42
			Potamogeton crispus	36
			Ceratophyllum demersum	18
			Myriophyllum sibricum	4.2

Table C.2: Data from the macrophyte survey conducted on September 25, 2003 (decimal day 267). Data from each plot includes biomass density in terms of dry weight (D. W.) and species composition (S.C.) in terms of percent dry weight.

Plot	D. W. (g/m^2)	Species	S. C. (% D. W.)
2	286	*Ceratophyllum demersum*	93
		Nuphar odorata	4
		Elodea sp.	2
		Potamogeton zosteriformis	1
		Myriophyllum spicatum	0
		Lemna trisulca	0
3	3.28	*Myriophyllum spicatum*	71
		Nitellopsis obtusa	22
		Lemna trisulca	3.9
		Potamogeton zosteriformis	2.9
4	71.9	*Ceratophyllum demersum*	81
		Potamogeton zosteriformis	4.8
		Utricularia spp.	4.5
		Lemna trisulca	4.1
		Elodea sp.	3.1
		Nitellopsis obtusa	2.6
		Najas flexilis	0.38
5	172	*Nitellopsis obtusa*	98
		Potamogeton pusillus	1.9
		Elodea sp.	0.35
		Myriophyllum spicatum	0.13
		Potamogeton zosteriformis	0.05
		Lemna trisulca	0.0023

Table C.2 (Continued)

Plot	D. W. (g/m^2)	Species	S. C. (% D. W.)
6	199	*Nitellopsis obtusa*	96
		Vallisneria americana	3.1
		Potamogeton zosteriformis	0.15
		Ceratophyllum demersum	0.12
		Utricularia spp.	0.10
		Myriophyllum spicatum	0.064
		Elodea sp.	0.028
		Potamogeton pusillus	0.006
		Lemna trisulca	0.0020
7	109	*Nitellopsis obtusa*	100
		Ceratophyllum demersum	0
		Elodea sp.	0
8	245	*Nitellopsis obtusa*	88
		Ceratophyllum demersum	12
		Potamogeton zosteriformis	0.055
		Lemna trisulca	0.0049
9	140	*Ceratophyllum demersum*	66
		Elodea sp.	16
		Nitellopsis obtusa	13
		Ranunculus spp.	3.6
		Lemna trisulca	0.94
		Potamogeton zosteriformis	0.38
		Najas flexilis	0.060
10	48.8	*Ceratophyllum demersum*	95
		Myriophyllum spicatum	2.4
		Lemna trisulca	1.8
		Elodea sp.	0.61
		Potamogeton zosteriformis	0.55
11	48.7	*Nitellopsis obtusa*	43
		Utricularia spp.	23
		Ceratophyllum demersum	17
		Elodea sp.	10
		Najas flexilis	3.7
		Lemna trisulca	2.6
		Potamogeton zosteriformis	0.016
12	234	*Nitellopsis obtusa*	100
		Vallisneria americana	0.16
		Lemna trisulca	0.0068
13	168	*Ceratophyllum demersum*	58
		Nitellopsis obtusa	24

Table C.2 (Continued)

Plot	D. W. (g/m^2)	Species	S. C. (% D. W.)
		Potamogeton zosteriformis	10
		Myriophyllum spicatum	4.9
		Utricularia spp.	2.1
		Vallisneria americana	0.43
		Lemna trisulca	0.31
		Potamogeton crispus	0.29
		Ranunculus spp.	0.19
		Elodea sp.	0.11
14	290	*Nitellopsis obtusa*	98
		Potamogeton zosteriformis	1.1
		Myriophyllum spicatum	1.1
15	82.9	*Nitellopsis obtusa*	96
		Myriophyllum spicatum	4.4
16	78.6	*Myriophyllum spicatum*	65
		Nuphar odorata	17
		Elodea sp.	15
		Vallisneria americana	3.3
		Potamogeton pusillus	0.12
		Ceratophyllum demersum	0.092
		Lemna trisulca	0.066
		Nitellopsis obtusa	0.056
17	134	*Nitellopsis obtusa*	93
		Myriophyllum spicatum	5.7
		Potamogeton zosteriformis	0.65
		Potamogeton crispus	0.30
18	404	*Nitellopsis obtusa*	91
		Ceratophyllum demersum	3.6
		Myriophyllum spicatum	3.1
		Potamogeton zosteriformis	1.6
		Elodea sp.	0.15
		Vallisneria americana	0.13
		Potamogeton pusillus	0.028
		Najas flexilis	0.022
		Lemna trisulca	0.017
		Lemna minor	0.0010
19	96.9	*Nitellopsis obtusa*	59
		Elodea sp.	18
		Ceratophyllum demersum	12
		Potamogeton zosteriformis	8.9
		Vallisneria americana	1.9

Table C.2 (Continued)

Plot	D. W. (g/m^2)	Species	S. C. (% D. W.)
		Chara vulgaris	0.72
		Najas flexilis	0.22
		Potamogeton pusillus	0.0041
20	125	*Ceratophyllum demersum*	90
		Myriophyllum spicatum	5.0
		Elodea sp.	4.8
		Lemna trisulca	0.38
21	244	*Nuphar odorata*	50
		Ceratophyllum demersum	29
		Myriophyllum spicatum	14
		Elodea sp.	3.3
		Nitellopsis obtusa	2.2
		Lemna trisulca	1.6
		Potamogeton zosteriformis	0.09
		Megalodonta beckyii	0.023
		Najas marina	0.020
22	500	*Ceratophyllum demersum*	98
		Lemna trisulca	0.93
		Potamogeton zosteriformis	0.85
23	156	*Elodea sp.*	60
		Ceratophyllum demersum	34
		Myriophyllum spicatum	6.0
		Potamogeton crispus	0.54
		Nitellopsis obtusa	0.028
24	197	*Nitellopsis obtusa*	70
		Ceratophyllum demersum	20
		Potamogeton zosteriformis	3.1
		Myriophyllum spicatum	2.3
		Potamogeton pusillus	2.0
		Elodea sp.	1.9
		Lemna trisulca	0.11
		Potamogeton crispus	0.0041
25	470	*Nitellopsis obtusa*	100
		Ceratophyllum demersum	0.024
		Potamogeton zosteriformis	0.022
		Vallisneria americana	0.014
		Elodea sp.	0.0009
26	191	*Nitellopsis obtusa*	47
		Elodea sp.	21
		Myriophyllum spicatum	20

Table C.2 (Continued)

Plot	D. W. (g/m^2)	Species	S. C. (% D. W.)
		Vallisneria americana	8.8
		Ceratophyllum demersum	3.5
		Potamogeton zosteriformis	0.69
27	412	*Nitellopsis obtusa*	90
		Myriophyllum spicatum	5.3
		Vallisneria americana	3.2
		Ceratophyllum demersum	1.2
		Elodea sp.	0.64
		Potamogeton zosteriformis	0.13
28	137	*Nitellopsis obtusa*	71
		Ceratophyllum demersum	24
		Vallisneria americana	3.5
		Myriophyllum spicatum	1.0
		Potamogeton crispus	0.16
		Elodea sp.	0.11
		Potamogeton zosteriformis	0.088
		Lemna trisulca	0.044
29	318	*Ceratophyllum demersum*	99
		Myriophyllum spicatum	1.5
		Lemna trisulca	0.0025
30	334	*Ceratophyllum demersum*	51
		Elodea sp.	48
		Myriophyllum spicatum	0.90
		Potamogeton crispus	0.21
		Lemna trisulca	0.15
31	248	*Ceratophyllum demersum*	97
		Vallisneria americana	2.9
		Lemna trisulca	0.052
		Elodea sp.	0.018
32	68.2	*Ceratophyllum demersum*	86
		Lemna trisulca	10
		Potamogeton zosteriformis	1.5
		Elodea sp.	1.1
		Myriophyllum spicatum	1.0
33	254	*Ceratophyllum demersum*	96
		Potamogeton zosteriformis	2.0
		Lemna trisulca	1.2
		Vallisneria americana	0.50
		Elodea sp.	0.33
		Zosterella dubia	0.29

Table C.2 (Continued)

Plot	D. W. (g/m^2)	Species	S. C. (% D. W.)
34	258	*Ceratophyllum demersum*	98
		Myriophyllum spicatum	1.4
		Elodea sp.	0.47
		Lemna trisulca	0.14
		Potamogeton crispus	0.091
35	16.8	*Ceratophyllum demersum*	56
		Myriophyllum spicatum	32
		Lemna trisulca	7.3
		Utricularia spp.	4.3
		Potamogeton crispus	0.21
36	0.00	no plants	
37	0.00	no plants	
38	227	*Ceratophyllum demersum*	93
		Myriophyllum spicatum	7.3
		Potamogeton crispus	0.067
		Lemna trisulca	0.026
		Elodea sp.	0.0035
39	175	*Ceratophyllum demersum*	100
		Lemna trisulca	0.021
40	14	*Vallisneria americana*	74
		Myriophyllum spicatum	26
41	338	*Ceratophyllum demersum*	99
		Myriophyllum spicatum	0.77
		Lemna trisulca	0.27
		Potamogeton zosteriformis	0.059
		Elodea sp.	0.027

BIBLIOGRAPHY

Andradóttir, H.Ó., and H.M. Nepf. 2000a. Thermal mediation by littoral wetlands and impact on lake intusion depth. *Water Resour. Res.* **36:** 725-735.

Andradóttir, H.Ó., and H.M. Nepf. 2000b. Thermal mediation in a natural littoral wetland: Measurements and modeling. *Water Resour. Res.* **36:** 2937-2946.

Chapra, S.C. 1997. *Surface Water-Quality Monitoring.* McGraw-Hill, St. Louis.

Coles, D. 1956. The law of the wake in the turbulent boundary layer. *J. Fluid Mech.* **1:** 191-226.

Cowen, E.A., and F.J. Rueda. 2004. Exchange Flows thorough a Long Shallow Channel. *Shallow Flows: Research presented at the International Symposium on Shallow Flows.* June 16-18 2003. Delft University of Technology, The Netherlands. ISBN 9058097005.

Csanady, G.T. 1977. Intermittent "full" upwelling in Lake Ontario. *J. Geophys. Res.* **82:** 397-419 .

Donaldson, D.E., and T.W. Robinson. 1971. Fluorescent dyes, their uptake and translocation in plants. *Water Resour. Res.* **7:** 692-696.

Efron, B.R. and R. Tibshirani. 1993. *An Introduction to the Bootstrap.* Chapman & Hall.

Fischer, H.B., E.J. List, R. Koh, J. Imberger, and N. Brooks. 1979. *Mixing in Inland and Coastal Waters.* Academic, New York.

Gill, A.E. 1982. *Atmosphere-Ocean Dynamics.* Academic, New York.

Hamblin, P.F. 1982. On the free surface oscillations of Lake Ontario. *Limnol. Oceanogr.* **27:** 1039-1049.

Heathershaw, A.D., and J.H. Simpson. 1978. The sampling variability of the Reynolds stress and its relation to boundary shear stress and drag coefficient measurements. *Estuarine Coastal Mar. Sci.* **6:** 263-274.

Hilton, A.B.C., D.L. McGillivary, and E.E. Adams. 1998. Residence time of freshwater in Boston's Inner Harbor. *J. Waterw. Port Coast. Eng.* **124:** 82-89.

King, A.T., R.L. Johnson, and E.A. Cowen. Effects of a strong connection to Lake Ontario, a large watershed, and dynamic plant populations on the hydrodynamics and resulting water residence times of a small coastal embayment. *Proceedings of the 10th European Workshop on Physical Processes in Natural Waters.* June 26-28, 2006. University of Granada, Spain.

Kline, S.J., and F.A. McClintock. 1953. Describing uncertainties in single-sample experiments. *Mech. Eng.* **1:** 3-8.

Levenspiel, O. 1999. *Chemical Reaction Engineering, 3rd ed.* John Wiley & Sons, New York.

Lightbody, A.F., and H.M. Nepf. 2006. Prediction of velocity profiles and longitudinal dispersion in emergent salt march vegetation. *Limnol. Oceanogr.* **51:** 218-228.

Lohrman, A., B. Hackett, and L.P. Røed. 1990. High resolution measurements of turbulence, velocity, and stress using a pulse-to-pulse coherent sonar. *J. Atmos. Ocean. Technol.* **7:** 19-37.

Lorke, A., L. Umlauf, T. Jonas, and A. Wüest. 2002. Dynamics of turbulence in low-speed oscillating bottom-boundary layers of stratified basins. *Environmental Fluid Mechanics.* **2:** 291-313.

Lu, Y., and R.G. Lueck. 1999a. Using a broadband ADCP in a tidal channel. Part I: Mean flow and shear. *J. Atmos. Ocean. Technol.* **16:** 1556-1567.

Lu, Y., and R.G. Lueck. 1999b. Using a broadband ADCP in a tidal channel. Part II: Turbulence. *J. Atmos. Ocean. Technol.* **16:** 1568-1579.

Moffat, R.J. 1988. Describing uncertainties in experimental results. *Experimental Thermal and Fluid Science.* **1:** 3-17.

Monsen, N.E., J.E. Cloern, and L.V. Lucas. 2002. A comment on the use of flushing time, residence time, and age as transport time scales. *Limnol. Oceanogr.* **47:** 1545-1553.

Nepf, H.M. 1999. Drag, turbulence, and diffusion in flow through emergent vegetation. *Water Resour. Res.* **35:** 479-489.

Nezu, I., and H. Nakagawa. 1993. *Turbulence in Open Channel Flow.* IAHR/AIRH Monograph Series. Balkema, Rotterdam.

Pope, S.B. 2000. *Turbulent Flows.* Cambridge.

Rueda, F.J., and E.A. Cowen. 2005a. Exchange between a freshwater embayment and a large lake through a long, shallow channel. *Limnol. Oceanogr.* **50:** 169-183.

Rueda, F.J., and E.A. Cowen. 2005b. Residence time of a freshwater embayment connected to a large lake. *Limnol. Oceanogr.* **50:** 1638-1653.

Soulsby, R.L., and K.R. Dyer. 1981. The form of the near-bed velocity profile in a tidally accelerating flow. *J. Geophys. Res.* **86:** 8067-8074.

Smart, C.C., and K.C. Karunaratne. 2002. Characterisation of fluorescence background in dye tracing. *Environmental Geology.* **42:** 492-498.

Stacey, M.T., S.G. Monismith, and J.R. Burau. 1999. Measurements of Reynolds stress profiles in unstratified tidal flow. *J. Geophys. Res.* **104:** 10,933-10,949.

Suijlen, J.M. and J.J. Buyse. 1994. Potentials of photolytic rhodamine WT as a large-scale water tracer assessed in a long-term experiment in the Loosdrecht lakes. *Limnol. Oceanogr.* **39:** 1411-1423.

Tai, D.Y., and R.E. Rathbun. 1988. Photolysis of rhodamine-WT dye. *Chemosphere.* **17:** 559-573.

Thackston, E.L., F.D. Shields Jr., and P. R. Schroeder. 1987. Residence time distributions of shallow basins. *J. Environ. Eng.* **113:** 1319-1332.

Upstill-Goddard, R.C., J.M. Suijlen, G. Malin, and P.D. Nightingale. 2001. The use of photolytic rhodamines WT and sulpho G as conservative tracers of dispersion in surface waters. *Limnol. Oceanogr.* **46:** 927-934.

Valentine, E.M., and I.R. Wood. 1977. Longitudinal dispersion with dead zones. *J. Hydraul. Div. Am. Soc. Civ. Eng.* **103:** 975-990.

Wüest, A. and A. Lorke. Small-scale hydrodynamics in lakes. 2003. *Annu. Rev. Fluid Mech.* **35:** 373-412.